Technische Universität München

Physik Department E20

Molecular Nanoscience & Chemical Physics of Interfaces

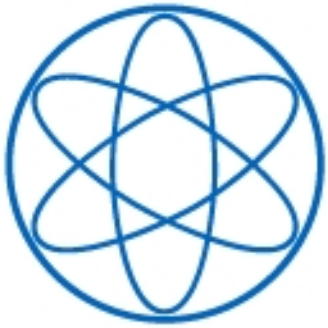

Attosecond time-resolved photoemission from solid samples

DISSERTATION

Andreas Kim

TECHNISCHE UNIVERSITÄT MÜNCHEN

Department E20

Molekulare Nanowissenschaften & Chemische Physik von Grenzflächen

Attosecond time-resolved photoemission from solid samples

Andreas Kim

Vollständiger Abdruck der von der Fakultät für Physik der Technischen Universität München zur Erlangung des akademischen Grades eines

Doktors der Naturwissenschaften (Dr. rer. nat.)

genehmigten Dissertation.

Vorsitzender:	Univ.-Prof. Dr. M. Zacharias
Prüfer der Dissertation:	1. apl. Prof. Dr. P. Feulner
	2. Univ.-Prof. Dr. R. Kienberger

Die Dissertation wurde am 29.06.2015 bei der Technischen Universität München eingereicht und durch die Fakultät für Physik am 22.09.2015 angenommen.

Abstract

In this work, the photoemission from the (110) and (100) surfaces of tungsten is studied with the attosecond ($1\ as = 10^{-18}\ s$) streaking method, an optical pump and probe approach that allows investigations of ultrafast electron dynamics. An extreme ultraviolett pump pulse (XUV) with sub-femtosecond duration excites wavepackets of photoelectrons that are momentum modulated (i.e. probed) by the strong electric field of a near infrared laser pulse (NIR). Variation of the pump-probe delay changes the NIR-field felt by the electron wavepacket, thereby mapping the evolution of the NIR-field strength onto a spectrogram of photoelectron energy versus pump-probe delay time. The method allows the detection of time differences (i.e. delays) between photoelectron wave packets from different orbitals with attosecond resolution. Atomic as well as solid state effects contribute to these relative time delays. Apart from these delay values, the evaluation methods retrieve additional properties of the wavepackets like duration and chirp, i.e. the temporal variation of the photon energy across the pulse.
Analyzing a large set of data with state of the art methods, it is found that wave packet chirp and relative delay values obtained for photoemission from tungsten valence and 4f core electrons are correlated, irrespective of the evaluation method. It is shown that this correlation is partly due to the energy dependence of the photoemission cross sections from the two electronic states, but, by comparing data from W(110) and W(100), also due to electron transport within the solid material. It is shown that such adetailed analysis is only possible if detection and evaluation artifacts are carefully identified and accounted for.
Attosecond streaking experiments make great demands on the electron spectrometers that are used. The total useful electron signals are small and the transmission of the spectrometers has to be large. The very short electron pulses require, on the other hand, absence of detector saturation. To meet these requirements, an electron time of flight spectrometer with a novel lens system has been designed and built. The spectrometer has a detection angle that is adjustable between $\pm 2°$ and $\pm 50°$ and a lens system with constant transmission for a large kinetic energy range. The use of a segmented anode suppresses detector saturation and allows to some extent angle resolved measurements necessary for the substantiation of band structure effects in electron propagation.

Zusammenfassung

In dieser Arbeit wird die Photoemission der (110) und (100) Oberflächen von Wolfram mittels der "Attosekunden-Streaking" Methode ($1\ as = 10^{-18}\ s$) untersucht, einem Ansatz mit optischen Anregungs- und Abfragepulsen, welche die Untersuchung von ultraschnellen, elektrodynamischen Prozessen ermöglichen. Ein Anregungspuls im extremen Ultravioletten (XUV) mit einer Dauer unterhalb einer Femtosekunde regt Photoelektronen-Wellenpakete an, welche durch das starke elektrische Feld eines Laserpulses im nahen Infraroten (NIR) impulsmoduliert (oder abgefragt) werden. Variation der Anrege zu Abfragepuls-Verzögerung verändert das NIR-Feld an der Stelle des Elektronenwellenpaketes und projiziert damit die Veränderung der NIR-Feldstärke auf ein Spektrogram, welches die Intensität gegen die Photoelektronenenergie und die Anrege-Abfrage-Verzögerung aufträgt. Diese Methode erlaubt die Detektion von Zeitunterschieden (oder Verzögerungen) zwischen Photoelektronenwellenpaketen von unterschiedlichen Orbitalen mit einer Auflösung im Attosekundenbereich. Abgesehen von den Zeitunterschieden liefert die Auswertung der Spektrogramme auch zusätzliche Parameter, wie die zeitliche Dauer des Wellenpakets oder dessen Chirp, also die zeitliche Variation der Photonenergie über den Puls.
Durch die Analyse von grossen Datensätzen mit modernsten Methoden lässt sich eine Korrelation zwischen dem Wellenpaket-Chirp und der relativen Verzögerung für die Photoemission aus Valenz und 4f Kernzuständen von Wolfram herstellen, unabhängig von der Evaluationsmethode. Es wird gezeigt, dass sich diese Korrelation teilweise durch eine Energieabhängigkeit der Photoemissions-Wirkungsquerschnitte zwischen zwei elektronischen Zuständen ergibt. Der Vergleich von Datensätzen, gemessen an W(110) und W(100), ergibt jedoch auch einen Anteil durch Elektronentransport innerhalb des Festkörpers. Es wird gezeigt, dass eine solche detaillierte Analyse nur möglich wird, wenn Detektions- und Evaluationsartefakte sorgfältig ausgewertet und beachtet werden.
Attosekunden-Streaking-Experimente stellen grosse Anforderungen an die Leistung von Elektronenspektrometern. Die nutzbaren Signale des Elektronenspektrums sind klein und die Transmission des Spektrometers muss gross sein. Die äusserst kurzen Elektronenpulse verlangen auf der anderen Seite, dass keine Sättigung des Detektors auftreten kann. Um diese Anforderungen zu erfüllen wurde ein neues Flugzeitspektrometer für Elektronen mit einem neuen Linsendesign konzipiert und aufgebaut. Das Spektrometer hat einen frei veränderbaren Akzeptanzwinkel zwischen $\pm 2°$ und $\pm 50°$, sowie ein Linsensystem mit konstanter Transmission über einen grossen Bereich der kinetischen Energie. Die Nutzung von segmentierten Anoden unterdrückt

die Sättigung des Detektors und erlaubt zu einem gewissen Maße winkelaufgelöste Messungen, welche nötig sind für die Untermauerung der Präsenz von Bandstruktureffekten im Elektronentransport.

Contents

Chapter 1.

Introduction

On the microscopic scale, fast electronic rearrangement, transport or transfer of charge as part of photo-excitation, bond formation/breaking or information transfer are at the heart of many processes in biology, chemistry and physics. The timescales of electronic motion can range from femtoseconds (fs, 10^{-15} s) at semiconductor nanostructures down to the attosecond regime (as, 10^{-18} s), which, e.g., is characteristic of inner-atomic motion. A deeper understanding of these processes may help to raise the efficiency of current solar cells and improve information processing devices, organic light emitting diodes and medical radiation-based instruments, e.g. by reduction of radiation damage through ultrafast charge transfer [1, 2]. Electronic currents as carrier of information are not only common in biological systems on a molecular scale, but also as a cornerstone of today's nanoscale computational devices.

Observation and control of electronic motion has therefore been of constant interest of research, where fs-pump-probe techniques [3, 4, 5] have developed into a standard tool, enabling the tracking of processes with femtosecond resolution. Vibrational motion of atoms in molecules occurs on timescales down to tens of femtoseconds [6] and has been observed for the formation and breaking of chemical bonds [7] or the tracking of phonon oscillations in hand with bond softening in Bismuth [8]. The active stabilization of a light pulse's carrier wave maximum (phase) in relation to its envelope, which has advanced recently, also allows the control of electron localization after molecular dissociation [9] with an ultrashort fs laser pulse. Two-photon photoemission (2PPE) with fs-pulses enables the examination of the lifetimes of image potential states [10] and of electron thermalization or cooling [11]. In the same way, electronic motion in semiconductor nanostructures, where the potential well is confined to the nanometer scale, can already be decoded.

Inner-atomic electronic motion, however, unfolds on a much faster timescale, which already becomes apparent considering the Bohr model for the hydrogen atom. The

ground state electron in this case exhibits a classical round trip time of $\approx 150\ as$. Quantum mechanically, the time of electronic rearrangement depends on the energy spacing of the atomic or molecular levels. In the case of inner-atomic processes, it is typically in the range of several eV or more and therefore implies dynamics on the attosecond scale. With the advent of attosecond spectroscopy, fast-scale electronic motion could be finally observed in real time on atomic [12, 13, 14], molecular [15, 16] and solid samples [17, 18]. The first experiments were conducted in terms of the reconstruction of attosecond beatings by interference of two-photon transitions (RABITT) [19], which rely on a measurement of a train of incident attosecond, extreme ultraviolet (XUV) pump-pulses and a delayed near-infrared (NIR)-probe pulse. The technique has not only been used to determine the phases of the harmonics in an attosecond pulse train, but to derive the delays of photoelectrons excited from states within atoms [13] and molecules [20]. Naturally, the utilization of pulse trains limits the effective observation time to the time interval between the pulses. Active stabilization mechanisms of the inner pulse evolution [21, 22] recently allowed for the generation of isolated attosecond pulses, which have been widely used to measure electron transport times or track electron wavepacket motion in atoms and molecules [23, 15]. Also electronic tunneling from shake up states has been a matter of research [24].

The transfer of attosecond techniques onto condensed matter had been accomplished for the first time by Cavalieri et. al. [17]. The applied concept has been used in gas phase before and is dubbed attosecond streaking spectroscopy. Here, for a fixed XUV-to-NIR pulse delay, an isolated attosecond XUV-pulse induces photoemission from the solid and the emitted electron wave packet (EWP) is accelerated or decelerated ("streaked") by a NIR-probe pulse outside the solid according to their arrival time in the NIR field. The XUV-pump to NIR-probe delay is then varied on the attosecond scale in order to obtain a full spectrogram. Alongside the retrieval of the temporal EWP delay, this technique also allows for the retrieval of the EWP chirp as additional information [25]. In their measurements, Cavalieri et. al. could deduce a relative delay of $110 \pm 70\ as$ between EWPs emitted from the conduction band (CB) and the W 4f core states for an excitation energy of 91 eV. Following this result, many theoretical approaches have been pursued [26, 27, 28, 29], which mostly identify either band structure or electron localization effects as the reason for the delay. In this context, the measurements on solids have been continued [30, 18] to gain a more detailed insight into the temporal delay's origin. Interestingly, recent measurements either supported the Cavalieri data or showed a smaller delay value of $55 \pm 10\ as$ [31]. For these experiments, oxygen contamination of the surface could be excluded to play a role in this discrepancy, where adsorbate layers were discussed to influence the NIR onset and the electronic configuration at the surface. Rather, our analysis, under careful consideration of systematic errors of the experiment and data evaluation artifacts, shows that atomic cross-section variations have the potential

to largely influence the measured relative EWP delays. A careful analysis of these effects was one of the goals of the present study.

In this work, the examination of the solid tungsten has been extended, building on large data sets of attosecond streaking spectrograms obtained from the (110) and (100) surfaces of tungsten. The observation of different crystal orientations was motivated by the notion that band structure dependent final state effects could influence the electrons' travel times differently for the (110)/(100) orientations. Moreover, the chirp was reconstructed in our measurements for each CB and W 4f electron wave packet. It was found that the EWP chirp itself, as an outcome of the initial XUV pulse chirp or a response of the solid, can have an influence on the final relative delay, which shows up as a linear trend of the apparent delay versus the individual chirp values. In addition to oxygen induced shifts, this dependency can explain the large deviations of the measurements on W(110) for similar excitation energies (around 90 eV) and enables one to reproduce the retrieved delay values of Cavalieri et. al. by accounting for the average chirp values of their measurement, specified in [32]. These findings may help theorists in the development of a full theoretical description of the electron transport processes within the solid tungsten, which has been hindered so far by the rather complex electronic structure of this material.
Apart from this, a sophisticated new design of the electron spectrometer has been developed and implemented in form of a large-angle, segmented anode time of flight (TOF) spectrometer, where the electron's kinetic energy is derived from its travel time within the detector. The new spectrometer was devised to overcome two given limitations: (1) The low flux of the excitation XUV pulses in attosecond spectroscopy and (2) the energy dependent transmission normally present in current detection systems, which requires post-correction of the measured spectrograms. Therefore, the newly built spectrometer has a large acceptance angle and the electric lens within the spectrometer is built in such a way that negligible energy dispersion occurs in the relevant kinetic energy range between 40 eV and 150 eV. Moreover, the segmentation of the anode reduces saturation effects and allows measurements of the angular distribution of the emitted electrons, where the angular resolution can be freely varied between $2,5^\circ$ and 10°. Future angularly resolved measurements will help to define the influence of band structure effects and will allow for a better comparison with theoretical band structure calculations, which so far are limited to single k-vectors [26].

The achievements of this work should provide further insight into the complex electron dynamics regarding electronic screening, NIR-skin depth and final state effects. The thesis is divided into the following parts: In chapter 2, an overview of attosecond related techniques and an introduction into attosecond streaking spectroscopy is given. Chapter 3 summarizes the experimental setup and the laser system. In chapter 4, the current and the newly built TOF spectrometer are discussed. Finally,

in chapter 5, the data on W(110) and W(100) are presented and discussed, including a discussion of the capabilities of the spectrogram retrieval routine and the extracted chirp dependence in the data. The work concludes with a summary and outlook.

Chapter 2.

Theoretical background

Photoelectron spectroscopy in the attosecond regime ($1\ as = 10^{-18}\ s$) draws its attention from the fact that fundamental processes related to electronic motion can now be resolved in real time, resolving the natural timescale in which electrons move in matter. Several methods and effects intertwine in the realization of attosecond spectroscopy, namely the pump-probe-technique, the photoemission process, the generation of high harmonics and the streak camera detection scheme. In order to better understand the generation and application of attosecond pulses, these techniques will be discussed in more detail.

2.1. Photoemission

Since the first photoemission experiments initiated by Hertz [33], which resulted in Einstein's postulation of the quantization of light ($E = \hbar\omega$) [34], the principle of photoemission has been mostly unchanged. Generally, monochromatic, continuous wave light or alternatively pulsed light (i.e. from a laser or a synchrotron source) is incident on a sample, which can be in a condensed or gas phase, and triggers the excitation of electrons as part of the photoemission process. In Photo Electron Spectroscopy (PES), one can discriminate between preferential observation of valence states and shallow core levels by excitation with light in the ultraviolet (UPS, $h\nu = 5 - 100\ eV$) or of deeper lying core levels by excitation with X-ray photons (XPS, $h\nu < 5\ keV$ or HAXPES, $h\nu > 5\ keV$), which requires vacuum to prevent absorption of light by air (mostly oxygen or nitrogen). On solid samples, ultra high vacuum (UHV) conditions are further needed to guarantee a contamination free surface for the time of observation. The photoelectrons, emitted after excitation by the impinging light, are finally detected by an energy analyzer, which usually is a hemispherical analyzer or a time of flight (TOF) spectrometer. The latter requires a pulsed optical source that gives a time zero of excitation, so that

the propagation time of the photoelectrons to the detector anode can be determined and subsequently converted into a kinetic energy [1]. Depending on the capabilities of the detector, the measurements are conducted either in an angle integrated mode, where the photoelectron intensity is measured after integration over a certain angle range, or in an angle resolved mode. While the energy resolution allows a detailed analysis of the elemental composition of the material and provides information about the chemical environment of an atom by characteristic "chemical" shifts of its core level binding energies (XPS), the angular resolved photoemission (ARPES) allows the reconstruction of the materials band structure. Photoemission is a statistical process, where the transition probability that a photon excites an electron from a certain initial state is governed by Fermi's Golden Rule [35],

$$w \propto \frac{2\pi}{\hbar} \, |\langle \Psi_f | \Delta | \Psi_i \rangle|^2 \, \delta(E_f - E_i - \hbar\omega) \; . \tag{2.1}$$

The Golden Rule describes the transition from an initial state Ψ_i to a final state Ψ_f, each of which describe the total (electronic) system, under the influence of a small perturbation Δ, the photon-matter interaction. The delta function denotes energy conservation upon absorption of a photon with energy $\hbar\omega$. One can see that the photoemission process does not only depend on the material, but also on the excitation energy (and thereupon, the preferentially excited state), which is also reflected by the photon energy dependent experimental photoionization-cross sections. In general, equation 2.1 gives an appropriate description of the detected photoemission spectrum in the case Ψ_i and Ψ_f are known. However, for most cases this is not a trivial problem, such that one often resorts to approximate models.

In a very simple model, photoemission from a solid can be divided into three distinct steps: excitation of the electron, transport through the medium and transmission from the surface barrier into vacuum (Fig. 2.1). The photoelectron excitation is governed by vertical transitions in the reduced zone scheme, which gives for the kinetic energy with respect to the vacuum level:

$$E_{kin} = \hbar\omega - \Phi - E_B \; , \tag{2.2}$$

where ω is the frequency of the exciting light, Φ is the work function of the material and E_B is the binding energy. Since the Fermi energy E_F is easily accessible for metals through the measurement of the Fermi step, binding energies are usually given with respect to E_F. Therefore, for the kinetic energy E_{kin}, measured in reference to the vacuum level E_{vac}, the work function Φ has to be included in equation 2.2 as illustrated in Fig. 2.1. The binding energy E_B of the detected electrons can, thus, be derived from the photoelectron spectra. For the case that synchrotron radiation

[1] A detailed description of the TOF-spectrometer will be given in chapter 4

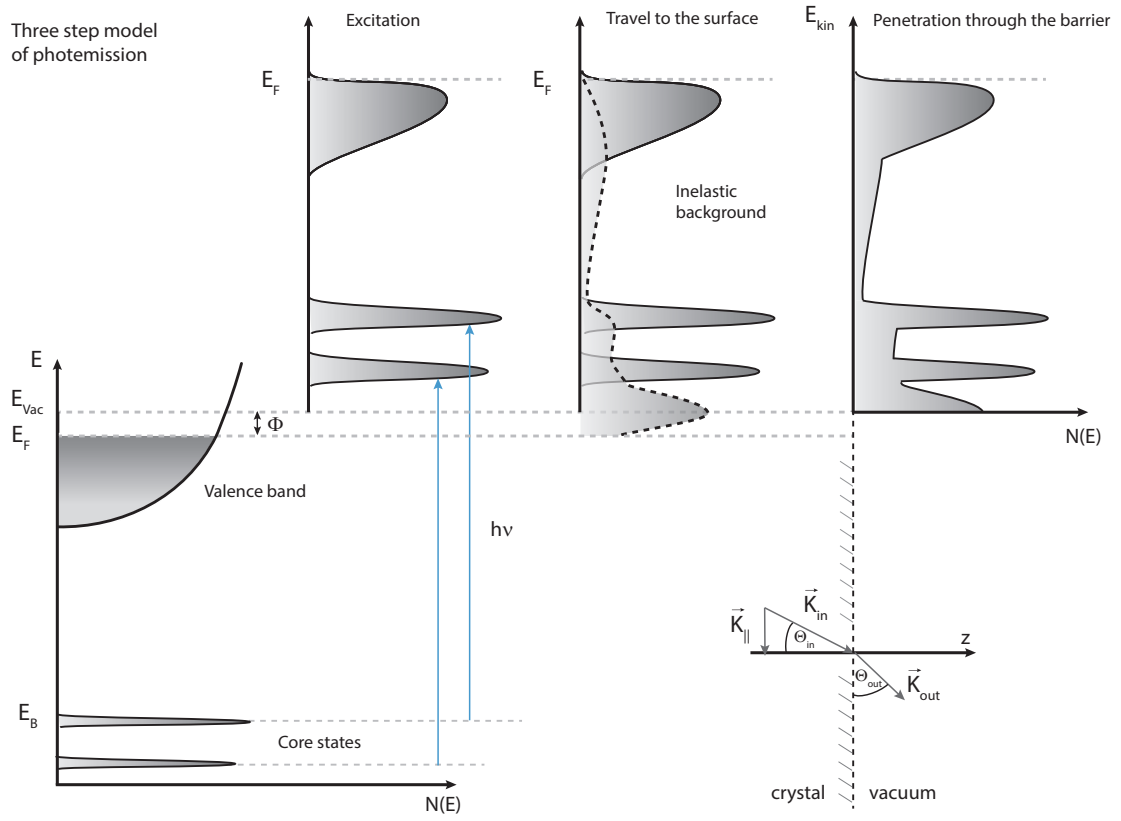

Figure 2.1.: Illustration of the photoemission process in the framework of the three step model. The emergence of the measured photoemission spectrum (top) from the distribution of states (bottom left) inside the solid is depicted schematically. According to the three step model, electron excitation inside the sample, electron transport to the surface and finally transmission of the electrons through the surface barrier into vacuum are considered as separate steps. The sampling depth is limited by the inelastic mean free path (IMFP). Photoelectrons encountering inelastic losses contribute to the inelastic background. The corresponding refraction of the wave vector in the last step is shown in the bottom right corner.

is used, one generally excites with light that has been monochromatized with widths down to the meV range. The spectral width seen in PES for, e.g., a core level then depends on the spectral width of the primary radiation, the core hole lifetime and the experimental resolution of the detectors. Besides energy conservation, momentum conservation has to be obeyed, implying

$$\Delta\mathbf{k} = \mathbf{k}_i - \ \mathbf{k}_f = \mathbf{G} \ . \tag{2.3}$$

The initial and final state wave vectors are given by $\mathbf{k}_i$ and $\mathbf{k}_f$, respectively, and $\mathbf{G}$ describes the crystal lattice vector. It is clear that, for momentum conservation to be fulfilled, a medium has to be present that is able to provide the lattice vector $\mathbf{G}$, otherwise no direct transition is possible [36]. The photon wave vector has been neglected in this case as it gives a vanishing contribution for energies in the UPS range, which are the ones commonly applied in attosecond photoemission.
In the next step, the transport of the excited electron through the sample with its group velocity v_g is considered. The group velocity is given by

$$v_g = \frac{d\omega}{dk} = \frac{1}{\hbar}\frac{dE}{dk} \tag{2.4}$$

and can, thus, be directly related to the final state energy dispersion $E(k)$. Since the wavelength of the electron is in the range of atomic distances, its momentum and energy can be greatly disturbed by elastic and inelastic collisions with phonons or other electrons. Most importantly, inelastic electron-electron collisions, which generally dominate over electron-phonon contributions for the usual excitation energies applied in photoemission, strongly diminish free electron propagation for large escape depths and confine the relevant electron emission to what is known as the inelastic mean free path λ_{e-e}. While this greatly enhances surface sensitivity with escape depths of typically less than 10 Å, it also requires UHV conditions to enable the creation and preservation of clean surfaces for the duration of the measurements. The characteristics of the mean free path plotted against the electrons kinetic energy E_{kin} is given in Fig. 2.2. It is obvious that the mean free path is rather large compared to what could be expected from the magnitude of the atomic distances within a solid. In a simplified picture in terms of a Fermi liquid, the enhancing factors can be traced back to the screening of the electron-electron Coulomb interaction in the electron cloud and more importantly, the Pauli exclusion principle [37]. The latter dictates both post-collision states of the electron-electron-collision to be outside the Fermi sphere. In order to obey energy conservation, only certain transitions are allowed, which minimizes the effective scattering cross section. In general, the inelastic scattering cross-section per atom can be written as [38]

$$\frac{d^2\sigma_{e-e}}{d\omega\ dk} \propto \frac{1}{nv_g^2 k}\ \mathrm{Im}\left(-\frac{1}{\epsilon(\omega,k)}\right) \tag{2.5}$$

with the atom density n and the dielectric function $\epsilon(\omega, k)$. After integration over ω and k, σ_{e-e} is directly related to the inelastic mean free path λ_{e-e} as its reciprocal. The interaction is primarily governed by the energy loss function $g(\omega,k) = \mathrm{Im}\left(-\frac{1}{\epsilon(\omega,k)}\right)$, which itself depends on the dielectric function $\epsilon(\omega, k)$. In the simplest case, the inelastic scattering function is calculated in the model of a free electron gas. It is reasonably accurate except for very small kinetic energies (Fig. 2.2), where the approximation becomes less valid as binding properties cannot be

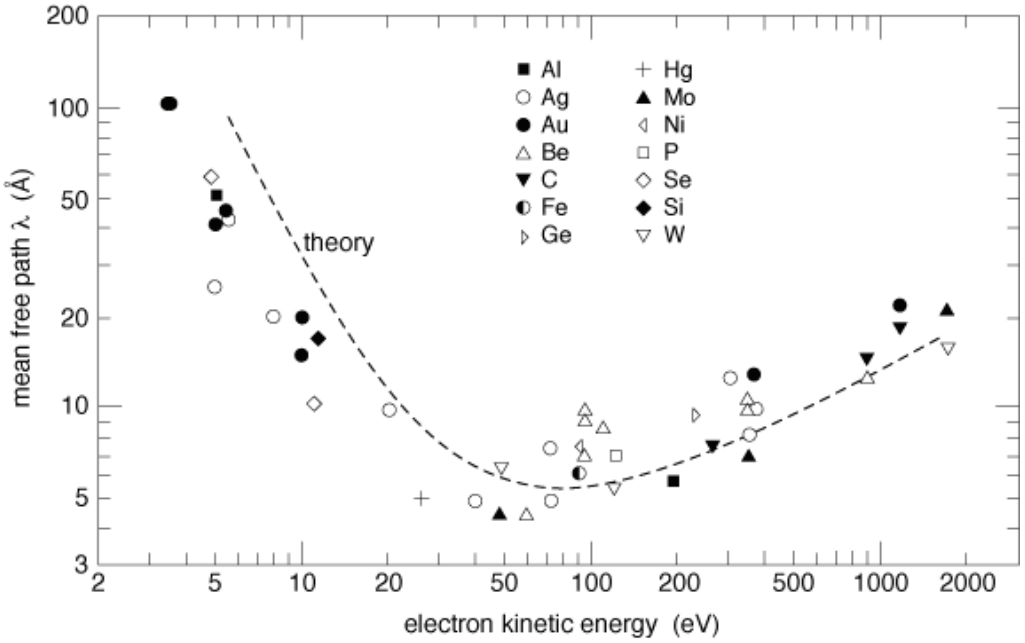

Figure 2.2.: Measured electron mean free paths λ plotted against the electron energy for different materials. The theoretical calculation is given by the dashed line and is fitting very well to the experimental data, except for very small energies. From [39]

neglected anymore [35]. The usual excitation energies in attosecond photoemission spectroscopy lie in the range of $90 - 130\ eV$, which translates to a mean free path of less than 8 Å or less than 3 layers for a tungsten substrate. The experimental analysis of the mean free path is usually derived in terms of the overlayer method, where the intensity decay of the substrate signal can be described as:

$$I \propto e^{-z/\lambda\ \cos\theta}\ . \tag{2.6}$$

Therefore, the attenuation of the photoelectron intensity in dependence of the overlayer thickness z is monitored. This method, however, is rather inaccurate since it is difficult to guarantee a surface with homogeneous overlayers and also elastic scattering, which is not considered in this model, provokes deviations from equation 2.6. It is therefore useful only as a rough estimate.
Finally, the propagating electron has to traverse the surface barrier into vacuum. At this point the electrons kinetic energy has to be larger than the work function Φ or reflection back into the bulk takes place. In this respect, it is also important to maintain a clean surface, since it is known that surface adsorbates (especially the strongly electronegative oxygen) can have a strong impact on the work function [40]. Furthermore, refraction at the surface changes the wave vector $\mathbf{k}$ and the emission angle measured with respect to the surface normal, accordingly. Since the

periodicity parallel to the surface is intact, symmetry prescribes

$$\mathbf{k}_{||}^{out} = \mathbf{k}_{||}^{in} + \mathbf{G}_{||} \ . \tag{2.7}$$

$\mathbf{k}_{||}^{in}$ and $\mathbf{k}_{||}^{out}$ denote the wave vectors inside and outside the solid, respectively. Refraction occurs at the surface governed by Snell's law

$$\mathbf{k}_{||}^{out} = \frac{1}{\hbar}\ \sqrt{2mE_{kin}}\ \sin\theta_{out} = \frac{1}{\hbar}\ \sqrt{2m(E_f - E_0)}\ \sin\theta_{in} \tag{2.8}$$

with the final energy E_f, the energy of the bottom of the valence band E_0 as well as the angles θ_{out} and θ_{in} outside and inside the solid, measured relative to the surface normal. It is obvious from this equation that by measuring the kinetic energy and the exit angle, $\mathbf{k}_{||}$ can be determined. In principle, this allows the energy dispersion E(k) or in other words the solids band structure to be received. The wave vector $\mathbf{k}_{\perp}$ is not conserved though, since the symmetry perpendicular to the surface is broken. Therefore, 3D band structures cannot be directly derived from ARPES measurements without making assumptions about the perpendicular component of the electron wavevector. Either theoretical support is needed, e.g. by comparison of experimental data with PES simulations based on calculated trial band structures, or experimental workarounds have to be applied, i.e. by measuring the angle resolved appearance and disappearance of maxima near the Brillouin zone boundaries for different crystal orientations or mapping a band transition for a fixed emission angle under variation of the photon energy. Equation 2.8 can also be used to estimate the sampled k-values within an angle integrated measurement. Assuming exemplarily an acceptance angle of the energy analyzer of $\Delta\theta = 20°$ and a kinetic energy of 90 eV, derivation respective to $\Delta\theta$ yields $\Delta k_{||} \approx 1.7$ Å^{-1}, which is comparable to the size of the Brillouin zone of tungsten (≈ 1.5 Å^{-1} for W(110)). Obviously, acquiring the signal integrated over the full angle range means averaging over the whole Brillouin zone. This has to be taken into account when comparing the measured data with theoretical simulations of attosecond photoemission from solids based on band structure calculations. Currently these simulations are solely calculated for one direction of $\mathbf{k}$ owing to the large demands of the calculations (i.e. necessary CPU time).

While the three step model of photoemission is a very useful tool to gain insight into the different processes, it simplifies considerably by neglecting any interference between the steps. A one step model tends to be a more precise description. It describes the whole photoemission process as a single step, as is the case in Fermi's golden rule 2.1, provided that the correct initial and final states are known. In order to derive these states one often resorts to what are called the "inverse LEED" states. This concept can be explained through the principles behind low energy electron diffraction (LEED) experiments. Here, a monochromatic beam of electrons is incident on a sample and is either transmitted or reflected from the surface, the

latter either directly at the surface or within the inelastic mean free path. If the reflected part is assumed to be zero and the propagation direction of the beam is reversed, one obtains a picture similar to the photoemission process. The wave inside the solid can be described by a damped Bloch wave, which is matching a freely propagating electron wave outside the solid. Therefore, inserting such states into equation 2.1 enables treatment of the whole process in a single step. In most cases, the three step model is yet the preferred one, since it is phenomenologically easier to grasp and often yields reliable results.

The energies retrieved in photoemission experiments usually deviate from the initial state energies calculated, e.g., by Hartree-Fock. This is due to a relaxation of the whole electronic system after excitation, which acts back on the emitted electron. This process is called electronic screening and influences the electronic transport times. Specifically, calculations have shown that screening of the core hole after excitation proceeds in the attosecond timescale [41, 42], thereby affecting the interaction of the emitted electron with the associated hole. One can separate between screening by electrons within the atom, denoted as intra-atomic relaxation, and screening by polarization of the matter surrounding the core-excited atom (extra-atomic relaxation) [35]. Both contributions are attributed to final state effects, where changes in the final state lead to a different measured binding energy. Other final state contributions can be, for example, plasmon losses, electron-hole excitations or exchange splitting, leading to a different set of final states. In contrast, chemical (peak) shifts are usually attributed to initial state effects, depending strongly on the chemical environment of an atom in its ground state. The commonly applied methods of photoelectron spectroscopy offer high spectral resolution, but with exceptions (e.g. core hole clock spectroscopy [43, 44]) they are not able to provide temporal information about the electron dynamics following photo-excitation. Therefore, in attosecond streaking spectroscopy, the high spectral resolution of conventional PES is traded for an unmatched temporal resolution on the attosecond timescale.

2.2. Pump-probe spectroscopy on the femtosecond time scale

A first step towards attosecond spectroscopy is the pump-probe technique, which in the standard application with Ti:Sapphire lasers already provides a resolution down to the femtosecond timescale ($1fs = 10^{-15}\ s$), thus allowing to track e.g. molecular vibrations and bond breaking [45]. In pump-probe spectroscopy, two pulses are used denoted as pump and probe, where the pump pulse promotes the system to an excited state and the probe pulse samples the evolution of the system after a given

delay τ. Variation of τ now reveals the full temporal dependence of the excited state. The temporal resolution is primarily limited by the temporal width of the pulse envelopes, since the excitation itself spans over this time range as does the probe process. Therefore, much effort has been paid to reduce the pulse durations resulting in pulses down to the femtosecond scale. Assuming a Gaussian envelope, the electric field of the pulse can be described as

$$\begin{aligned} E(t) &= A(t) \cdot e^{i(\omega_0 t + \Phi_C(t) + \Phi_{CEP})} \\ &= E_0 \cdot e^{-4 \ln 2 \ (\frac{t}{\Delta\tau})^2} \cdot e^{i(\omega_0 t + \Phi_C(t) + \Phi_{CEP})} \ , \end{aligned} \tag{2.9}$$

where $A(t)$ is the temporal pulse envelope, ω_0 denotes the central frequency of the pulse, $\Delta\tau$ is the pulse's full width half maximum (FWHM) and Φ_{CEP} is the so called carrier envelope phase (CEP). The latter describes a constant phase shift between the carrier wave and the envelope and becomes important for pulses near the single cycle limit (i.e. close to 2.5 fs for 750 nm light). The time dependent phase $\Phi_C(t)$ depicts changes of the carrier wave or pulse form. Characterized by a linear time dependence, $\Phi_C(t)$ simply invokes a spectral shift of the entire pulse, whereas higher order dependencies introduce what is widely known as chirp [46]. In the most general way, it reflects a time dependence of the instantaneous frequency: $\omega(t) = \frac{d\phi(t)}{dt}$ (for a general phase term $\phi(t)$), which means that the number of carrier oscillations within the pulse is changing over time. This behavior also modifies the form of the pulse envelope, leading to a larger FWHM than given in the chirp free or "Fourier-limited" case. A linear chirp is characterized by a dependency $\Phi_C(t) = bt^2$ with a constant chirp parameter b.

In many cases a spectral representation of the pulse can also be useful. It can be derived by a simple Fourier-transform from

$$E(\omega) = \frac{1}{\sqrt{2\pi}} \int dt \ E(t) \cdot e^{-i\omega t} \ . \tag{2.10}$$

As the Fourier-transformation of a Gaussian pulse is, itself, a Gaussian line shape, the spectral domain is also defined by a Gaussian distribution. The two domains, in particular the spectral bandwidth $\Delta\omega$ and temporal FWHM pulse duration Δt, are linked by the time-bandwidth-product

$$\Delta\omega \cdot \Delta\tau \geq 2\pi c_B \tag{2.11}$$

where c_B is a constant, which is dependent on the pulse shape and constitutes ≈ 0.44 for a Gaussian pulse. Equation 2.11 is equivalent to the Heisenberg uncertainty relation and only equals $2\pi c_B$ in the Fourier-limited case. Any chirp introduced to the pulse significantly broadens the pulse. The change in the pulse form for

propagation through a medium of length L can be depicted by inspecting the Taylor-expansion of the wave vector

$$\begin{aligned} k(\omega) &= \frac{\phi(\omega)}{L} \\ &= k(\omega_0) + \frac{\partial k}{\partial \omega}\,(\omega-\omega_0) + \frac{1}{2}\,\frac{\partial^2 k}{\partial \omega^2}\,(\omega-\omega_0)^2 + \frac{1}{6}\,\frac{\partial^3 k}{\partial \omega^3}\,(\omega-\omega_0)^3 + ... \end{aligned} \tag{2.12}$$

The first term denotes a simple spectral phase shift, which keeps the shape of the pulse intact and is governed by

$$\omega_0 = v_P \cdot k(\omega_0) \quad \text{or} \quad v_P = \frac{\omega_0}{k(\omega_0)} \tag{2.13}$$

with the phase velocity v_P. The second term is linked with the group velocity v_G by the term

$$k'(\omega) = \frac{\partial k}{\partial \omega} = \frac{1}{\frac{\partial \omega}{\partial k}} = \frac{1}{v_G} \quad \text{with} \quad v_G = \frac{\partial \omega}{\partial k}\ , \tag{2.14}$$

the velocity of the pulse envelope. In most cases, v_P and v_G are not equal, which means that the carrier wave maximum is drifting away from the maximum of the carrier envelope. The group delay emerging from this behavior is given by

$$t_g = \left(\frac{1}{v_P} - \frac{1}{v_G}\right) \cdot L \tag{2.15}$$

and is directly related to the carrier envelope phase Φ_{CEP}. The first two terms of equation 2.12 only introduce a constant phase shift and leave the form of the pulse intact. In contrast, higher order terms introduce dispersion and thereby a modification of the pulse form. The third term is often referred to as the group velocity dispersion (GVD) since it holds

$$k''(\omega) = \frac{\partial^2 k}{\partial \omega^2} = \frac{\partial}{\partial \omega}\left(\frac{1}{v_G}\right) \tag{2.16}$$

Propagation of a pulse through a medium imposing GVD means that the emergent pulse is inevitably chirped and temporally broadened. A Fourier-transformation of the spectral representation of a pulse including a contribution from 2.16 shows that the pulse is now linearly chirped in the temporal domain, where the pulse duration can be approximated by the revised time-bandwidth-product for a Gaussian pulse

$$\Delta\omega \cdot \Delta\tau = 0.44 \cdot 2\pi \cdot \sqrt{1 + \frac{1}{4}\,b^2\,\tau^4}\ . \tag{2.17}$$

It is apparent that both positive and negative chirps lead to a pulse broadening compared to the minimal possible pulse width for the Fourier-limited case. In principle, following equation 2.17, one could try to significantly increase the spectral

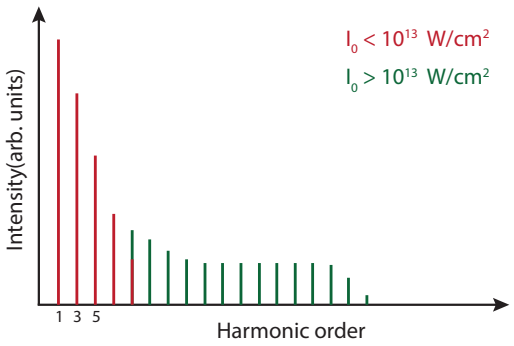

Figure 2.3: Evolution of generated harmonic orders for low driving laser intensities (red lines, perturbative regime) and large intensities (green lines, non-perturbative regime). The formation of a plateau for higher intensities can be seen clearly in the power spectrum.

bandwidth in order to achieve an ultrashort pulse in time. This approach works, however, only until a fundamental limit is reached: The duration of a single optical cycle. Therefore, in the mid-1980's the so called femtosecond-barrier was reached for laser light, which was typically in the IR-range ($700\ nm - 1\ mm$). Breaking this barrier can only be achieved by lowering the central wavelength and thus, lowering the duration of a single cycle. Therefore, one has to move into the extreme ultraviolet (XUV) range ($10\ nm - 121\ nm$) to be able to generate pulses in the attosecond regime.

2.3. High Harmonic Generation (HHG)

The generation of attosecond pulses is one of the key parameters in attosecond streaking spectroscopy. Since no gain medium is available that can provide the necessary bandwidth in the XUV-range, its creation directly within the laser cavity is not possible. The conversion of pulses into the XUV domain thus turned out to be technologically challenging and it succeeded with the advent of the high harmonic generation (HHG) technique. The possibility of creating lower order harmonics from a given laser pulse has been already known since the 1960's, where the second harmonic generation (SHG) was accomplished for the first time [47]. Here, in a very simplified picture, two photons at frequency ω combine to generate one photon at double frequency 2ω. The process of harmonic generation is governed by the nonlinear response of the polarization $P(t)$ in a medium to the external electric field $E(t)$ as [48]

$$P(t) = \epsilon_0 \left(\chi^{(1)} E(t) + \chi^{(2)} E^2(t) + \chi^{(3)} E^3(t) + ... \right) \quad . \tag{2.18}$$

The above form is a Taylor-expansion of the polarization term with the superscript denoting the respective orders. For a medium exhibiting a second order susceptibility

$\chi^{(2)}$, the SHG then is the dominant process, for a third order susceptibility $\chi^{(3)}$, third harmonic generation (THG) occurs and so on. In quantum mechanics low order harmonic generation can usually be described within perturbation theory, where the electric field is treated as a small perturbation [46]. Within this theory, the conversion efficiency rapidly decreases with harmonic order following an exponential decay. While this may be true for laser intensities below $10^{12}\frac{W}{cm^2}$, employing by far higher intensities leads to deviations from this theory. In the non-perturbative regime, the perturbation of the electric field can no longer be considered small and the electric field is now strong enough to influence the atomic potential. This behavior is manifested in the formation of a plateau for higher orders for which the harmonic intensity stays approximately constant, followed by an abrupt cut-off at the highest order. For gases this was first found experimentally by McPherson in 1987 [49] and since then the process, dubbed high harmonic generation (HHG), has usually been achieved by focusing an intense near infrared (NIR, $750 - 1400\ nm$) laser beam into a gas target. Here, inversion symmetry of the gas invokes the generation of only odd harmonics. The use of a gaseous medium has been found advantageous for the high intensities applied here, since the constant gas flow equals "regeneration" from damage. Moreover, primarily noble gases are used because of their high ionization potentials I_P, which enable higher XUV photon energies. The cut-off energy of HHG is intensity dependent and can be described for gases as [36]

$$E_{cut-off} = I_P + 3.17 \cdot U_P \tag{2.19}$$

where U_P is the ponderomotive "wiggle" energy supplied by the NIR-laser field

$$U_P = \frac{e^2 E_0^2}{4m\omega^2} \tag{2.20}$$

In a semi-classical description, Corkum [50] developed a simple phenomenological model, which separates the HHG process into three distinct steps. In the first step atomic ionization under the influence of the strong laser field takes place. Depending on the laser intensity, two distinct paths of ionization are now possible, which can be identified in terms of the Keldysh parameter [51]

$$\gamma = \frac{\omega\sqrt{2mI_P}}{eE} \tag{2.21}$$

with the laser electric field E, the ionization potential I_P, the frequency ω and the electron mass m. For $\gamma >> 1$ the laser electric field is comparably weak and ionization takes place by electronic absorption of multiple photons, which is called above threshold ionization (ATI). For $\gamma << 1$ the external laser electric field is now strong enough to bend the atomic potential, which makes electron tunneling possible. In the latter regime HHG takes place. As the electric field strength is varying over

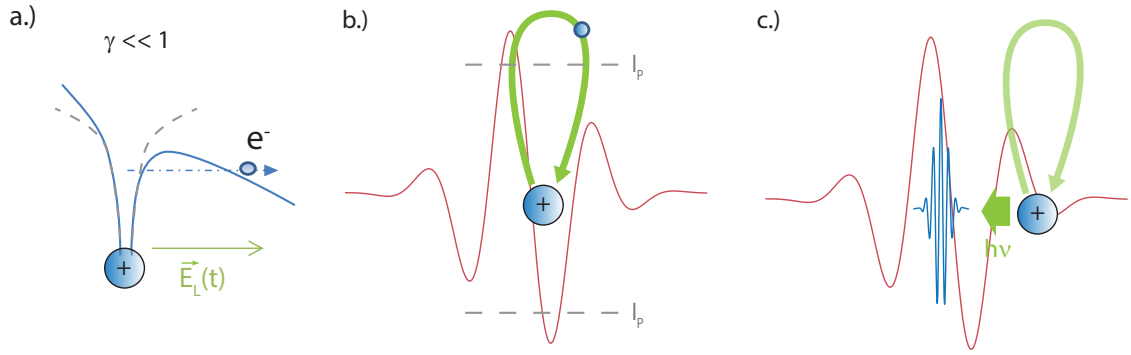

Figure 2.4.: Illustration of the three step model of HHG: a.) The laser electric field is strong enough to bend the atomic potential, so that electron tunneling becomes possible. Ionization only occurs at instants, at which the gain in energy by the electric field is larger than the ionization potential I_P. b.) Electron propagation in the laser field. c.) Emission of a high energetic XUV photon-pulse, which is inherently synchronized with the NIR-field.

time, it is obvious that electron tunneling is only possible in short time-frames (300 *as* or lower) around certain points, where the electric field strength obtains its highest value. As soon as the electron has tunneled through the barrier, in the second step the electron movement is driven by the oscillations of the laser. The electron is accelerated away from the atomic core until the sign of the laser vector potential changes. Then, the electron is accelerated back to its origin. In the third step, the electron can, with a certain probability, recombine with its parent ion by emitting a high energy photon. The kinetic energy of the electron gained through the laser induced acceleration process is thus converted into photonic energy. The short time window, in which ionization is possible, as well as the fast recombination of the ejected electron to within one optical cycle entails the generation of pulses with durations down to 100 *as* or lower, depending on the harmonics gained. Since the process of ionization and recombination is repeated for each sufficiently strong maximum of the electric field, it gives rise to a train of pulses separated temporally by one half of the fundamental optical cycle. Therefore, within each fundamental period two attosecond pulses can be created corresponding to its two electric field maxima. The strong temporal confinement demands that the XUV- and near infrared (NIR)-pulse are inherently coherent with each other. This strong synchronization is very useful for the implementation of pump-probe experiments.

The process of high harmonic generation has also been revised by the use of a full quantum mechanical model by Lewenstein [36] as well as in terms of Feynman's

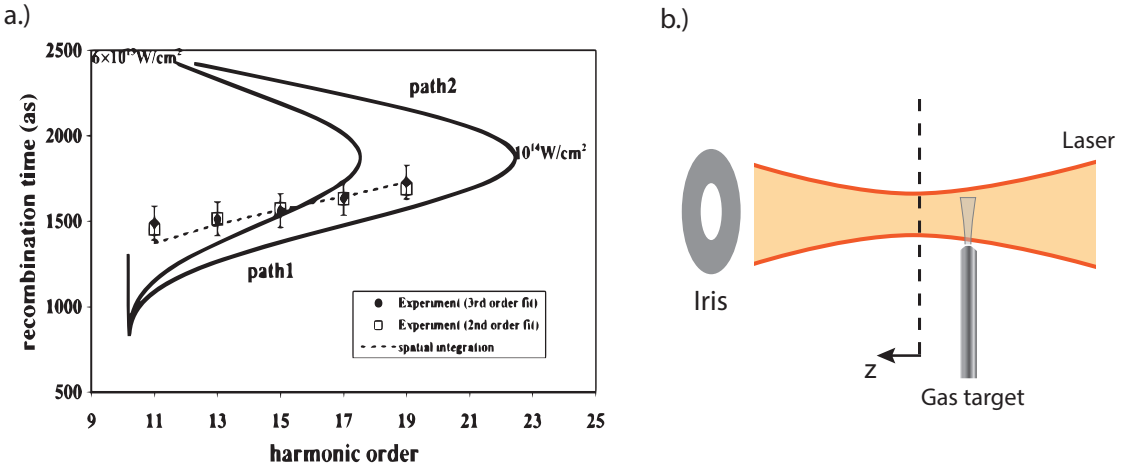

Figure 2.5.: a.) Calculation of the recombination times for the long and short electron trajectories plotted against the harmonic order for two different intensities. The different recombination times over the energy can also be translated into an intrinsic chirp (see text for further explanation). From [52] b.) Illustration of the HHG process for gas: Depending on the position of the laser focus to the gas target, a different phase matching can be achieved. Moreover, an iris allows separation of the less divergent short trajectories.

path integral by Salières [53]. Both support the semi-classical interpretation of the three-step model derived by Corkum. In fact, it was shown that the dominant electronic motion is determined by quantum orbits, space-time trajectories for which two different quantum paths lead to the same final energy. Those paths have been dubbed short and long trajectories, because of their different recombination times. Fig. 2.5 shows the corresponding recombination times plotted against the generated harmonic order. As the recombination times of each harmonic differ, which can be translated into a phase difference between the harmonics, a pulse arising as the combination of several harmonics is inherently chirped [52]. It is clear from Fig. 2.5 that this intrinsic attosecond chirp is different for short and long trajectories giving a positive or negative chirp, respectively. Furthermore, both trajectories also show different spatial characteristics containing a different spatial divergence [54]. The harmonics originating from short trajectories can thus be separated as a result of a lower divergence compared to those originating from long trajectories, for example by a simple iris. Moreover, the ratio of short and long trajectories depends also on the position of the gas target relative to the laser focus [53]. Depending on the position of ionization within the focus a different phase is accumulated [55]. The phase term can be divided into a superposition of the geometric (asymmetric) Gouy phase [56] and the intensity dependent (symmetric) dipole phase. Therefore, the

overall attained phase varies with relative focus position. In common experiments the gas extends over a range of approx. 1 mm along the laser focus, so that by varying the focus position effective phase matching of XUV-photons emitted throughout the interaction volume is achieved. Usually one resorts to a position, where the relative change of the combined dipole and Gouy phase is minimal over the interaction volume. In this case the gas target is placed behind the laser focus and best phase matching is achieved on-axis, preferring the low dispersive short trajectories, whereas moving the target in a position in front of the laser focus leads to phase matching off-axis, preferring the spatially more dispersive long trajectories [55]. Additionally, the gas pressure (as a measure of the interaction volume) and the laser intensity itself influence the phase matching [57].
In an investigation of HHG near the cut-off [58] Chang discussed the *temporal* dependence of the overall phase and the resultant chirp inherent to it. The overall phase in time domain is built up from the dipole phase $\Phi_D(t)$, whose temporal dependence arises from its connection with the time-dependent laser intensity, and the laser induced chirp $\Phi_L(t) = qbt^2$, which transfers the laser chirp b to each harmonic q. Therefore, the laser field projects its chirp on each harmonic modified with a factor q, the harmonic number. The phase shift between the harmonics leads to a chirp in a pulse comprising several harmonics. It was found that this effect is most dominant for negative chirps [58, 59]. Though a chirp in the generated XUV-pulses is mostly an unwanted effect, it has been shown recently that by modifying the temporal phase of the excitation pulse, an optimization of the time dependent phase around one certain harmonic can be achieved [60].
For the generation of high harmonics usually ultrashort excitation pulses below $10fs$ are used. They have been found advantageous, since for extremely short pulses the possibility of the electron to re-encounter the core more than one time is diminished [61]. Several electron encounters tend to weaken the phase coherence between the harmonics. Moreover, for a rapidly varying electric field the atoms can survive longer before ionization resulting in the generation of higher harmonics. Another advantage is the increased energetic separation of the manifold of pulses originating from one exciting NIR-pulse. As mentioned before, at the position of each electric field maximum, where the gain in energy exceeds the ionization potential, a distinct attosecond pulse emerges in HHG. This results in the generation of attosecond pulse trains, in which each pulse is separated by half a period of the fundamental. Normally, one is rather interested in performing experiments with isolated single pulses instead of a pulse train, since the latter confines the observation timescale to exactly the separation between the pulses. Therefore, several gating techniques have been developed, which focus on the separation of a single pulse from a given pulse train.

2.3.1. Pulse gating techniques

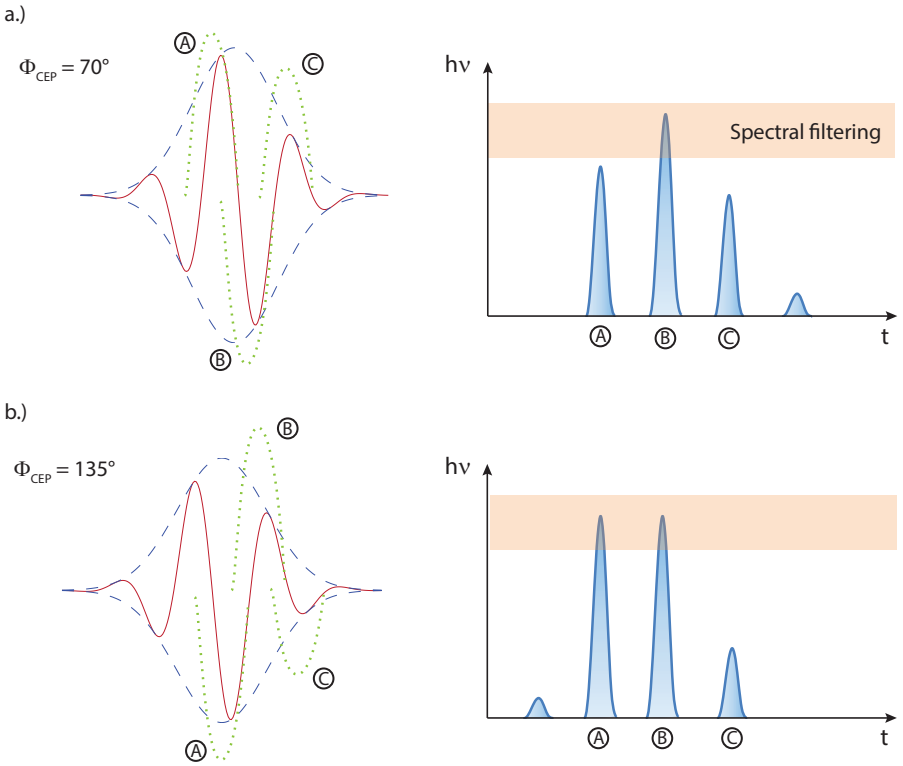

Figure 2.6.: Schematic view of the emergence of an attosecond pulse train from a NIR-few cycle pulse (left) and the subsequent isolation of a single attosecond pulse by means of spectral filtering (right). a.) Left side depicts the NIR-field (red) for the case of largest spectral contrast between the generated XUV-pulses according to [62]. The green dotted lines schematically depict the electron paths. The filter can then be placed, so that only one pulse is passing through. b.) The same NIR-pulse with a different CEP-phase is depicted. Now, the pulses cannot be separated spectrally and a double pulse is generated.

The most commonly applied technique is the use of spectral filters, as illustrated in Fig. 2.6. Already in the framework of the three step model of HHG it becomes clear that, depending on their moment of ionization, the electrons undergo a different acceleration and thereby acquire a different kinetic energy through the interaction with the electric field in step two of HHG. The pulses hence attain different cut-off energies in the corresponding harmonic spectra, whose separation drastically increases with shorter near infrared (NIR) excitation pulses. This also means that, for ultrashort pulses, the harmonics of the cut-off and the near plateau harmonics are inherent to a single attosecond pulse. The application of a spectral filter now

allows the separation of this pulse from the surrounding ones. Since the separation by a spectral filter only works by restraining the outgoing pulse to the higher energetic harmonics, the filtered pulse will always have a larger pulse duration than what is present in the attosecond pulse train, where the full harmonic spectrum is available. Nonetheless, with this technique, pulses down to 80 as could be achieved, representing, for a long time, the shortest achievable isolated attosecond pulses [62]. In most cases spectral filtering is achieved through reflection from a multilayer XUV-mirror [63, 64], which simultaneously allows focusing of the XUV light by introduction of a curvature to the mirrors surface. The mirrors usually consist of alternating stacked layers of Mo and Si, due to their high reflectivity in the XUV-range. As the penetration depth is different for each wavelength component of the XUV pulse, aperiodic stacking of these layers introduces a different group delay to each component. In particular, the amplitude and phase of the mirror reflectance are calculated in a way that the desired pulse-form, a Gaussian output pulse, is achieved. As mentioned before, the spectral cut-out is placed in the plateau/cut-off region, where the spectral intensity stays approximately constant over several harmonics. This facilitates the calculation of the mirror reflectance, which then in many cases retains an approximate Gaussian shape. The final pulse duration of the reflected pulse can be estimated from the supported bandwidth of the mirror reflectance, which is also the transform-limited bandwidth of the reflected pulse. Also, an overall chirp can be introduced by the mirror, since the principle of the XUV mirror lies in the implementation of a wavelength dependent group delay dispersion. This can be used to compensate for the intrinsic chirp from the HHG process.
As illustrated in Fig. 2.6, the carrier envelope phase Φ_{CEP} of the NIR-pulse (see equation 2.9) now plays a major role. The form of the electric field of the ultrashort NIR-pulses applied here now drastically changes with the value of Φ_{CEP}. Depending on its exact value, either one or two pulses of the attosecond pulse train fall in the spectral filter range. As a result, a satellite pulse accompanying the main pulse or an equal intensity double pulse can be created, both of which are unwanted effects. In Ref. [62] it was found that for a 1.5 cycle NIR-pulse the maximal separation between the pulse with the highest energy and its surrounding pulses can be achieved for a carrier envelope phase of $\Phi_{CEP} = 70°$. In this case, more than 90 % of the final spectrum consists of the harmonics of a single attosecond pulse. In the same paper, the minimal (energetic) pulse-to-pulse contrast was found to be at 135°, which would result in two pulses generated from HHG that cannot be separated in the spectral range given their close spectral overlap. Thus, a double pulse is created. The carrier envelope phase drifts within the laser cavity itself, because the group- and phase velocity are not equal for the propagation within the laser medium. Therefore, the implementation of precise CEP-stabilization mechanisms are necessary to guarantee the repetitive stable generation of isolated attosecond pulses. The applied CEP-stabilization mechanisms are described in detail in section 3.1.1.

Instead of a spectral filtering, isolation of a single attosecond pulse can also be achieved by the use of temporal gating. As has been mentioned in several theoretical approaches [65, 50], the HHG process is very susceptible to the polarization of the excitation laser field. Following these lines, a technique called polarization gating can be utilized [66], which relies on a laser field with a polarization changing from elliptical to linear and finally back to elliptical. Such a field can by created using a pulse-shaper, if two perpendicularly polarized pulses with different frequencies are superimposed. Since HHG in the picture of the three-step model relies on the re-encounter of the electron with its parent ion, the generation of XUV photons is prevented for elliptically polarized light, for which the electron is not accelerated back to its origin. In polarization gating, one lets the NIR-light adopt a linear polarization only for a short time, less than one optical cycle. Then, HHG can only occur at a single electric field maximum and thus a single attosecond pulse is created. Though guaranteed satellite-free pulses can be generated with this technique, the electric field strength of this modified field at the spot of ionization is lower than for an unmodified pulse. Therefore, the achievable maximal pulse energy and ionization rate, respective conversion efficiency, are relatively low.

A third possible gating method is the superposition of the fundamental driving laser with light fixed at the second harmonic of the fundamental. In this approach one can optimize the relative intensity of the main (electric field) peak and therefore increase the contrast to the surrounding peaks. These so called two-color fields can also be used to increase the temporal distance between the attosecond pulses. The requirements for a temporal gate are then lowered, so that e.g. a wider polarization gate can be used. The combination of both methods is called “double-optical gating”. The preferred method in our measurements, however, has been the spectral filtering, due to its high cut-off energy and good conversion efficiency between 10^{-5} and 10^{-6} [67, 6].

2.4. Attosecond streaking on solids

With the generation of attosecond pulses, observation of electronic motion on the attosecond scale came into reach. At a first glance, realization in a traditional pump-probe-setup seems reasonable, with both pulses in the attosecond regime. The low photon flux and the low two-photon transition probabilities in the XUV-regime, however, prevent the direct transfer of this technique. With the knowledge that the XUV-pulse is, since its birth, inherently in phase with the NIR-pulse, one can yet devise an operation mode very similar to the work principle of a streaking camera [6, 68, 25, 69]. In the first place, the XUV-pulse is inducing photoemission, where far away from any resonances the generated electron wave packet is a replica of

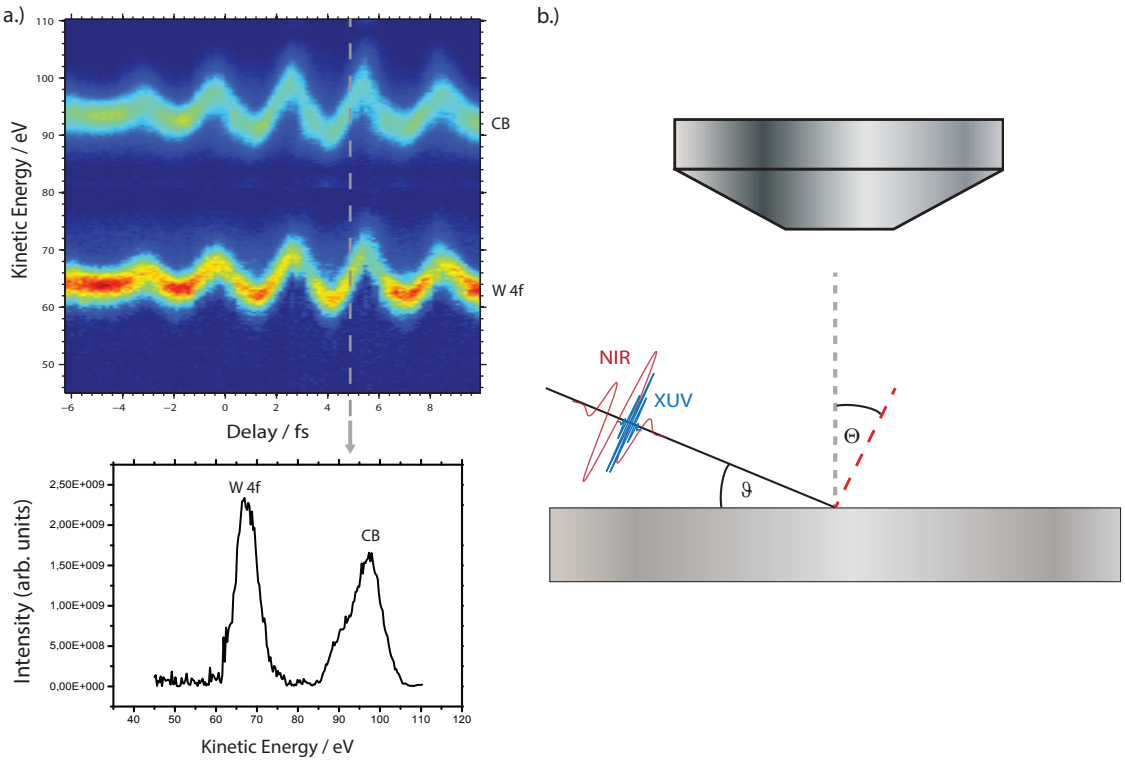

Figure 2.7.: a.) False-color plot of a measured attosecond streaking spectrogram. The spectrogram consists of several intensity-versus-energy plots (bottom) for different delays (top) between the XUV- and NIR-pulse. b.) Simplified illustration of the setup for attosecond streaking spectroscopy. The incident XUV-pulse (blue) photoexcites electrons, which are momentum-modified by the NIR-field (red). Detection of electrons is performed by a TOF-spectrometer.

the XUV pulse, adapting its parameters as well as its chirp. In the next step, the emitted electron wave packet (EWP) interacts with the electric field of the NIR-laser pulse. From the instant t_0, at which the electrons enter the NIR-field, they are accelerated and decelerated by the electric force until the end of the pulse. The acquired net change of momentum Δp after the NIR-pulse has passed, depends on the vector potential $A_{NIR}(\mathbf{r}, t)$ at the instant t_0.

$$\Delta\mathbf{p}(t_0) = \int_{t_0}^{\infty} \mathbf{F}\, dt = -e \cdot \int_{t_0}^{\infty} \mathbf{E}_{NIR}\, dt = -e \cdot \mathbf{A}_{NIR}(\mathbf{r}, t_0) \quad , \tag{2.22}$$

since $\mathbf{E}(t) = \frac{d\mathbf{A}(t)}{dt}$. Δp translates into the kinetic energy change ΔE, which can be measured preferably by a time of flight spectrometer (TOF).
This technique, dubbed attosecond streaking, can be applied in the gas phase, where

the laser interaction with the electron can be seen as almost instantaneous after ionization, or for solids. In the latter case, estimates based on the Fresnel equations show that due to refraction the contribution of the laser field parallel to the surface normal is negligible inside a metal [17]. Usually, the laser polarization as well as the detection axis of the TOF-spectrometer are oriented along the surface normal. For a metal, electronic screening ensures that the electrons propagating to the detector feel the full NIR-laser field after leaving the solid [2]. Thereby, the streaking technique theoretically enables the measurement of the electron travel time to the solid's surface after excitation. A complete attosecond spectrogram is now acquired by variation of the XUV-/NIR- pulse delay $\Delta\tau$. With advancing delay, photoelectrons sample the vector potential of the NIR-pulse at subsequent instants ("streaking"). The resulting streaked curves thus reflect the NIR-pulse form, which can be seen in the complete spectrogram in Fig. 2.7. The false-color plot gives the signal intensity plotted against the electron energy and the delay $\Delta\tau$. The intensity as a function of the kinetic energy for a constant delay yields a single energy distribution spectrum as measured by the TOF spectrometer. In this example, the two peaks correspond to the 4f and conduction band states of tungsten. Arrival times at the NIR-field can differ for electrons from different states as result of e.g. different travel or emission times. This results in a differential shift of the streaked curves with respect to each other, which makes it possible to measure the relative delay between the electrons from these two states. In a more detailed description, the laser-photoelectron interaction can be described within the framework of a semi-classical approach. Here, the electrostatic force of the laser field acting on the emitted electron can be expressed as

$$\mathbf{F}(t) = \frac{d\mathbf{p}}{dt} = -e \cdot \mathbf{E}_L(t) \tag{2.23}$$

with the laser electric field $\mathbf{E}_L(t)$. Considering the initial momentum $\mathbf{p}_0$ of the electron, the total electronic momentum $\mathbf{p}(t)$ during and after laser interaction can then be written as

$$\mathbf{p}(t) = \mathbf{p}_0 - \int_{t_0}^{t} dt\ e \cdot \mathbf{E}\ , \tag{2.24}$$

where t_0 denotes the instant, at which the electron enters the electric field. Since the electric field is directly connected to its vector potential via $\mathbf{E}(t) = \frac{d\mathbf{A}(t)}{dt}$, one can write

$$\mathbf{p}(t) = \mathbf{p}_0 + e \cdot (\mathbf{A}(t) - \mathbf{A}(t_0))\ . \tag{2.25}$$

When the laser field has ceased, its vector field $\mathbf{A}(t)$ at the electron's position is obviously zero. The final kinetic energy of the electron can then be written as

$$E_{kin,f} = \frac{p^2}{2m} = \frac{1}{2m}\ (p_0^2 - 2\ e\ \mathbf{A}(t_0)\ \mathbf{p}_0 + e^2\ A^2(t_0))\ \ . \tag{2.26}$$

[2] Different NIR-penetration depths have been discussed in literature recently, especially for the nearly free-electron metal magnesium [70, 71]

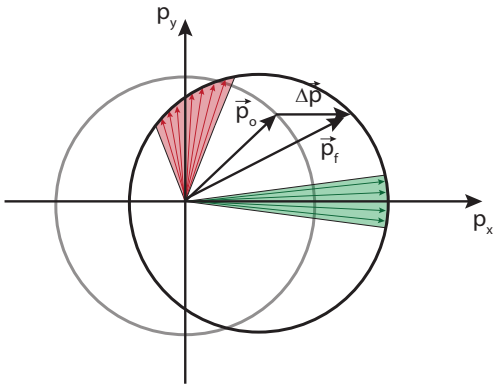

Figure 2.8: Shift of the electron momentum cone within attosecond streaking under influence of the external NIR-field, which is polarized in the x-direction here. The cone is shifted in its total by Δp. Depending on the observation direction the detected momentum distribution is either asymmetrically broadened (in p_y direction) or almost unmodified, but shifted (in p_x direction).

From the latter equation it can be reasoned that the modulation of the kinetic energy, as observed in the experiment (Fig. 2.7), is governed by the laser vector field $\mathbf{A}(t)$ at the electron entry time t_0 into the field. The inclusion of a Gaussian envelope electric field as given by equation 2.9 for a vanishing chirp and the inclusion of the ponderomotive energy U_P from equation 2.20, then gives the full description [65] in approximation for $E_0 > U_P$:

$$\begin{aligned} E_{kin,f} = E_0 + 2\, U_P(t_0) \cdot \cos(2\theta) \cdot \sin^2(\omega_L t_0 + \Phi_{CEP}) \\ \pm \sqrt{8 E_0 U_P(t_0)} \cdot \cos(\theta) \cdot \sin(\omega_L t_0 + \Phi_{CEP}) \ , \end{aligned} \tag{2.27}$$

where the different angles between the initial and induced momentum have been explicitly included, ω_L denotes the laser frequency and E_0 the initial kinetic energy of the electrons. The final energy therefore exclusively depends (apart from the constant laser parameters) on the angle of detection θ measured relative to the direction of the laser polarization (Fig. 2.7 b) and the time t_0, at which the electron enters the laser electric field. The final electron momentum distribution is illustrated in Fig. 2.8, where an isotropic initial distribution is assumed [3]. In this case, the electrons are initially distributed over a sphere of constant momentum, which subsequently is shifted in its entirety by interaction with the NIR-field [65, 12]. Depending on the sampling direction, the final electron distribution can be quite different. For detection around an angle of $\theta = 90°$, which means perpendicular to the laser polarization, the shift of the sphere causes an asymmetric and significantly broadened momentum distribution, whereas detection along the laser polarization gives a symmetric distribution with negligible broadening. The latter is the configuration applied in our experiments.

The concept discussed is valid if the duration of the emitted EWP is small compared

[3] Depending on the observed state this, of course, cannot be a general assumption and can be derived from the angular distribution of the photoionization cross-sections [29]

to the fundamental period of the NIR-laser. If the wave packet duration is close to or larger than the laser period, quantum mechanical effects arise, which appear as interference of electrons experiencing the same momentum shift in the interaction with the laser field [72, 73]. Thus, with increasing EWP duration gradually sidebands build up in the observed spectrograms, which are spaced by a multiple of the NIR photon energy $\hbar\omega_L$. The emergence of these interference effects cannot be explained within a classical theory.

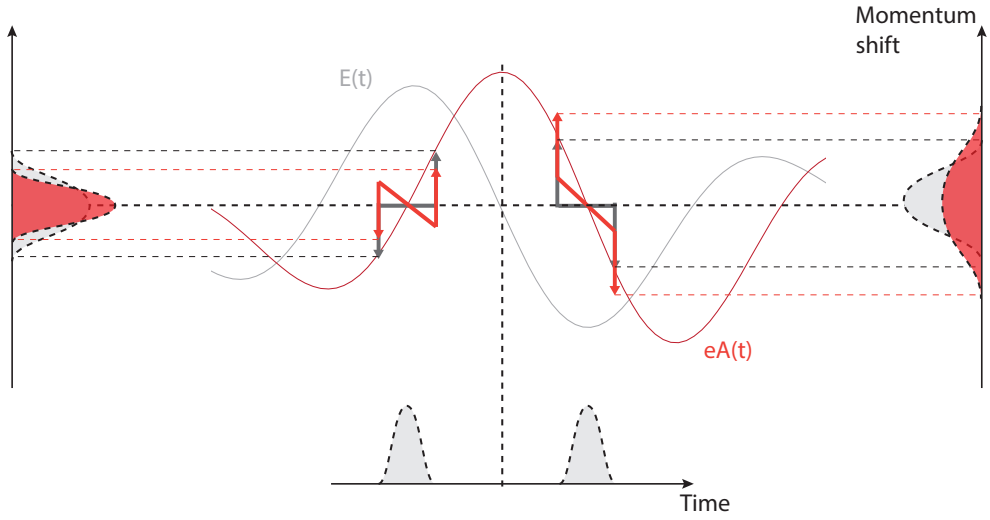

Figure 2.9.: Illustration of the periodic broadening and narrowing of the momentum distribution induced by interaction with the NIR field. The field induces a time dependent momentum shift over the attosecond pulse, as indicated by arrows. For an unchirped pulse (marked in gray) the momentum shift changes its sign over the pulse, leading to a pulse broadening. A linear frequency sweep (i.e. chirp, orange) either enhances the pulse broadening originating from the additional momentum shift by laser interaction or leads, in contrast, to a narrowing of the wavepacket distribution.

In a more elaborate description, one has to consider the process in terms of electron wavepackets, interacting with the laser field after the primary emission. In this regard, a quantum mechanical approach is necessary, which will be described in detail in section 5.1.3. The measured spectrograms (Fig. 2.7) noticeably resemble the spectrograms that are derived from traditional frequency resolved optical gating (FROG)-measurements [74, 75]. Therefore, FROG-type algorithms can be applied in a standard manner to reconstruct the emitted EWPs (section 5.1.3). Since the measured spectrograms deliver the full amplitude and phase information, it is also possible to derive the chirp of the emitted wave packets [25, 69]. Comparison of the streaking of an unchirped and chirped EWP (Fig. 2.9) reveal that a chirp can be

identified through a modified linewidth behavior, mostly in the zero crossings of the laser vector potential. As can be seen in Fig. 2.9, the interaction with the vector potential leads to a broadening of the momentum distribution for an unchirped pulse. If the initial momentum distribution, however, is carrying a linear frequency sweep as for a linearly chirped pulse, the final momentum distribution exhibits a narrowing or broadening in the zero crossings depending on the actual slope of the vector potential. This periodical narrowing and broadening of the spectral peaks can be used to derive the actual chirp of the EWP.

2.4.1. Theory of attosecond streaking

Until recently several authors have taken part in the quest of creating a self-contained theory of attosecond streaking spectroscopy with methods ranging from a classical transport theory to a one-step treatment of the XUV photo-release. The debate is still ongoing regarding the role of the mean free path as part of inelastic/elastic scattering contributions as well as the escape depth [29, 76], the influence of different localization of core and conduction band electrons[28, 77, 26], the NIR-skin depth σ_L[78, 77, 29, 28] or interband bulk transitions [79] in the creation of the streaking delay ($110 \pm 70\ as$) as observed by Cavalieri [17].
In particular, Lemell et al. performed predominantly classical calculations with the inclusion of quantum effects for the scattering process [29, 76]. While explicitly including the different localization characters of W 4f and conduction band electrons for the W(110) surface, Lemell et al. ascribe the main contribution to the streaking delay to the different escape depth of the electrons as well as to inelastic scattering inside the solid. Furthermore, according to Ref. [29] the group velocity could influence the delay depending on the XUV photon energy, even though no influence could be identified for the employed excitation energy of 91 eV. The retrieved streaking delay underestimates the experimental result by predicting an average delay of 33 as, while the influence of the NIR-field inside the solid on the delay was estimated to be rather small ($\approx 10\ as$).
In [26], Krasovskii et al. modeled the effect of the band structure on the observed delay by solving the time-dependent Schrödinger equation and explicitly including the electron Bloch nature. They predicted that, for large excitation depths, electrons in a final state far away from the band gaps give a delay of the streaked spectrogram in comparison to a free electron streaking, since these electrons are faster as a result of the lower crystal potential compared to the vacuum. In the vicinity of a band gap the dispersion relation is giving an opposite effect, i.e. a lower group velocity, and an advance (or antecedence) compared to a free electron streaking. Inclusion of the escape depth causes the shift in delay to approach zero in the regions away from the band gaps, while the effect of advance near the band gaps still pertains.

According to Krasovskii et al. this effect should be visible for the experiments on W(110) exhibiting band gaps near 58 and 91 eV. Moreover, it was concluded that even for the first atomic layer a notable shift in the streaking delay can be expected, since the larger bulk density of states (DOS) in the vicinity of the band gaps is shifting the electron back into the solid initially. Thus, even an electron emitted from the first layer must have spent some time in the bulk.
In a different approach [28] Kazansky et al. stated that the picture of a static band structure cannot be applied and the time is too short for the group velocity to evolve. In this model, the nonstationary Schrödinger equation was solved in the rotating wave approximation for a one dimensional slab of metal. The streaking field inside the metal was completely neglected and the potentials for the electron-lattice interaction and the electron-hole interaction were included for core electrons, while the electron-hole interaction given by a screened Yukawa potential was omitted for delocalized electrons. Within this model, electrons with an energy of $E = 2$ $a.u.$ and $E = 3$ $a.u.$ were predicted to give a time difference of only 12 as and the difference in the effective potential for the two energies was expected to be negligible. The final relative delay between core and conduction band electrons was calculated to be 85 as in good agreement with the experiment. Notably, in this work the delay shift is only produced as an effect of the different localization of the electrons.
Similar, Zhang et al. [78, 77] proposed that the mean free path and, particularly, the different localization in terms of interference effects for core electrons emitted from different layers in the solid are the origin of delay. The initial state wave functions were described by Bloch waves and the final states were represented by damped Volkov waves. The NIR-intensity inside the solid was kept constant until 5 Å. Upon further examination, the dipole matrix element, as part of the photoelectron transition amplitude, was split into two parts: A form factor and an interlayer structure factor. Zhang et al. concluded that the interlayer structure factor vanishes for the conduction band electrons, though it is still pertaining for the core electrons. This difference was attributed to the observed delay difference. Zhang et al. also stated that the mean free path defining the escape depth of the electrons affects the final delay. Thus, for smaller escape depths the relative delay between core and conduction band electrons also diminishes, continuing until the delay vanishes for the emission from the first atomic layer in this model. The calculations can reproduce the experimental results of 110 as for a mean free path set to a value of 5 Å.
In strong contrast to theories ascribing the delay solely to a localization effect, recent measurements on magnesium [18] showed no significant core-to-CB-electron delay, despite its high delocalization of the valence band states. If the electron localization were to play a dominant role in the delay, the delay for the nearly-free-electron-like metal magnesium should fit even better to the corresponding theoretical, localization-based values [28, 78, 27] than that of tungsten, which has an at least partially localized valence band due to the contribution of the 5d-electrons. The use of magnesium is also beneficial, since the free electron character of the metal leads to

an efficient screening of the NIR-field at the substrate surface thereby fulfilling one of the major requirements of the attosecond streaking technique. The experiment gives a relative delay between valence and Mg 2p states of 5 ± 20 as, which in Ref. [18] has been attributed to a cancellation effect between different group velocities and escape depths of the electrons in a simple free-particle-like propagation model. Stimulated by the experimental findings, Borisov et al. recently conducted calculations on magnesium ascribing the vanishing delay to the influence of resonant interband bulk transitions, while still retaining the different localization character as the main effect [79]. The model employed in the calculations is based on the previous model by Kazansky et al. [28] with a different potential for the electron-lattice interaction. The original potential by Chulkov was modified to include the orthogonality constraint respective to the core electrons. The new potential is now able to create notable interband transitions as a result of the higher harmonics in the potential itself. According to Ref. [79] the observed (vanishing) delay is a result of the interplay of the nonresonant surface emission and the resonant bulk interband transitions, which leads to a localized emission of electrons quite similar to the emission of the Mg 2p core electrons. The inclusion of the electron mean free path decreases the influence of the otherwise dominant bulk transitions, but is still strong enough as to yield an average delay of 16 as according to Borisov et al.. This value fits the experimental data within the experimental uncertainties.

In summary, several theoretical models have been established in this field leading to a controversy regarding the origin of the delay. In particular, either localization induced or band structure related effects have been proposed. Moreover, the theorists also act on different assumptions concerning the role of the band structure, the mean free path or the screening of the NIR-field in the first layers of the material. Especially the latter is difficult to define, since the validity of the Fresnel equations in this microscopic regime is not obvious. In fact, with the experimental data obtained so far, it is difficult to clearly favor one of the existing theories or to clearly define, how far and to which percentage localization or band structure related effects play a role. In this thesis, an additional contribution is identified that is able to modify the observed delays notably: the XUV-chirp. Next to the efforts to measure absolute electron travel times, where a cancellation of effects concerning the delay is no longer possible, this could stimulate theoretical efforts to gain further knowledge of the fundamental electronic processes.

Chapter 3.

Experimental setup

The discussion presented above showed that the efficient generation of attosecond pulses by HHG is in need of intense, CEP-stabilized ultrashort NIR-driving pulses. As pulses in the 5 fs range can now be routinely produced in Ti:sapphire laser systems [80], for the generation of high intensity, sub-4 fs pulses one has to resort to chirped pulse amplification (CPA) [81] as well as pulse compression in time by means of hollow-fiber compression [82] and chirped mirrors [83]. Besides, the stabilization of the laser carrier envelope phase (CEP), which is a crucial point in the generation of reproducible, isolated attosecond pulses, has been made possible through the findings of Hänsch and coworkers [21, 84]. These methods will be discussed in detail in the following sections, followed by a description of the experimental setup regarding the HHG, spectral filtering, the preparation- and experimental- chamber, the latter in which attosecond streaking spectroscopy is conducted.

3.1. The laser system

The laser system is built up on a Ti:sapphire laser oscillator (Femtosource Compact Pro, Femtolaser GmbH) pumped by a Verdi $Nd : YVO_4$ continuous wave (CW) pump laser (Coherent) at a wavelength of 532 nm. Chirped mirrors [83] inside the resonator reduce dispersion already within the cavity, which then allows the generation of 6 fs, 4 nJ pulses at a repetition rate of $\approx$ 71 Mhz and a center wavelength of 750 nm.

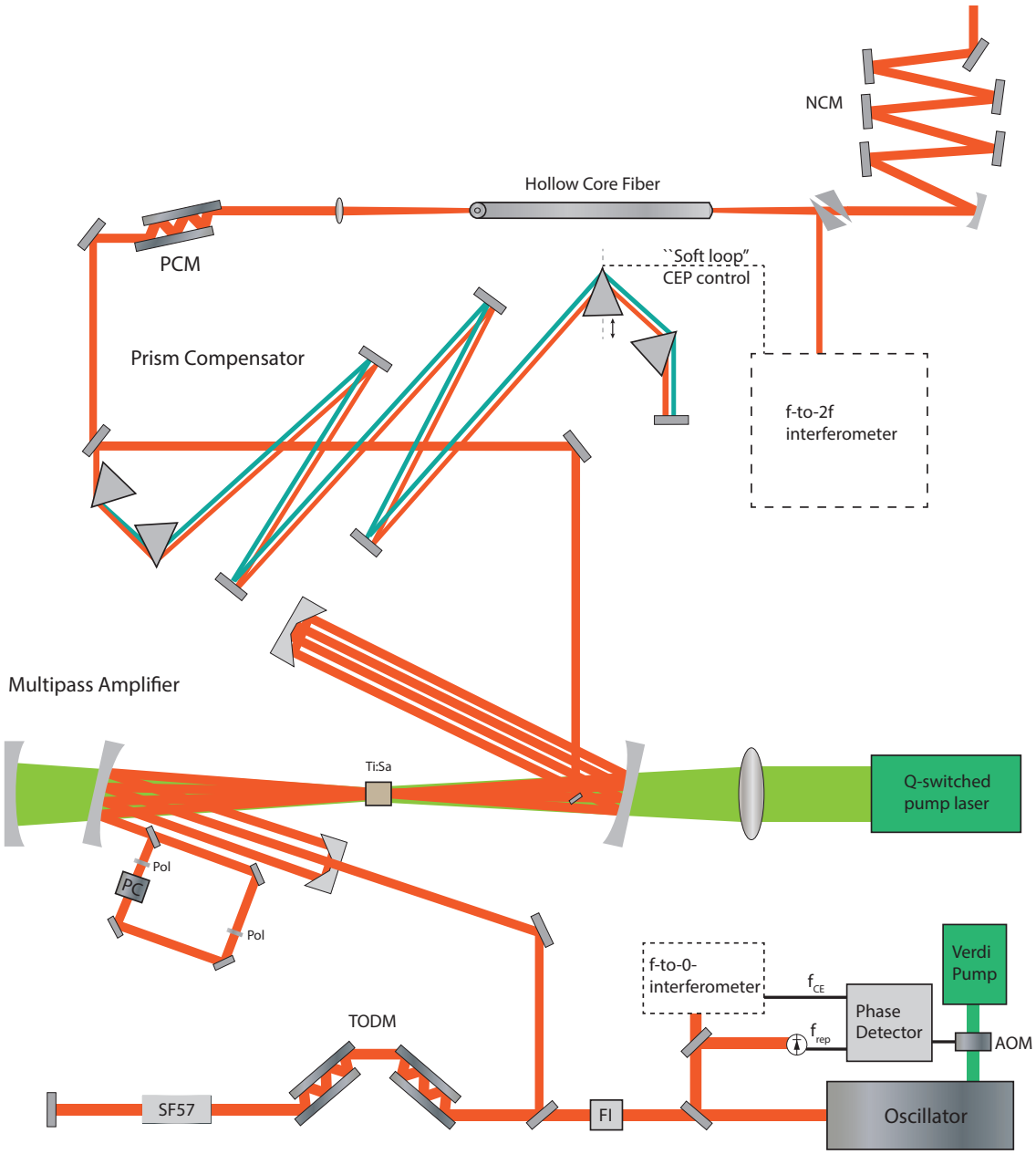

Figure 3.1.: Design of the Laser system producing sub 4 fs, 400 μJ pulses with a repetition rate of 3 kHz: (AOM) Acusto-optical modulator, (FI) Faraday isolator, (TODM) third-order dispersion mirrors, (PC) Pockels cell, (Pol) Polarizers, (PCM) positively chirped mirrors, (NCM) negatively chirped mirrors. The pulse generation is accomplished in three steps: i) the amplification of pulses in a multi-pass amplifier, ii) compensation of chirp in the prism compensator and finally iii) spectral broadening of the pulse by focusing into a hollow core fiber.

In order to increase the pulse energy, the laser light is guided into a multi-pass amplifier. Since the mode-locked fs-pulses would rapidly exceed the damage threshold of the amplifier crystal, the pulses have to be stretched in duration before entering the amplifier. This procedure, also dubbed chirped pulse amplification (CPA), is realized with a block of flint glass preferred for its smooth overall dispersion. The positive chirp, introduced during propagation through the glass, results in a stretched pulse of approx. 15 ps duration. Before entering the multi-pass amplifier the light propagates through a Faraday-isolator, which prevents back-reflections or other disturbing influences from entering the oscillator, and undergoes several reflections on third order dispersion (TOD) mirrors, which pre-compensate higher order chirp accumulated during the amplification process. In the following stage the laser beam executes nine passes through the amplifier, which is pumped by a *Nd:YLF* pump laser (Photonics Industries) at 532 nm. The multi-pass amplifier consists of opposite retro-reflectors, which focus the NIR- and the pump laser beam on a cooled Ti:sapphire crystal. A Pockels-cell limits the repetition rate of the laser to the final value of 3 kHz to increase the overall gain acquired by the amplified pulses and to prevent the amplification of unwanted spectral contributions. Since amplification occurs with a limited gain bandwidth as defined by the Ti:sapphire crystal, the amplification of the spectral wings can be weaker than that of the pulse center, which results in gain narrowing. A reversed Gaussian filter with a higher transparency in the region of the spectral wings is introduced into the beam path to reduce this effect. The amplified pulse energy now reaches up to a value of 1.6 mJ. In the next step, the temporally broadened pulses need to be re-compressed, which is achieved with a prism compressor introducing negative chirp. The compressor consists of two prism-pairs, each arranged in Brewster angle configuration. The prism-pairs are known to introduce a negative chirp to the pulses, whereupon the chirp is usually overcompensated to prevent the occurrence of self phase modulation (SPM) within the last prism. In this case, it was found that SPM would lead to spectral narrowing [85]. Therefore, the final compression is realized outside the prism compressor through 14 reflections of positive chirped mirrors (PCM). This results in a pulse duration of 23 fs at a pulse energy of 1.1 mJ.
Generation of shorter pulses is now only possible by increasing the overall bandwidth. This can be achieved by induction of SPM, which is able to generate new frequency components in a non-linear process by introduction of an intensity dependent phase. In our setup, SPM is initiated by focusing into a 1 m long hollow-core fiber [82] with an inner diameter of 260 μm that is filled with 1.8 *bar* of neon, enabling the creation of a supercontinuum between 400 and 1000 nm. Piezo-driven mirrors guarantee a precise coupling into the fiber. This system now allows the generation of sub-4 fs, 400 μJ pulses at a rate of 3 kHz. Finally, a pair of wedges allows a fine tuning of the pulse's chirp, which is an important quantity regarding the transfer of the NIR-pulse chirp to the XUV-pulses generated within HHG, as discussed in section 2.3.

3.1.1. Carrier envelope stabilization

As already proposed in 1978 by Hänsch [84], the laser oscillator itself represents a frequency comb, which in turn can be used to measure frequencies. In view of extreme nonlinear optics, such a "ruler" in frequency domain is used to measure changes in the carrier envelope phase (CEP), which has been found to introduce dominant changes for pulses near the single cycle regime. The comb structure arises from the periodicity of the generated laser pulses separated by the round-trip time T within the laser cavity [86, 22]. The overall electric field of such a pulse train can then be described in terms of equation 2.9 with a now periodic envelope $A(t)$. As any periodic function can be described by a Fourier series, one receives [22]

$$E(t) = \sum_{n=-\infty}^{+\infty} A_n \cdot e^{-i(\omega_0 + n\omega_r)t} + c.c. \tag{3.1}$$

with time independent coefficients A_n, the central carrier frequency ω_0 and the laser repetition rate ω_r [1]. The spectral representation of the above equation represents a series of delta functions separated by the laser frequency ω_r, namely a frequency comb (as depicted in Fig. 3.2). Inclusion of the laser CEP now shows that its change $\Delta\Phi_{CEP}$ shifts the whole frequency comb by a small value ω_{CEP}, where both quantities are connected by

$$\omega_{CEP} = \Delta\Phi_{CEP}/T = (\Delta\Phi_{CEP}/2\pi) \cdot \omega_r \ . \tag{3.2}$$

Each mode n can then be described as

$$\omega_n = n\omega_r + \omega_{CEP} = (n + \Delta\Phi_{CEP}/2\pi) \cdot \omega_r \ . \tag{3.3}$$

As mentioned before (equation 2.15), the CEP tends to shift from pulse to pulse already within the laser cavity as a result of the different laser group- and phase-velocities. The CEP stabilization mechanism is devised to lock this phase term by application of a f-to-0 interferometer ("fast-loop") and a f-to-2f interferometer ("slow-loop"). The former compensates fast changes arising already in the laser cavity, e.g. from mechanical vibrations or thermal effects, while the latter compensates low frequency changes of the CEP and of the pulse's chirp after the light has passed the pulse-amplification and -compression stages. In the present setup, the fast loop is based on difference frequency generation (DFG), which is accomplished by focusing into a periodically poled lithium niobate (PPLN) crystal. DFG between modes m and k is then governed by the frequency comb

$$\omega_{DFG} = m\omega_r + \omega_{CEP} - (k\omega_r + \omega_{CEP}) = (m - k) \cdot \omega_r \ . \tag{3.4}$$

[1] The laser chirp has been neglected in this case for simplicity, but it has been shown that the presence of chirp is not changing the basic statements made here [22]

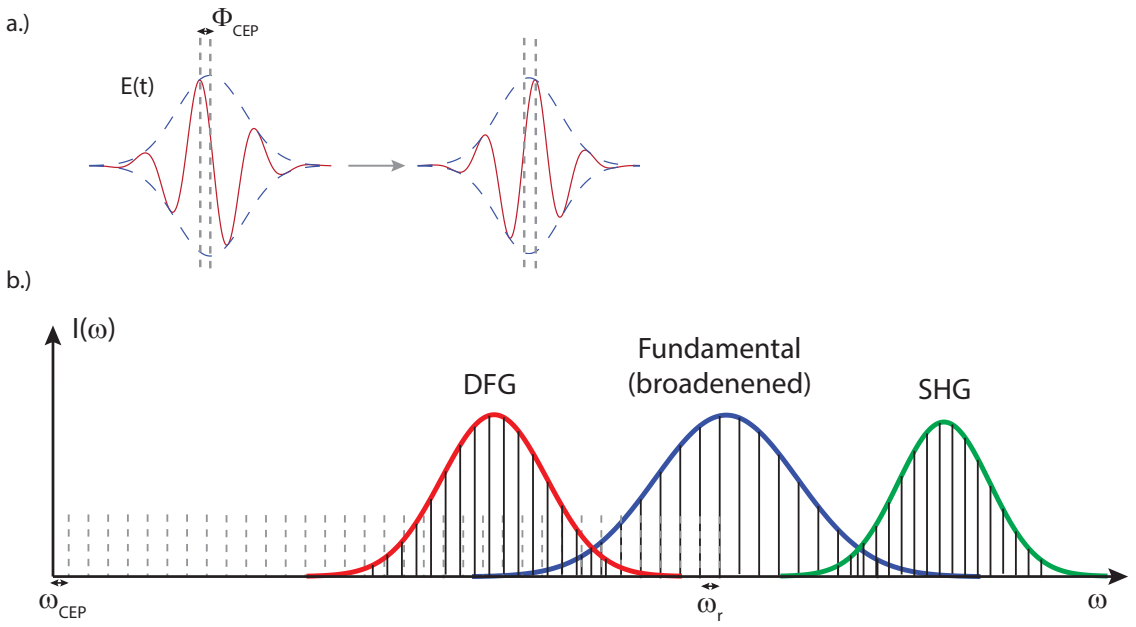

Figure 3.2.: a.) Illustration of the pulse to pulse change in the carrier envelope phase occurring already within the oscillator, b.) Illustration of the frequency comb generated by a pulse train. In the case of a broadened fundamental, spectral beat notes can be created and monitored by overlap with a lower frequency comb created by DFG or a higher frequency comb (SHG).

Superposition of this comb with the frequency comb of the fundamental light ω_n produces a signal with the beat frequency

$$\omega_n - \omega_{DFG} = (n - m - k) \cdot \omega_r + \omega_{CEP} \ . \tag{3.5}$$

Stabilization of this frequency thus automatically stabilizes ω_{CEP}. The spectral range, in which both combs interfere, is separated from the fundamental after the PPLN-crystal by reflection from a dichroic mirror. The beat signal is then collected by a photo-diode and changes in the CEP are, in the following, compensated by modification of the Verdi pump-laser intensity, which is itself varied by an acusto-optical modulator (AOM). The modulation appears such that stabilization occurs with $\omega_r/4$ yielding the same CEP for every fourth pulse.
Residual variations of the CEP by propagation through the laser system are finally corrected in terms of the f-to-2f interferometer mentioned above [87]. After pulse broadening in the hollow-core fiber, the octave spanning final spectrum is broad enough to be superposed with its second harmonic. Therefore, a part of the beam is split off and focused into a β-barium borate (BBO) crystal, where second harmonic generation (SHG) takes place. The generated frequency comb, as a superposition of

the fundamental with its second harmonic, can be described by

$$2\omega_n - \omega_{2n} = 2n\omega_r + 2\omega_{CEP} - (2n\omega_r + \omega_{CEP}) = \omega_{CEP} \tag{3.6}$$

The signal is then detected by a spectrometer and the position of the appearing fringes in the detected spectrum are stabilized using a proportional integral (PI)-controller that steers one of the prisms in the prism compressor, where more or less glass is then shifted into the beam path to modify the CEP.
The scheme applied here consist of measuring and stabilizing the relative CEP, while the absolute phase remains undetermined. It should be noted, that there are other schemes permitting the measurement of the CEP by focusing into a nanoscale tungsten tip [88] or the measurement of the absolute phase by detection of the ATI electrons in two opposite directions parallel to the laser polarization [89]. The additional measurement of the absolute phase in future measurements could be useful regarding the efficiency of the spectral filtering and, in particular, the residual amount of satellite pulse-contributions in dependence of the CEP.

3.2. The HHG-chamber

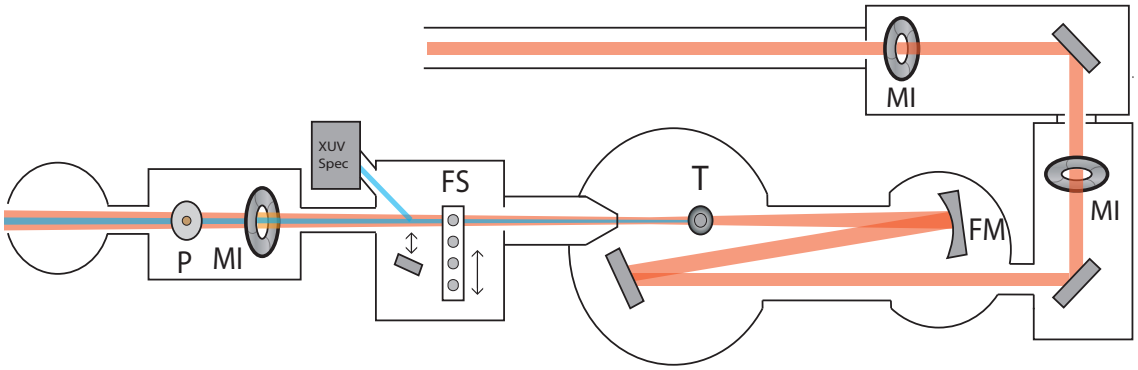

Figure 3.3.: Design of the high harmonic generation (HHG) setup: Two motorized iris' (MI) are used for a reproducible beam incidence and to modify the NIR-intensity. The beam is then focused by a folding mirror (FM) onto a gas target (T). Several filters can be introduced by the filter slider (FS). Another motorized iris at the exit is used to change the NIR-intensity, while a subsequent pellicle (P) is separating the XUV- and NIR- beam (see text). For beam diagnostics, the generated XUV-light can be guided to an XUV-spectrometer by a mirror on a translation stage.

The intense, ultrashort pulses are guided to the HHG chamber under a base pressure of 10^{-4} *mbar*, which prevents additional pulse broadening due to dispersion during

propagation. HHG is realized by focusing into a gas target by a combination of a silver mirror and a concave folding (silver) mirror placed in z-fold geometry. In this way, any influence by astigmatism or other dispersive effects is minimized. The focus length was chosen to be at $f = 550\ mm$ for our experiments, yielding a focal spot laser intensity of $\approx 5 \cdot 10^{14}\ W/cm^2$. The setup offers the possibility to modify the focal spot intensity by insertion of a folding mirror with a different focus length and, at the same time, variation of the target distance to the folding mirror, which is enabled by flexible bellows. The HHG target is a thin, closed cylindrical nickel tube filled with gas, which is usually squeezed to a thickness between $1 - 2\ mm$ to modify the effective gas interaction length. If inserted into the beam path, the high laser intensities create a hole in the tube so that an interaction with the gas is possible. This method has been found advantageous to minimize the gas flow leaving the target and also to limit the maximal laser-gas interaction length. The noble gas neon has been used in this setup, because of its large ionization potential I_P and consequently high HHG-cutoff.
The setup offers two XUV-diagnostic tools that enable the optimization of the generated XUV-spectrum. On the one hand, the direct XUV-spot can be monitored by guiding the XUV-light onto a micro channel plate (MCP) followed by a phosphor screen. A video camera then detects the spatial XUV-spot. The second tool is an XUV-spectrometer that allows the observation of the harmonic cut-off in comparison to the reflectivity of the XUV-mirror. By introduction of a gold-palladium mirror into the beam path, the light is reflected to the XUV-spectrometer. Here, the incident XUV-light is dispersed by a grating, amplified by means of two cesium-iodide covered MCP's (higher XUV-sensitivity) and finally monitored by a CCD device. A 950 nm thick zirconium filter placed directly in front of the MCP/camera-stack prevents NIR-light and any other residual light apart from the XUV from being observed. In HHG, the modification of the gas pressure, the final NIR-laser intensity set by a motorized iris and the target position relative to the laser focus (see section 2.3) allow for an optimization on, first, the smallest and most intense XUV-spot and, second, the position of the plateau in the XUV-spectrum, which should be close to the spectral filter range supplied by the XUV-mirror.
Several filters, placed in a filter slider, can be introduced into the beam path in order to adjust the XUV spectrometer. The filter slider contains a 150 nm thick silicon- and a 200 nm aluminum-filter for the calibration of the spectrometer energy scale as well as 200 nm thick palladium and zirconium filters. The latter are used for optimization and alignment procedures in the main experimental chamber. Upon utilization of the XUV spectrometer, a 450 nm thick high pass filter (zirconium) in front of the slider is moved into the beam path to prevent damage from the subsequent thin slider filters.
As the experiments performed in the experimental chamber require UHV ($< 10^{-10}$ $mbar$) conditions, care has to be taken to reduce the pressure from the HHG- to the experimental chamber by approximately 8 orders of magnitude. Since window

materials, transparent in the NIR as well as in the XUV regime, are not available, differential pumping is required. Therefore, a 600 l turbo pump is placed at the "high pressure" region around the gas target reducing the residual pressure to about 10^{-2} $mbar$. A skimmer, which can be moved in x- and y- direction perpendicular to the laser beam, is further reducing the probability that particles reach the subsequent chamber, just providing a small aperture of 1.5 mm. Consecutive 200 l and 300 l turbo pumps in the next sections suffice to reduce the pressure to approx. 10^{-9} $mbar$, while the last 400 l turbo realizes the final pressure of $< 10^{-10}$ $mbar$.
Before entering the experimental chamber, in the last section, the spatial shape of the generated XUV- and NIR-beam is modified. Another motorized iris is used to modify the overall intensity of the NIR-laser, which exhibits a larger spatial divergence than the XUV-beam. In the next step, the NIR- beam is confined to an outer ring, whereas the XUV-beam is limited to the residual inner diameter. This is realized by a combined filter, which exhibits an outer ring out of a nitrocellulose pellicle, solely transmitting NIR-light, and an inner disk made of palladium or zirconium, blocking any NIR-light while transmitting XUV radiation. At the same time, this method tends to prefer lower divergent, short HHG-trajectories (see section 2.3). For the central XUV energies applied in this thesis, zirconium was used, since palladium is only transmitting energies larger than 100 eV.

3.3. Preparation- and experimental chamber

The final section of the setup consists of two UHV chambers, the experimental- and the preparation-chamber, which are connected by a gate valve. This separation is a standard technique of UHV systems, confining less clean procedures like the preparation or cleaning of the sample to the preparation chamber, while maintaining a good vacuum in the experimental chamber, where the actual measurements take place.
One of the major components of the experimental chamber is the double-mirror stack, the form of which resembles the cross-sectional area of the co-propagating XUV-NIR light (Fig. 3.4). Thus, the double mirror consists of an outer ring that reflects the NIR-light and an inner circular mirror to reflect and spectrally filter the XUV-light. Thereby, a special Mo/Si multilayer coating of the latter defines the reflected bandwidth and pulse shape [64, 63] [2]. The outer mirror is usually coated with 13 nm boron carbide to limit the reflected NIR-intensity to a value of less than 20%, since otherwise, the laser intensity could induce beam damage of the solid samples. The second purpose of the double mirror is to focus the incident XUV- and NIR-light onto the sample, which is achieved by a spherical shape of both mirrors

[2]The XUV-reflectivity of the applied XUV-mirror is described in detail in section 5.1.1

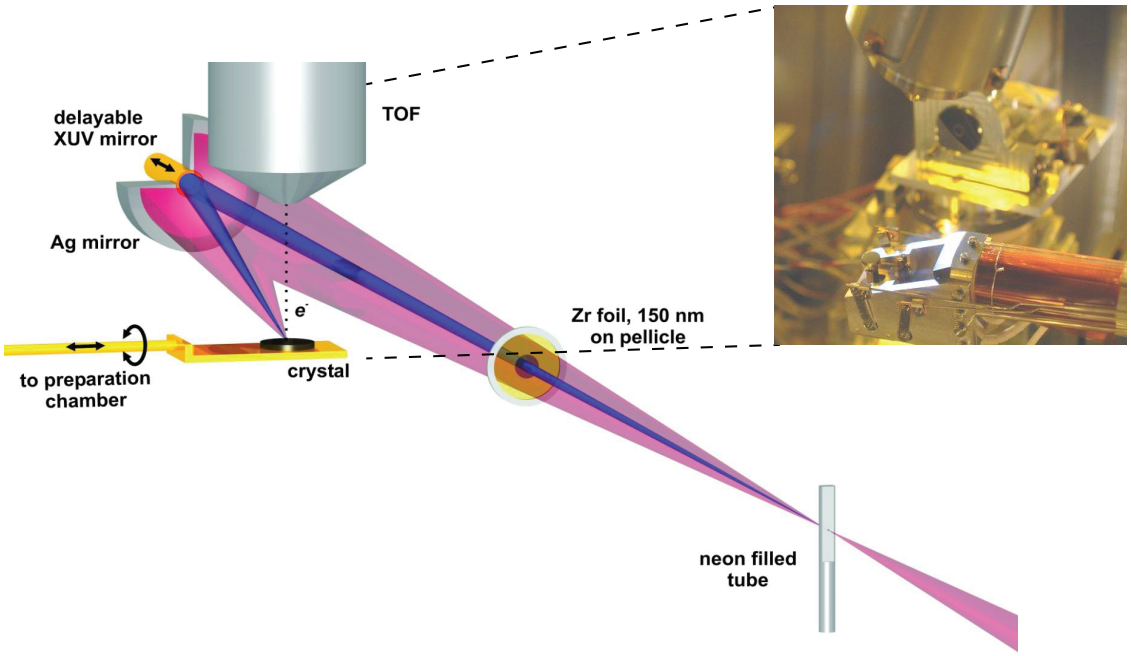

Figure 3.4.: Illustration of the working principle of the double mirror and the separation of the XUV- and NIR- beam, where the XUV-beam is limited to an inner diameter and the NIR-beam to the outer ring. Adapted modified from [17, 90]

(radius of curvature $-250\ mm$). The XUV mirror is mounted on a pin, which is directly connected to a piezo-actuated stage (PI Hera 621) and allows the introduction of a temporal delay between the XUV- and NIR-pulse. The overall range of the piezo stage is 100 μm with a step resolution of 0.2 nm translating to a temporal resolution of 1.3 as. The double mirror is mounted on a stack of piezo-driven stages including a goniometer so that the mirror can be rotated and translated according to the incident beam and sample position. For maintenance, the whole double mirror stack can be retracted from the chamber behind a gate valve by means of flexible bellows. The stability of the whole double mirror stack is rather important, since any mechanical vibrations introduced at this point translate into a timing delay between the XUV- and NIR-pulse, meaning an increased experimental uncertainty. Therefore, a counter bearing is installed in the main chamber, against which the mirror stack is pressed with the support of springs (Fig. 3.5).
The light, incident on the double mirror, is then reflected to the tungsten sample, which is mounted on a x-y-z movable manipulator. The latter allows positioning and transfer of the sample to the preparation chamber. The electrons emitted from the sample are detected by a time of flight (TOF) spectrometer (old spectrometer

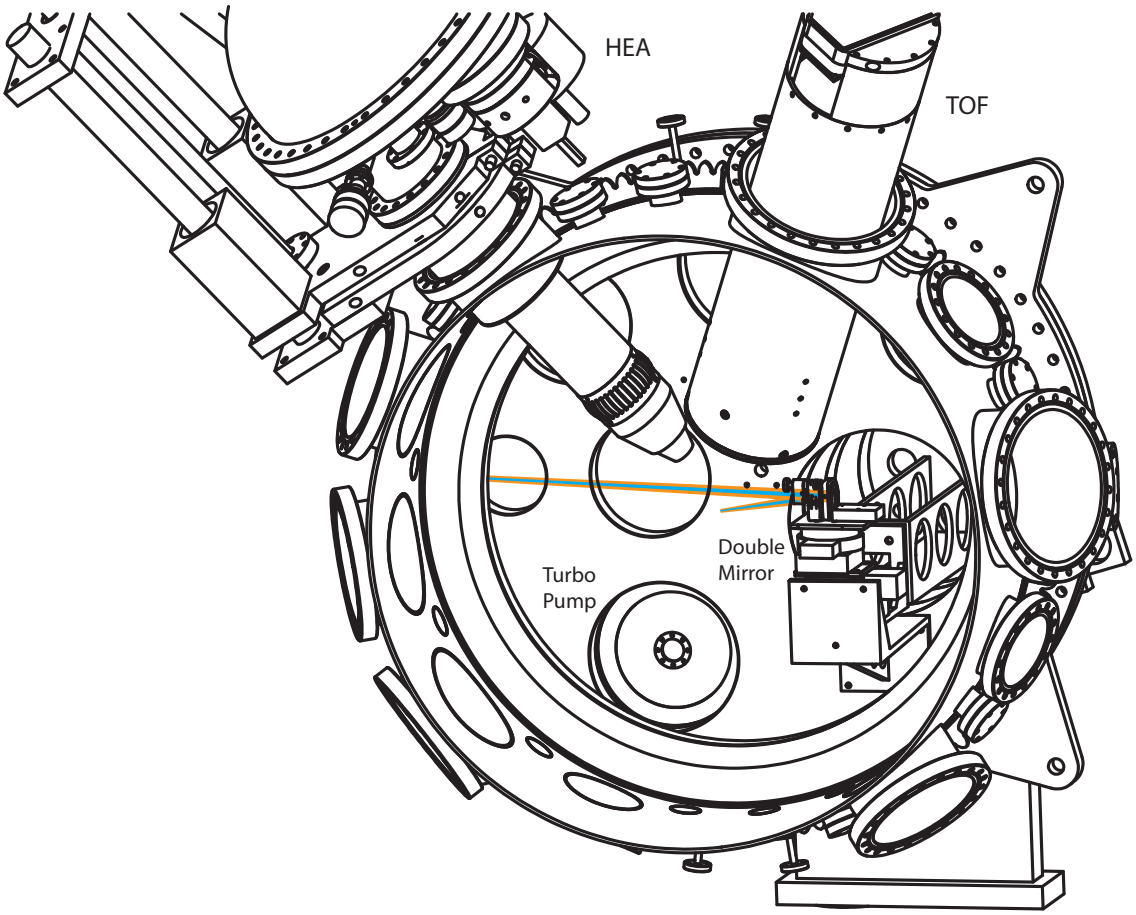

Figure 3.5.: Inside view into the experimental chamber showing the hemispherical analyzer (HEA), the time of flight spectrometer (TOF), the double mirror stack and the pathway of the combined XUV-/NIR-beam.

applied in the measurements: Kaesdorf, Geräte für Forschung und Industrie) or a hemispherical energy analyzer (HEA) (Specs Phoibos 100). Attosecond spectroscopy has been performed with the TOF spectrometer, since it allows the simultaneous detection of a whole spectrum resulting in a higher detection efficiency compared to the HEA, whereas the latter has been used for characterization of the sample cleanness in standard XPS. For this reason also a dual anode Mg/Al Kα - source (PSP vacuum technology) is installed in the chamber. In order to minimize the reflection angle of the double mirror in the horizontal direction, all flanges are tilted by 20°, which allows a sample position closer to the position of the mirror (see Fig. 3.5). This restricts the direction of the sample normal and the E-vector of the light to be also tilted by 20°, i.e. the sample normal and the axis of the TOF coincided with a distance of 3 mm between sample surface and TOF entrance. In order to minimize the NIR reflection, the sample is illuminated under the Brewster angle

($\approx 15°$ against the surface plane).
The tungsten sample can be heated in vacuum up to temperatures of 2500 K by electron bombardment of its backside. The temperature is measured with a tungsten-rhenium (type C) thermocouple, which is directly spot-welded to the side of the sample. The second contact of this temperature measurement is made to a small block, mounted against the sample holder, which allows the measurement of the temperature difference between sample holder and the sample itself, i.e. the thermocouple reference point is at the sample mount, the temperature of which was measured separately. This allowed the use of different thermocouple wires without changing the wiring of the manipulator. In particular, no special thermocouple feedthroughs are necessary.
Two optimization procedures are applied in a standard manner: As mentioned before, first, the XUV-spot of the generated harmonics can be observed on a phosphor screen consecutive to MCP amplification. In the past, the whole chamber has been rotated around its vertical axis to guide the laser beam either onto the XUV-mirror or the phosphor screen. In a recent change, another gold-palladium mirror was installed, which is mounted on a manipulator and can be freely rotated due to motorized screws. A rotation of the chamber to observe the XUV-spot is therefore not necessary anymore, which should increase the reproducibility of the measurements and the lifetime of the equipment. The second optimization procedure refers to the spatial and temporal overlap of the XUV- and NIR-beam. Here, the pellicle is moved out of the beam path letting NIR-light pass in the inner diameter. Next, the light reflected from the double mirror is guided outside the chamber by a mirror and finally, passed through a lens and detected with a CCD camera. As the outer mirror can be independently moved by motorized screws, the spatial overlap can be adjusted this way. The XUV- spot size is generally much smaller than the NIR one due to its smaller divergence assuring a spatial overlap within the measurements. The temporal overlap can now be found by movement of the piezo-driven inner mirror. The simultaneous spatial and temporal overlap can be identified by the appearance of interference rings with the quality of the spatial overlap defined by their symmetry. The temporal overlap can only be determined roughly with this method, but is only used as a starting point to find the overlap in the more precise attosecond streaking measurements.
In the experimental chamber, moreover, a gas nozzle for attosecond spectroscopy in the gas phase and a hot-cathode pressure sensor are installed. The part of the chamber containing the spectrometers can be rotated, which allows to set the XUV-/NIR- angle of incidence onto the sample. This is realized by means of differentially pumped, rotary feedthroughs. The preparation and the experimental chamber are pumped by a 700 l turbo pump each, reducing the pressure to about 10^{-10} $mbar$. The final pressure of approx. 10^{-11} $mbar$ is then achieved by $L-N_2$ cooled titanium-sublimation pumps (TSP) (VAb TVP 40K) installed in both chambers.

The preparation chamber contains a gas doser and a sputter gun for sample preparation, LEED optics (SPECS, ErLeed 100/150) and a load lock system for sample exchange. Since the sample manipulator is fixed to the rotatable front side of the preparation chamber, the whole manipulator arm can be rotated within the preparation chamber to reach every station. Recently, also a mass spectrometer has been installed in a way that the sample can be placed directly in front of it, thus enabling the examination of desorption products upon heating of the sample.

Chapter 4.

Time of flight spectrometry

4.1. Basic principles

The spectrometric detection of electrons emitted through light-matter-interaction is usually devised in terms of an energy analyzer, followed by an amplification of the electron current and its successive detection. A rather simple concept relies on the determination of the electron time of flight (TOF): The kinetic energy of the emitted electrons is obtained by measuring the electron flight time in a field free space inside the spectrometer. Given a starting point of electron emission, one can determine the flight time T to the detector anode, which can then be converted into the electrons kinetic energy granted that the total electron propagation distance S to the detector anode is known. For the propagation in a field-free space, this correlation is simply

$$E = \frac{1}{2} m \, \frac{S^2}{T^2} \tag{4.1}$$

with the electron mass m, whereas the time-to-energy relation of TOF detectors that contain a focusing electrostatic lens system [91, 92] can mostly only be described by numerical trajectory calculations. Since a (temporal) starting point is necessary, common TOF spectrometers require pulsed sources. The TOF technique has been found advantageous, especially for the low intensity measurements in this thesis, due to its ability to monitor the whole energy spectrum at once and its high detection efficiency. The quality of the timing information depends on different parameters, concerning the detector size, detection rate, constant wide-energy transmission of the spectrometer or the possibility of multi-electron detection.

TOF spectrometers most commonly are built up from the following components: An entry cone allowing to place the spectrometer close to the sample, an electrostatic lens focusing the incident electron beam, a field-free propagation space and finally,

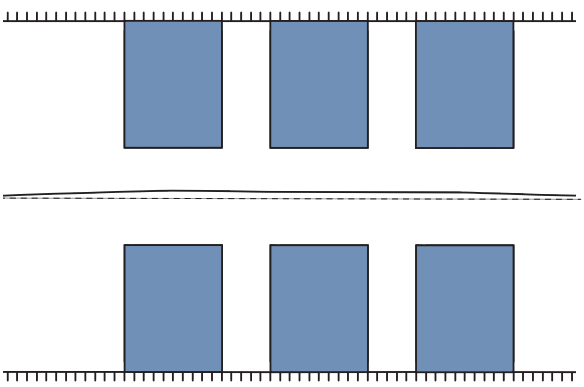

Figure 4.1: Working principle and simulated electron trajectory of a simple electronic lens system consisting of 3 electrodes, where the center electrode carries a large and the surrounding electrodes a small potential.

components to amplify and detect the incident electrons. Each component will be discussed in more detail in the following.

After passing the entry aperture of the spectrometer, the electrons enter the electrostatic lens system, whose purpose is to focus the angularly dispersed electron beam and thereby increase the acceptance angle of the TOF. A simple focusing electric lens (Fig. 4.1) can be constructed by the arrangement of three successive electrodes, where only the center electrode carries an electric potential and the remaining ones hold a zero potential [93, 94, 95]. In the usual case, the center electrode carries a positive voltage, since it comes in hand with a lower spatial aberration compared to a negative voltage electrode [93]. It has been found that systems with open electrodes usually yield a better performance than constructions of consecutive grids, since the latter reduce the transmitted electron flux with each grid and tend to blur the velocity-space mapping giving a larger uncertainty in time [92]. While the application of a lens system drastically increases the electron detection range, it should also be considered that the integrated measurement of a larger angle of incidence at the same time implies, e.g., the averaging over a larger area of the Brillouin zone for the case of photoemission.

At the entry aperture of the TOF spectrometer usually a fine grid at zero potential is installed that prevents any outer electric field from penetrating the space inside the spectrometer as well as to prevent the electric field of the lens from having any influence outside the spectrometer. In this way a clear boundary is achieved by the installed grid.

Past the electrostatic lens system, the electrons pass through a field-free space, which can be defined, for example, also by a grid or an electrode at zero potential. Upon propagation, an initial velocity difference between the electrons is emerging as a time difference, for which reason this section defines the time resolution of the detection to a large extent.

Finally, the propagating electron needs to be detected. Since the direct detection of a single electron is not possible, at first amplification by means of microchannel plates (MCP) is conducted. MCPs consist of millions of micrometer-scale capillaries (channels) commonly made of glass, which are stacked together in a honeycomb-like

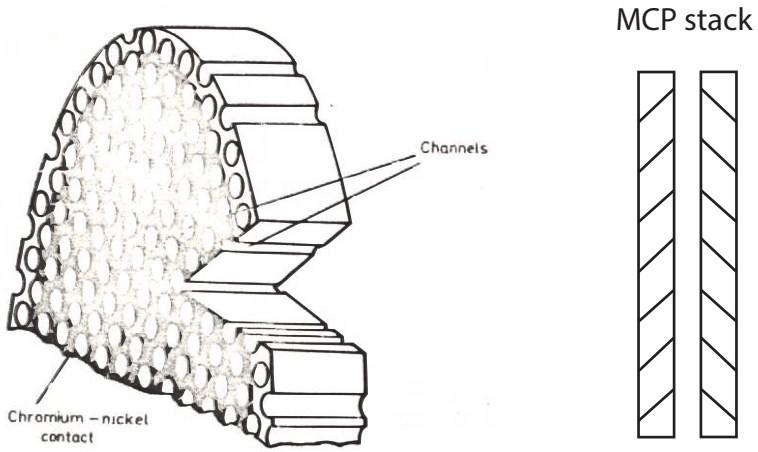

Figure 4.2.: Arrangement of the μm- small channels in a MCP (left side) [96] and the usual arrangement of two MCP's in a V-like constellation of the channels (right side) in order to prevent destructive ion feedback.

structure, as can be seen in Fig. 4.2. The internal of each capillary is coated with a material that has a large secondary electron emission coefficient. An incident electron hitting the channel wall produces secondary electrons, resulting in an exponential rise of the overall electron current upon each further hit. A potential difference of usually a few hundred eV is applied between the front and end part of the MCP to increase this effect. With this method, an amplification about a factor of 10^3 can be routinely achieved. For further amplification, ion feedback is becoming a problem, where residual gas at the output of the MCP is ionized by the outgoing electrons. The produced ions are then accelerated backwards to the front of the MCP and, provided that the acceleration potential is large enough, can them-self induce electron emission upon hitting the channel wall. The reduction of the acceleration potential efficiently prevents ion feedback, since ions now do not obtain sufficient kinetic energy to release secondary electrons. In order to supply the amplification rate of 10^6 that is needed in TOF spectrometers, usually two MCPs stacked in chevron geometry are used. As the channels of each MCP are slightly tilted (e.g. by 10°), in this geometry the MCPs are arranged in a "V-like" constellation of the subsequent channels, as can be seen in Fig. 4.2. Thereby, ions leaving the second MCP are hindered from entering the first MCP. The stacked constellation of the MCPs therefore allows amplification factors of about 10^6. The accelerating voltage between and in the MCPs are usually chosen in such a way that saturation of the individual channels (of the second plate) occurs, which minimizes the statistical variability of the signal due to varying amplification. The relatively high voltages also result in a small electron propagation time within the MCPs so that it can be neglected for the energy conversion. Typical FWHM values of the electron cloud generated from an incident electron lie in the range of $500 - 700\ ps$ depending

on the channel diameter [96]. The electric current impinging on the anode can be estimated according to the simple formula

$$I = \frac{N \cdot e}{t} \cdot N_A \ , \tag{4.2}$$

where N_A denotes the MCP amplification factor, N is the number of incoming electrons and t is the duration, which for one electron is the pulse duration of the generated electron cloud behind the MCPs. For a pulse duration of 1 ns, a single electron accordingly generates a current of $\approx 1.6 \cdot 10^{-4}$ A, which translates to a voltage of 8 mV at 50 Ω. This value is orders larger than the estimated noise at a 50 Ω resistance of ≈ 0.07 mV (for an estimated frequency bandwidth of 5 Ghz). The current is therefore sufficient for the detection of a single electron. The micrometer scale channel diameters in principle also enable to gain the spatial resolution of the detected electron distribution, which is only limited by electrostatic electron-electron repulsion and the channel spread when passing to the second MCP and is usually also in the micrometer scale.
The spatial resolution provided by the MCP can be used to receive the angular distribution of the emitted electrons or to improve the temporal resolution of the spectrometer [97]. The readout of this spatial resolution can, for example, be made with a delay-line anode [98]. Here, a delay-line is arranged in a two-dimensional zig-zag pattern and the signal at both ends of the delay line is measured. When an electronic current is impinging on one point, the temporal difference between the induced signals at both ends of the line is measured, from which one can also calculate back to the initial spatial position. A resolution in two spatial dimensions can then be achieved by the use of two delay-lines, tilted by 90°. As this method delivers timing and position information at the same time, it usually lacks of an appropriate multi-hit capability and longer detection times. Another method is the use of a segmented anode, which relies on the direct read-out of the detector current with an anode divided in individual segments, all connected to their own detection electronics. Here, the time information can be read-out fast and very precisely, while the spatial resolution is given by the size of the segments. As long as different segments are hit, this method offers a good multi-hit capability. In contrast, some TOF spectrometers (e.g. the Kaesdorf-TOF, see below) use solely a single anode, neglecting the spatial resolution.
In the final step, the signal is sent through a pre-amplifier, followed by a timing -discriminator and a time-to-digital converter (TDC). The timing discriminator is converting the analog pulses received from the pre-amplifier to standard logic pulses. In this regard, a rather simple leading-edge discriminator could be used, which starts or ends a logic pulse when the analog pulse's leading edge or trailing edge is passing a pre-defined threshold, respectively. The arrival time of the electron is then derived from the point in time, where the leading edge has passed the threshold. For this system, timing-walk tends to be a problem, which decreases the timing resolution (Fig 4.3 a). It can be described in terms of two analog pulses with the same

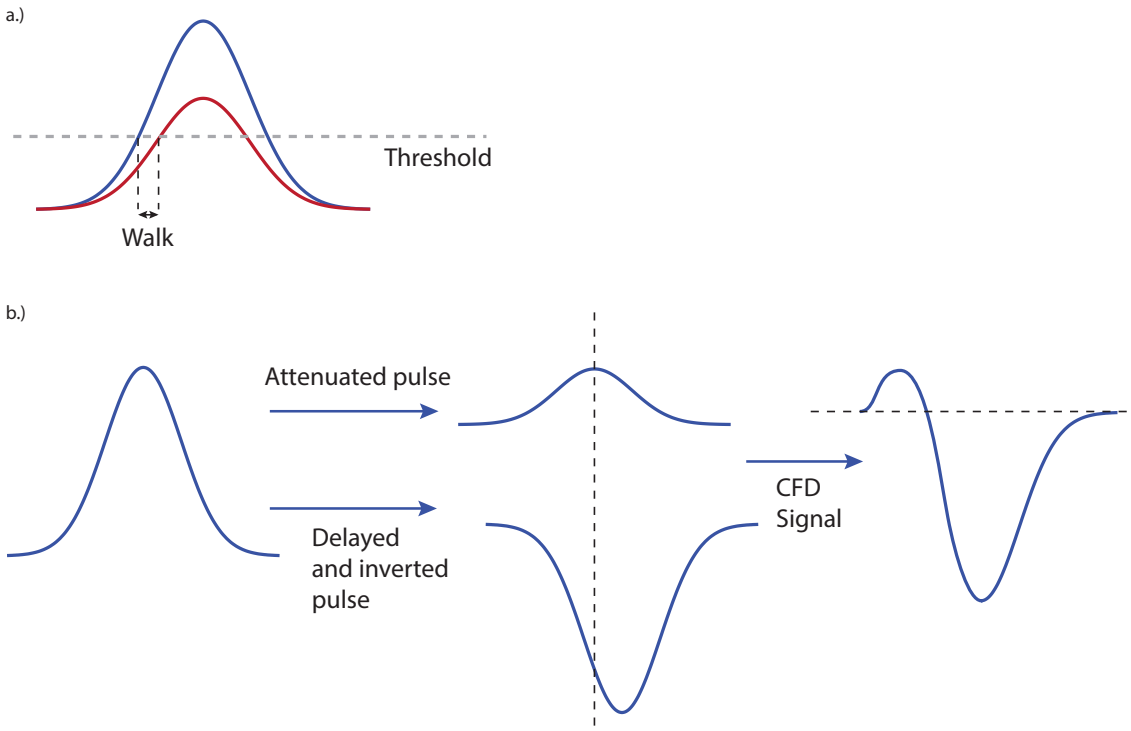

Figure 4.3.: a.) Illustration of timing walk occurring within a leading edge discriminator: Two pulses with the same timing, but different amplitudes, yield a different timing signal, since the threshold is reached at different instants. b.) Processing of the incoming pulse in a contant fraction discriminator. Two copies of the pulse are created, where one is attenuated and the other one is delayed and inverted. The recombined signal of the two pulses yields the CFD signal.

shape, but different amplitudes. The pulse with the larger amplitude will pass the threshold at an earlier time resulting in a differently timed output pulse compared to the lower amplitude analog pulse. This behavior can be prevented by the use of constant-fraction discriminators (CFD) [99, 100]. Here, the input signal is divided into two identical copies, where one signal is attenuated and the other is inverted and delayed by a pre-defined value (Fig 4.3 b). Attenuation and delay are chosen in such a way that the combination of the two pulses experiences a zero-crossing at the position of the original pulse maximum. Since the position of this zero-crossing is mostly independent on the pulse amplitude, this point in time allows a good timing discrimination with a small influence of timing-walk. A residual uncertainty of about 30 *ps* still remains from jitter. In our setup a self-made CFD has been used, the electronic build of which is given in Fig. 4.4.
Finally, the standard logic pulse is send to a TDC, which can be viewed as a clock counter. In principle, the time is measured by a high frequency clock and subse-

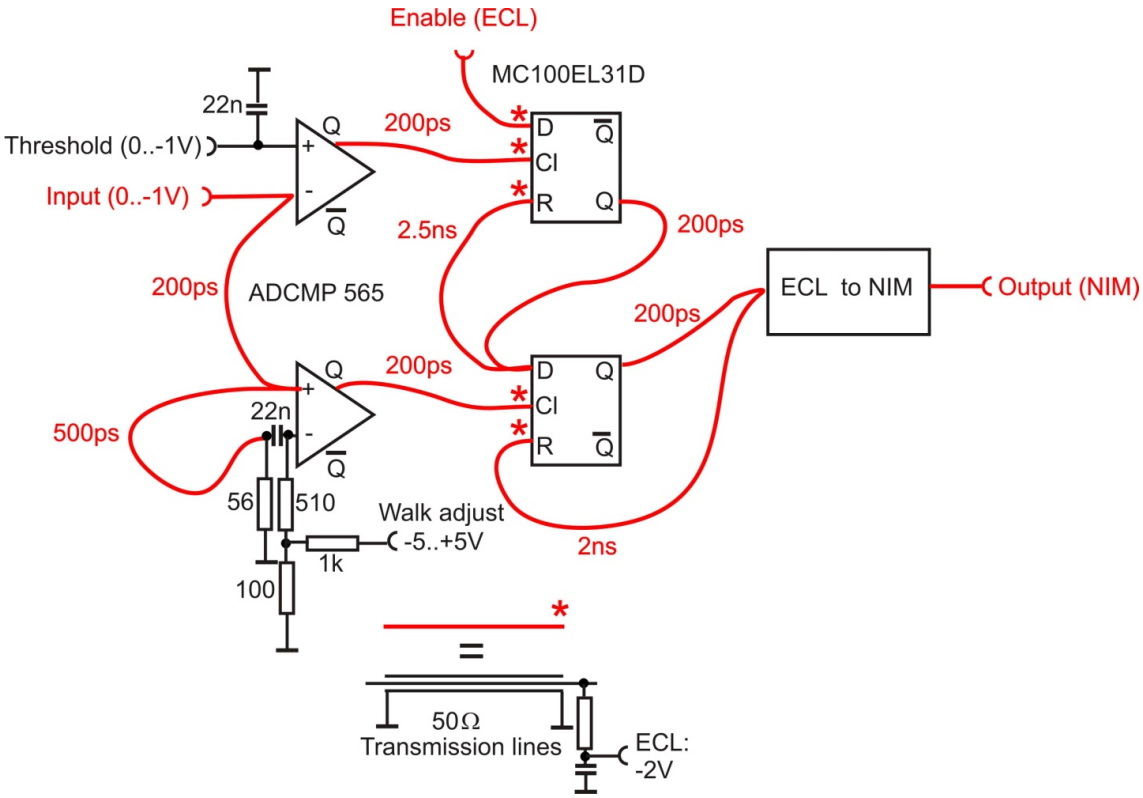

Figure 4.4.: Schematic of the self-made CFD, consisting of a double comparator (ADCMP 565, ECL logic), two D-type flip-flops (MC100EL31D, ECL logic), and an ECL-to-NIM converter. Input pulses larger than the preset threshold arriving at the upper comparator set the upper flip-flop. The analog input signal is then sent to the second comparator, first to its plus input, and then with a variable delay of 500ps to its minus input. The zero crossing of the resulting signal triggers the second flip-flop, provided the first has been set. The ECL output of this second flip-flop is then converted to a 2.2 *ns* NIM pulse, digestible by the data acquisition electronics that follows.

quently counted in a register. At this point, the dead-time of the TDC plays an important role, since after detection of one electron, the detection of further electrons is prevented for a certain period of time (typically in the nanosecond range). In the most extreme case, this can create artificial peaks in the detected spectra i.e. in the tail of a saturated peak. Nowadays, TDCs in combination with constant-fraction discriminators allow the determination of electron arrival times with a precision down to the 30 *ps*-range.

In the field-free case, the energetic uncertainty of the spectrometer can be estimated. As is clear from equation 4.1, the energy has two sources of error: the spatial

and temporal determination uncertainty, ΔS and ΔT. While ΔT is given by the current TDC/CFD-uncertainty of around 100 ps, the spatial uncertainty arises from propagation differences of electrons with the same kinetic energy. For example, angular dispersed electrons starting from the same point travel a different distance when detected with a planar anode. This path difference for equally fast electrons gives rise to a spatial uncertainty ΔS. Derivation of 4.1 now allows to determine the influence of both errors as

$$\frac{dE}{dT} = \frac{1}{2}m \cdot (-2)\ \frac{S^2}{T^3} = -2 \cdot E \cdot \frac{1}{T} \tag{4.3}$$

$$\frac{dE}{dS} = \frac{1}{2}m \cdot (2)\ \frac{S}{T^2} = 2 \cdot E \cdot \frac{1}{S} \tag{4.4}$$

so that the total error can be written as

$$\frac{\Delta E}{E} = \sqrt{\left(\frac{2\ \Delta T}{T}\right)^2 + \left(\frac{2\ \Delta S}{S}\right)^2}\ . \tag{4.5}$$

The spatial error ΔS can be set to zero when a spherical anode is used, for which case, however, also the MCP's have to be spherical. Such spherical MCP's can be custom-built, but are (besides their high price) known to be quite delicate in their handling and the integration into the setup. Therefore, usually planar anodes with comparably large propagation distances are used to minimize the spatial uncertainty.

4.1.1. The Kaesdorf TOF-spectrometer

Before giving a detailed description of the simulations and setup of the newly built TOF-spectrometer, the former spectrometer shall be depicted shortly. It is a commercial TOF-system (Kaesdorf, Geräte für Industrie und Forschung) with a drift-length of 425 mm providing an electrostatic lens for electron beam focusing. The entry cone of the spectrometer is placed at a distance of 3 mm in front of the sample. The aperture itself has a diameter of 3 mm, which supports a maximal acceptance angle of 22°. The electrostatic lens allows an accepted angle of incidence between 12° and 18° in the energy range of $40 - 150\ eV$. The lens voltage can be freely varied up to a value of 2.5 kV, but is usually limited to voltages lower than 800 V for the kinetic energies of interest ($< 150\ eV$). After propagation in the drift tube, the electrons are accelerated by a fixed potential of 1000 V in a 69 mm long section divided from the drift tube by a fine grid. Finally, the electrons are multiplied by a stack of two MCP's in chevron geometry with a channel diameter of 5 μm and detected with a planar, single anode. The anode signal is then send to a self-made pre-amplifier (5 GHz, 40 dB), converted to logic pulses by a commercial CFD (Ortec

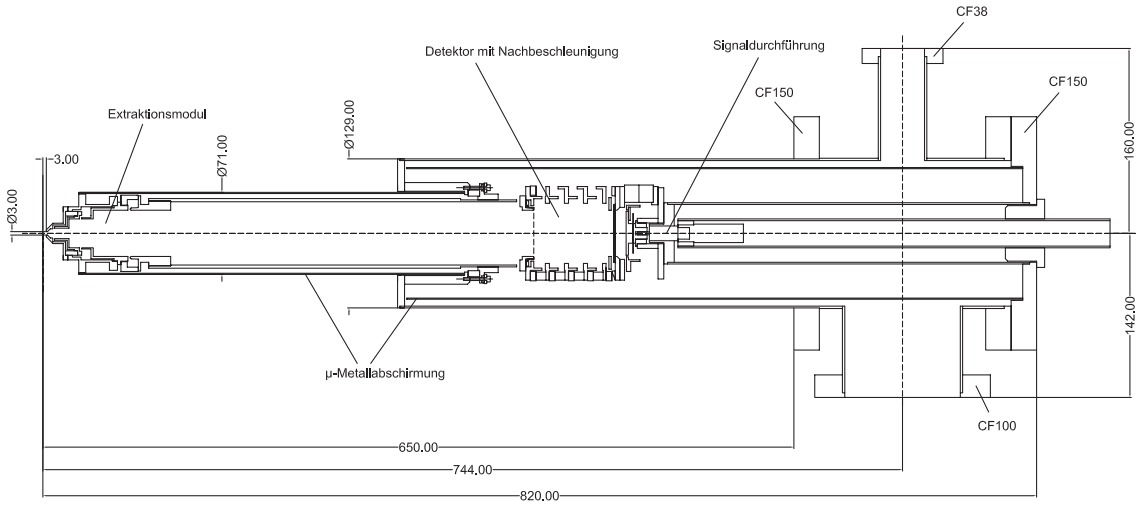

Figure 4.5.: Setup of the Kaesdorf TOF spectrometer, showing the electrostatic lens system and the post acceleration section.

9307) and counted with a TDC supplying an absolute temporal resolution of 100 ps and a dead-time of 3 ns (FAST ComTec P7889). The system is able to provide a total energy resolution of $\Delta E = 1.5\ eV$ at a kinetic energy of 150 eV.

The time-to-energy conversion for this spectrometer can, as mentioned before, not be realized by the solution of analytical equations as, e.g., given by equation 4.1. Therefore, the manufacturer has provided time-to-energy conversion tables for each lens voltage calculated by numerical trajectory analysis through the SIMION software package (Scientific Instruments and Services). The kinetic energy for each arrival time is obtained from these conversion tables, while, at the same time, each intensity value has to be rescaled according to

$$dI = \dot{I}\ dt = \dot{I}\ \frac{dt}{dE}\ dE\ . \tag{4.6}$$

Hence, every intensity value of our data is rescaled by the factor $|\frac{dt}{dE}|$ to account for the conversion $dt\ \rightarrow\ dE$. Finally, a linear interpolation of the data matrix allows projection onto an equally spaced kinetic energy scale.

Mostly two problems have been identified, which arise in the current TOF-setup. The first problem is the rather strong energy dependent transmission of the electric lens system, which was measured for the Kaesdorf spectrometer on a Si(111) sample for different lens voltages as can be seen in Fig. 4.6. The measurement of the intense Si- Auger lines enables to detect the signal transmission of the TOF-lens as a measure of the kinetic energy dependent acceptance angle of the TOF. The transmission

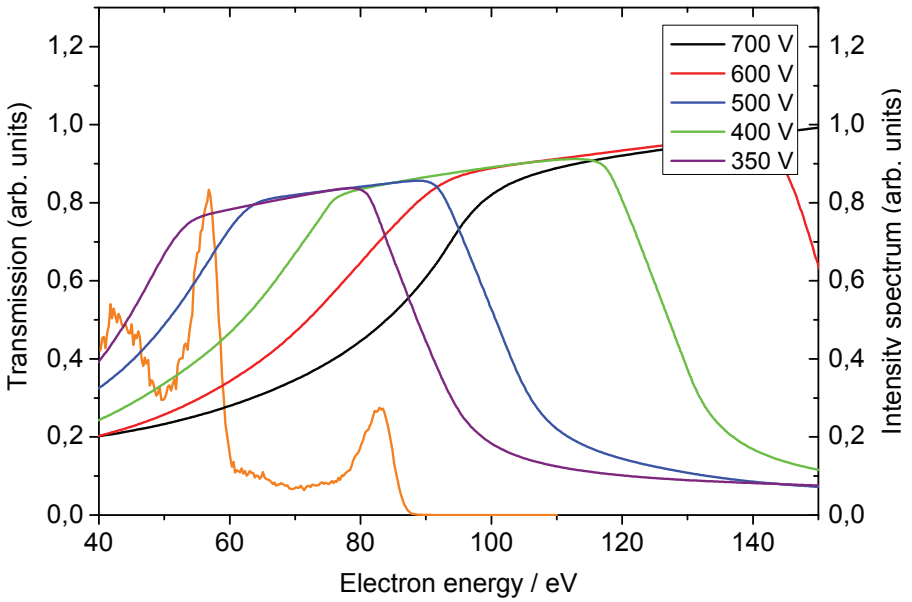

Figure 4.6.: Measured transmission function of the electron current (after cubic spline interpolation) plotted against the electron energy for the Kaesdorf TOF at different lens voltages $400 - 700\ V$. All curves have been divided by the same value in order to coincide at the identical kinetic energies. The intensity distribution of a XUV-only spectrum (orange) on W(110) taken at 92 eV excitation energy is shown for comparison.

varies strongly with the lens voltage and the electron's kinetic energy. Moreover, it is difficult to find a lens voltage, at which the transmission of two peaks separated by e.g. 30 eV is equal for each peak. Mostly, one peak will be outside of the plateau of maximal transmission for a given lens voltage, where the transmission is showing a noticeable variation already within the peak. An example for this behavior is given in Fig. 4.7. Here, the noble gas neon has been observed independently by two groups. The measurement on the left side has been acquired with the Kaesdorf-TOF under excitation of our pulsed (attosecond) XUV-source at an excitation energy of 106 eV, while the right spectrum has been taken with a $YM\zeta$ x-ray tube (excitation energy 132.3 eV, natural linewidth 0.47 eV) and an hemispherical analyzer (HEA) with nearly constant-transmission. It is clearly observable that the Ne 2s and 2p peaks exhibit different intensity-ratios for the Kaesdorf TOF and the HEA measurement. This strong modification, even switching the sign of the intensity ratio, is not a physical effect, but an effect of the different transmission functions of the two spectrometers. Recent simulations [31] showed that this behavior, in the case of attosecond spectroscopy, can lead to an asymmetry in the recorded spectrograms and thus, an artificial delay. Therefore, the energy dependent transmission of the lens had to be corrected for each spectrogram according to the measured transmis-

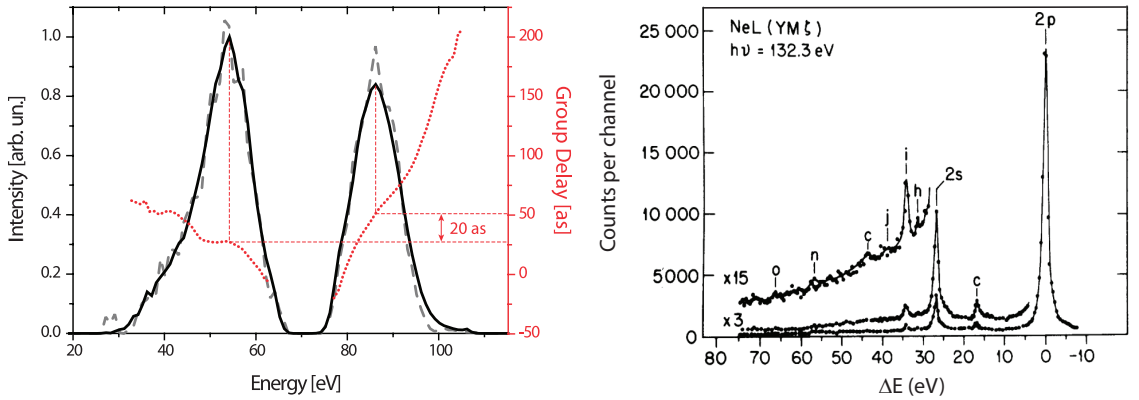

Figure 4.7.: Comparison of the intensity distributions measured by [14] and [101] for the $2s$ and $2p$ shell of neon. The spectrum on the left side has been measured with a TOF and shows a modification of the intensity relation in comparison to measurements with a HEA, where the transmission as a function of kinetic energy is well known.

sion curve on Si(111). Regarding the new spectrometer, it was desirable to have a nearly constant energy dependent transmission to omit this step, since the accuracy of all TOF-measurements otherwise strongly depends on the accuracy of the Si(111)-measurements.
The second problem lies within the dead time of the pulse discrimination/counting process. The dead time of 3 ns in the current single anode setup prevents the detection of any electrons within this time-frame after detection of the first electron. Fig. 4.8 shows the influence of the dead time effect on the spectra with one spectrum obtained with low XUV intensity (black) and one at higher intensity (red). The black (raw data) curve is depicting the expected behavior, where the low (kinetic) energy tail of the peak is modified by an increasing amount of electrons, inelastic scattered to lower kinetic energies. However, for increased XUV intensity, the dead time effect prevents detection of a significant part of events in a "shadow window" behind earlier events. In this way, the tail of the main peak is reshaped resulting in the creation of an artificial peak at lower energies in some situations. Consequently, for excitation energies lower than 100 eV and depending on the laser performance, one may have to limit the XUV intensity with the present spectrometer. The effective dead time can be decreased by the use of segmented anodes, where electrons arriving at different segments still can be detected.
In this spirit, a new TOF-spectrometer was devised, which solves the aforementioned problems and at the same time offers a larger and variable acceptance angle as well as a moderate angular resolution. The new lens design, which supports these properties, has been found through extensive electron trajectory calculations of angular dispersed electron beams in the relevant energy range between 40 and 150 eV.

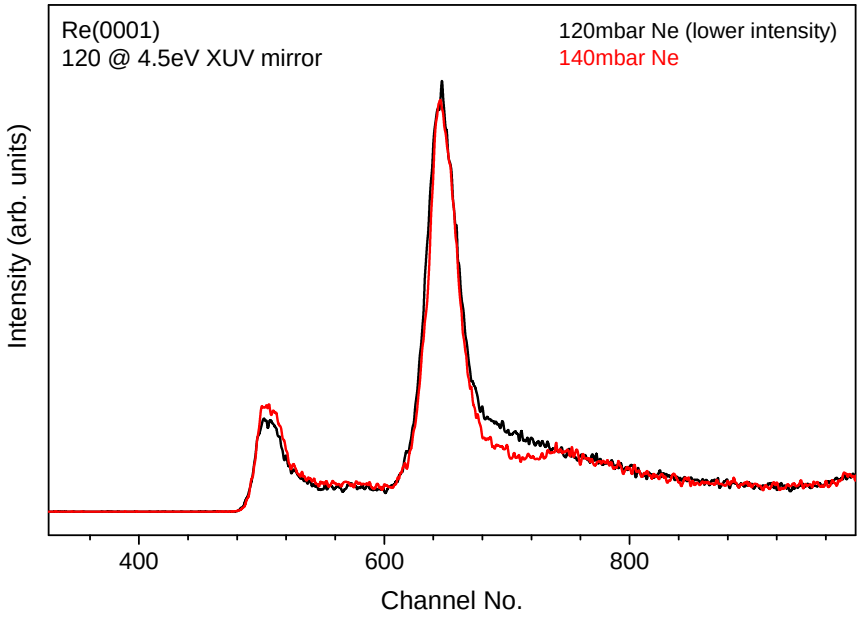

Figure 4.8.: Measurement of the Re CB and 4f states for low (back curve) and high XUV intensity (red curve). For large intensities, the effective deadtime of the discriminator shows up, leading to a dip for a certain period of time after the most intense peak. Provided by [31].

4.2. The large angle, anode segmented TOF-spectrometer

4.2.1. SIMION trajectory simulations

The trajectory simulations have been performed with the SIMION 8.0 (Scientific Instrument Services) ion optics simulation program, which is also able to solve electron propagation problems. The program enables the definition of electrodes and their associated potentials in 3D-space and is subsequently calculating the electric potential for the remaining points in space by a solution of the Laplace-equation. Electrons, propagating in the field of such an electrode system, experience a force in direction of the potential gradient. The incident electron beam can be focused this way.
The first draft of the new TOF-spectrometer was based on the idea to create a lens-free system, where segmented anode plates were placed rather close to the sample to still provide a large acceptance angle. This would have the advantage that electron trajectories can be calculated directly from the analytical equations. However, it

was quickly realized that such an arrangement also involves a large spatial error as can be seen from equation 4.4. Therefore, a system including an electrostatic lens and a long drift tube (705.5 mm) was chosen instead. The use of an inverting lens has been found to give the best results in our case. Here, the electron trajectories are driven through an inversion point. Incident positive-angle electrons arrive at the anode with a negative angle, as can be seen in Fig. 4.9. The figure shows calculated electron trajectories for different incidence angles varying in steps of 5° for the two extreme cases of 40 eV (black lines) and 150 eV (red lines) kinetic energy, all starting from the same point 3 mm in front of the entry cone, which was chosen as the TOF working distance. The 12 mm aperture of the cone allows a large acceptance angle. The outside of the cone is at ground. Simulations showed that its inside, extending to the entrance aperture, should be at a potential different from ground in order to focus the divergent beam emerging from the sample already at this entry location. This can be achieved by covering the internal of the cone with a thin enamel layer onto which a gold layer is evaporated. In the following, a high voltage lens is focusing the electron beam even further, while at last another high voltage electrode followed by 3 lower voltage electrodes (around 1 kV) spatially spreads the beam onto the spectrometer anode.
With this method each incidence angle is mapped onto a different anode spot. This mapping works best for an electron energy of 150 eV and is slowly decreasing in performance with lower energies down to the limit of 40 eV, exhibiting the lowest spatial spread. For an electron energy of 40 eV, the angle-to-position mapping is still clearly defined. Such a well-defined distribution is important for the increase of the temporal resolution by the use of a segmented anode. Different emission angles imply different trajectories, i.e. different flight times even for identical kinetic energies, but also different impact sites at the detector. Since each angle-dependent electron trajectory is receiving a different spatio-temporal mapping, a spatial limitation of the anode is inherently increasing the temporal and therefore the energy resolution. According to the simulations, the spectrometer allows a large acceptance angle of ±50° in the energy range between 40 eV and 150 eV. If the distance to the sample is decreased to about 2 mm, even an accepted angle of incidence of ±55° is possible.

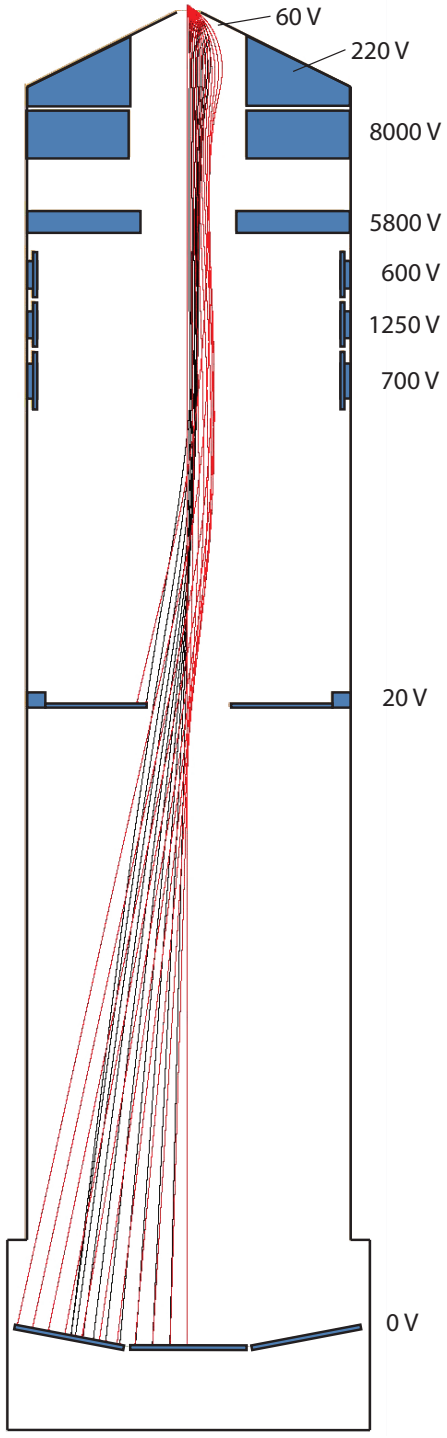

Figure 4.9.: SIMION simulations of the lens design of the new TOF spectrometer. The lens electrodes are shown in blue. Simulations have been performed for electrons at 150 eV (red curves) and 40 eV (black curves) kinetic energy, each for a set of different angles. The angular distribution reaches from 0° to 55°.

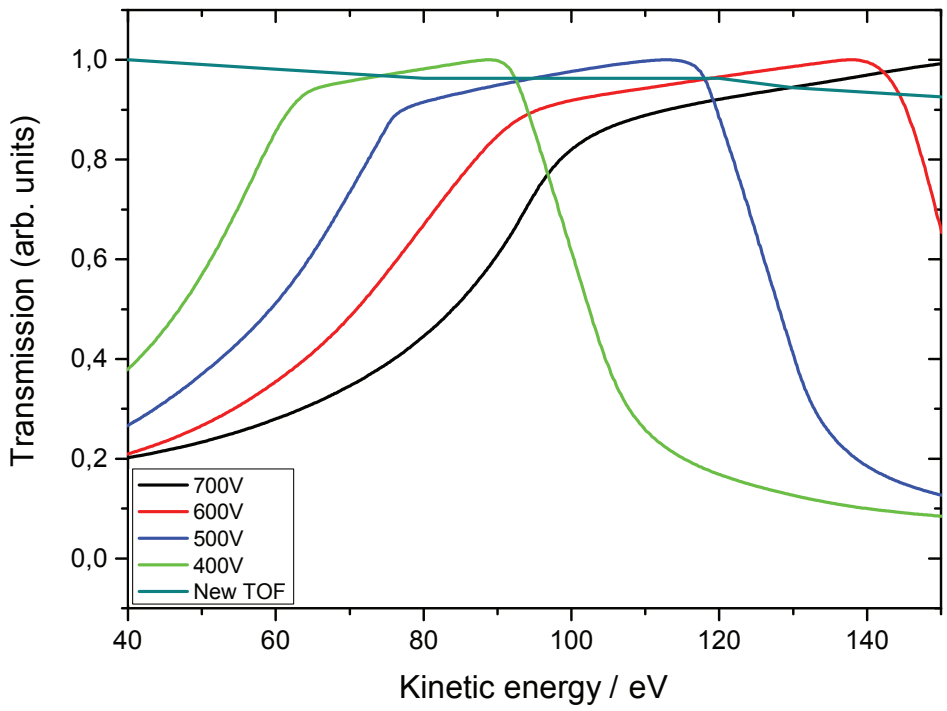

Figure 4.10.: Relative change of the transmission plotted against the electron energy for the Kaesdorf TOF at different lens voltages $400 - 700\ V$, and the new TOF spectrometer at its operating voltage. Each curve has been normalized against its maximum.

Fig. 4.9 shows a planar cut through the spectrometer, while in fact the calculated electrodes have a cylindrical form with an open center aperture. The spectrometer's field-free propagation space is defined by a final electrode at almost zero voltage ($20\ V$) in a distance of $365\ mm$ from the spectrometer entry. This last aperture is simultaneously limiting the maximal angular acceptance, especially for electrons of lower energy. Thereby, the angle-integrated intensity for each kinetic energy is approximately the same, which translates into an almost constant energy dependent transmission. The calculated energy dependent transmission in comparison to the transmission of the Kaesdorf spectrometer is shown in Fig. 4.10. It can be seen that the new spectrometer shows an almost energy independent behavior in the relevant energy range as a result of the good spatial mapping of the lens and the implementation of the zero-potential aperture plate. Hence, the energy dependent transmission of the electrostatic lens can be neglected for this new design, rendering the use of transmission corrections unnecessary.
Moreover, segmented anodes have been envisaged to counter saturation effects as a result of the detection electronics' dead time. Therefore, three anode plates have been placed in the setup, while the outer plates have been tilted by 11° to decrease

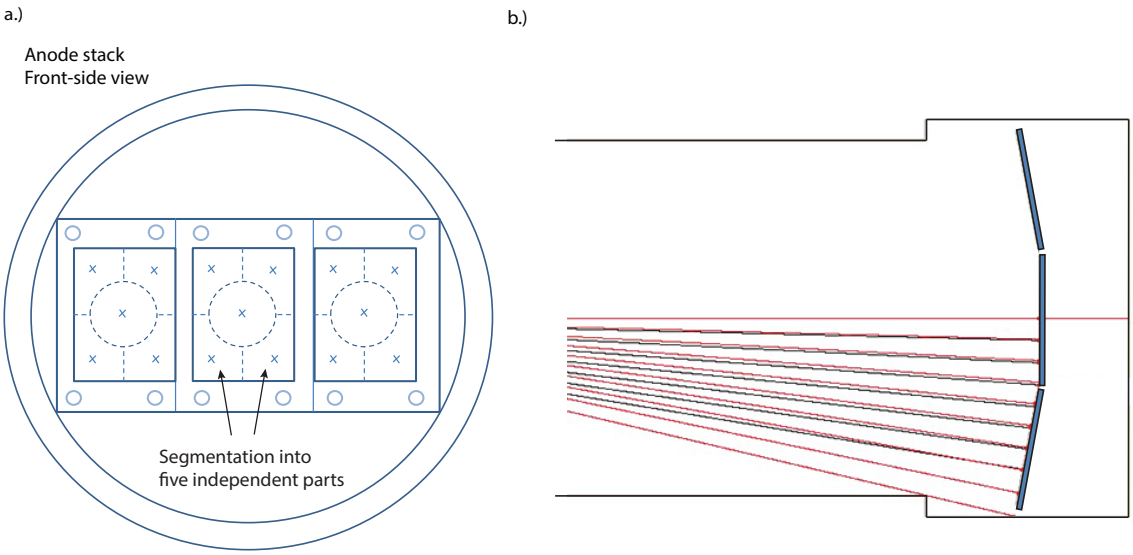

Figure 4.11.: a.) Top view on the anode stack. The segmentation of each anode into 5 independent parts is shown. b.) SIMION simulation for electrodes voltages optimized to retain an optimal angular resolution. The figure shows electron trajectories with 150 eV kinetic energy (red curves) and and 40 eV (black curves) increasing the angle in 2° steps.

the spatial error for these anodes. Each anode plate itself is further divided into 5 individual anode segments, each connected to its own detection electronics. This allows an independent detection of the, in total, 15 segments and makes multiple electron detection possible, if different segments are hit. The effective dead time this way decreases to a value of 0.2 ns for an isotropic angular electron distribution. The true effective dead time, of course, strongly depends on the actual angular distribution, which can be different for each excited state.
The introduction of a segmentation also provides a moderate angular resolution, which, on the one hand, would be very useful to observe the modification of the laser streaking in dependence of the angle as is expected from equation 2.27. Since this variation follows a cosine distribution, already a rough angular resolution is sufficient in this case. On the other hand, an angular resolution would be very useful to enable a better comparability of the measured spectra with those given by, e.g., theoretical band structure calculations, where a full, k-vector dependent calculation is difficult as yet. The angular resolution of the spectrometer in the normal mode with electrode potentials according to Fig. 4.9 is $\approx 10°$. This resolution can be modified by the applied lens voltages: One prominent feature of the new spectrometer is that the accepted angle of incidence can be continuously varied by a variation of the high voltage lens potential. In the most extreme case, the maximal acceptance angle can be reduced to $\approx 16°$ for 150 eV electrons, which gives an angular resolution of 2.5°

for this energy (Fig. 4.11 b). In this way, also angle resolved measurements can be conducted, provided that the intensity of the excitation source is large enough. For attosecond spectroscopy with its low intensity XUV-excitation pulses, this is currently only reasonable at an photon energy around 90 eV.

4.2.2. Energy resolution of the spectrometer

The anode segmentation has been chosen in such a way as to minimize the total uncertainty of the detected energy. Thus, a segmentation as depicted in Fig. 4.11 a.) has been chosen, which builds on a radial center segment surrounded by 4 complementing segments to achieve a rectangular shape (as restricted by the form of our MCP's). This arrangement gives the lowest spatial error (i.e. the energy uncertainty arising from the spatial uncertainty of the trajectories; see equ. 4.4), since the spatial uncertainty is naturally increasing from the center of the anode plate to one of its corners with electron trajectories of nearly the same spatial error at the same radius around the center. Division at the halfway of this increasing radial uncertainty allows to minimize the maximal uncertainty of each segment.
As has been mentioned before, the application of a complex electrostatic lens usually prevents the analytical calculation of the energetic uncertainty. Therefore, one has to resort to numeric trajectory calculations provided by SIMION. For the SIMION data analysis, a routine has been written in Labview (National instruments), which is able to directly calculate the energy uncertainty from the given data. In principle, one determines, which electrons hit a selected segment in a predefined time interval Δt, defined by the resolution of the CDF/TDC-discrimination (i.e. 100 ps). The electrons, still arriving within this time frame around a chosen center time t_c, cannot be separated from each other so that their range of kinetic energies defines the energetic uncertainty.
The corresponding procedure is, in detail, pursuing the following steps: At first, a simulation is conducted in SIMION in a given energy range (i.e. 10 eV or larger) around a chosen center energy, where the energy is varied in small steps of 0.1 eV. At each energy step a discrete number of electrons (i.e. 180) are launched from the intended sample position, where the angle of incidence with respect to the spectrometer axis is varied in both directions, simultaneously in 0.1° steps (or smaller in dependence of the number of electrons). Therefore, for each energy, the angular electron distribution from the center to the corner of the anode is measured. SIMION writes the electron time of flight and the x,y,z - coordinates of each electron hit at the anode in a separate file, which can then be analyzed by the Labview routine. At first, the z-coordinates are used to exclude electrons from the analysis, which are not at the position of the anode detector. The x and y-coordinates are then recalculated to a radius r. In the next step, any electron is excluded from the further analysis,

which is not in the predefined time frame around the variable time t_c and not in a radial frame between two predefined values r_{min} and r_{max}. The latter is denoting the spatial dimension of the chosen segment, while at the same time defining the currently observed segment. Since so far, only a line distribution of the electrons diverging from the anode center is simulated, the radius r of each remaining electron is converted to the corresponding circumference U in consideration of the form of the examined segment. This way, a measure for the actual intensity for the case of a uniform electron distribution is obtained. For the inner radial segment, this conversion is rather simple as given by the formula

$$U = 2\pi \cdot r \tag{4.7}$$

For the outer segment, the conversion has to be divided into two parts, for radii smaller or larger than half of the size of the anode (25 mm), giving

$$U_{in} = \frac{1}{2}\,\pi \cdot r \tag{4.8}$$

or

$$U_{out} = \pi r \cdot \left(0.5 - \frac{acos(\frac{25}{r})}{90^{\circ}}\right)\ , \tag{4.9}$$

respectively. In the last case, the rectangular form of the anode comes into play, where the excess intensity on each side had to be subtracted according to

$$U_r = \pi r\ \frac{acos(\frac{25}{r})}{180^{\circ}}\ . \tag{4.10}$$

The remaining values of the analysis are now already depicting the energy range (as calculated from the arrival time) of all electrons arriving within the defined temporal and spatial frame. In order to receive a realistic value of the energetic uncertainty, though, the calculated electron energies have to be weighted according to their appearance frequency on the segment. A measure for this value is the circumference U, which was calculated for each energy. The routine is now summing up all circumference values U of the same energy value. The summed up U-values plotted against the kinetic energy then resemble a Gaussian shape, from which the FWHM can be determined. The FWHM then provides the sought energy resolution. With this method an average energetic uncertainty between $0.6 - 0.7\ eV$ for each segment at an energy of 150 eV was determined, which becomes less for lower kinetic energies.

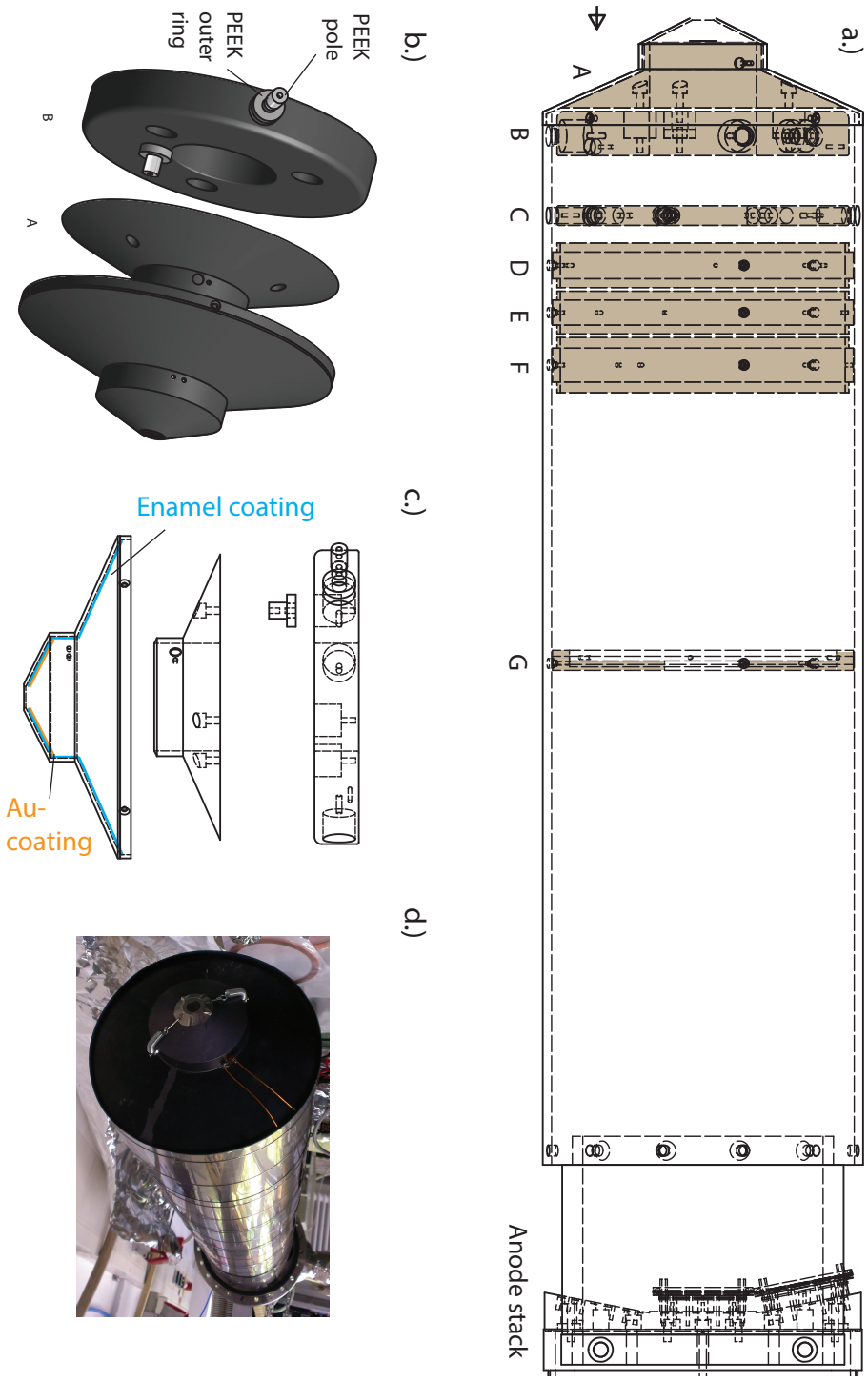

Figure 4.12.: Right side: Inside view of the TOF spectrometer showing the arrangement of electrodes marked in brown. Left side: Illustration of the mounting of the first two electrodes and placement in the entry cone. The coating of the inner side of the cone with enamel and its front part with gold is also illustrated.

4.2.3. Setup of the large angle, segmented TOF

The new TOF spectrometer has been realized with the electrode/detector positions and forms resembling their simulated SIMION counterparts as close as possible. An inside view of the final setup is given in Fig. 4.12. At the entry of the TOF cone, a fine graphite-coated grid (8 lines/mm, 85% transmission) is installed defining the zero-potential and a clear onset of the TOF electrode potential influence. The grid is drawn over the 12 mm diameter entry of the TOF cone and is mounted through a metal sheet, which is connected to two springs anchored at the sides of the cone (Fig. 4.12 c). The outer form of the cone has been modified to resemble the form of the sample mount as present in the AS3 chamber, while leaving the electrode potentials inside the spectrometer untouched. This way, the spectrometer can be placed in close distance to the sample permitting a minimal working distance of 2 mm. The inside of the cone is covered with enamel coating of 100 μm thickness (Wendel Email GmbH), which provides a good electric isolation for the low potentials (below 300 V) applied at the front of the spectrometer. The inner front part of the cone is additionally coated with a thin gold layer on top of the enamel (Fig. 4.12 b). With this method, it is possible to extend the first electrode, i.e. the gold layer, right to the front of the cone. A thin graphite stripe connects the gold layer with an isolated screw, which is contacted outside the cone.
The cone expands to the front of a 180×5 mm aluminum tube, the size of which fits inside a 200 mm CF-flange and gives preferential potentials of the implemented ring electrodes within the SIMION simulations. The tube is housing the electrostatic lens system, which consists of cylindrical electrodes of various sizes with an open center aperture between 52 mm (electrodes A and B) and 60 mm (electrode C). Care has been taken to prevent any breakthroughs of the high voltage. Therefore, the distance of the high voltage electrodes (B and C), which exhibit a potential of 8000 V and 5800 V, to the inner surface of the mounting tube is ≥ 3 mm. The mounting of electrode B is described in Fig. 4.13. For electrode C, a very similar mounting technique has been chosen, where, yet, the outer PEEK ring has been omitted and the drilled electrode holes have a diameter of 9 mm (cf. Fig. 4.13). This is reasonable, since the potential of this electrode is lower. The 0.13 mm thick Kapton, used for isolation of the electrode contacting wires, has been tested before [102] and was found to resist voltages larger than 10 kV. In addition to the Kapton-isolation of the wire, this is sufficient to isolate the high voltage from the tube, which is inherently at zero-potential, i.e. connected to ground.
Electrode A fits directly into the inner form of the cone and reaches up to the front to a distance of 13 mm to the conic aperture (Fig. 4.12 a,b). It is mounted in a distance of 3 mm against the subsequent electrode (B) in the same manner as before providing a reasonable high voltage isolation. Therefore, the electrode is screwed against three 9 mm-PEEK poles, which are residing in 18 mm holes in the front of electrode B surrounded by PEEK rings (Fig. 4.13). Electrode A is contacted

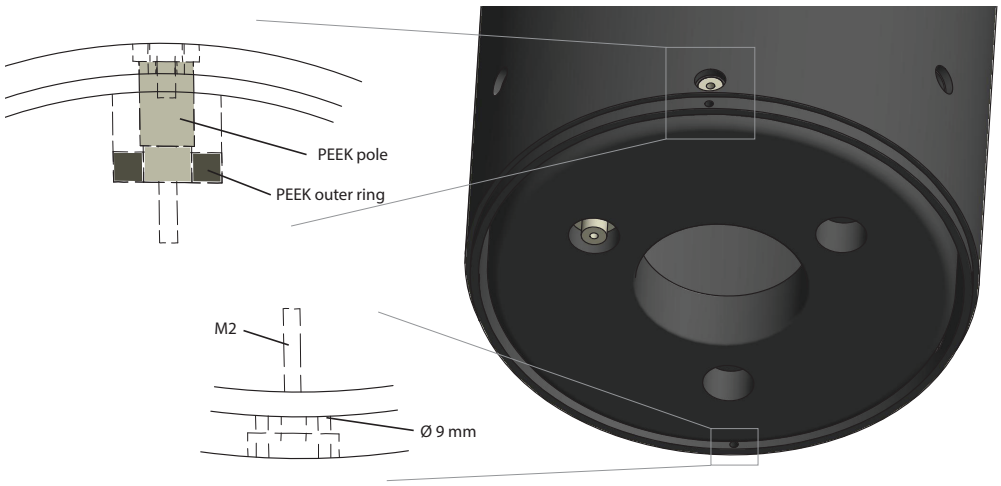

Figure 4.13.: Mounting of the high voltage electrode B. Three 18 mm diameter holes are drilled into the sides of B for every 120°, in which 9 mm PEEK poles are mounted with M3 screws. Each pole is additionally centered by a PEEK outer ring, filling the remaining space of the hole. The spectrometer tube features three corresponding 9 mm holes, which are precisely fit to the PEEK poles to obtain a good central positioning of the TOF electrodes. Each pole is then screwed against a thin 11 mm-diameter aluminum plate, sitting in an equally-sized notch of the mounting tube around the center of the hole. The electrodes are contacted from outside of the tube by long M2 screws (bottom of the figure), which pass through additional 9 mm holes in the tube. The space between the screw and the rim of the hole prohibits creepage currents along the Kapton sheets surrounding the screw. More precisely, the screws are contacted outside of the tube by thin, 0.9 mm thick, Kapton-isolated wires, additionally wrapped between two sheets of 0.13 mm-Kapton. The wires lead to 20 kV -high voltage feedthroughs, mounted in the 200 mm end flange. The right draft shows three holes drilled in the front of electrode B, enabling to mount electrode A.

by a M2 screw guided through the side of the cone and isolated against the cone by a small ceramic hull. The other electrodes (D,E,F) are 2 mm thick rings with a distance of 0.5 mm to the inner wall. Three screws (M2) in ceramic hulls are fixing the electrodes in position and are also contacting them from outside in order to apply a voltage in the 1 kV range. The final electrode (G) is depicting an almost zero-potential electrode (20 V) with an open center aperture of 43 mm and is mounted in the same way.
The 180 mm tube is hold in place by two semicircular plates, which leave an open rectangular space of 86 mm between them and, themselves, are mounted sideways

against a rectangular base plate (Fig. 4.18). On top of the base plate, the anode stack is mounted on a removable, 10 mm thick stainless steel plate, where the outer wings of the plate are tilted in order to realize the 11° setting angle of the outer anodes. The setting of one anode stack is described in Fig. 4.14, where the basic anode setup is similar to a previously realized setup [102] and has been improved and adapted to our needs. A fine, graphite coated Cu/Ni grid with 8 lines/mm and a transmission of 85% is placed in the grid holder at the top of the stack. The Cu/Ni grid material has been chosen due to its ability to shrink irreversibly upon heating to about 300°, which removes any asperity of the grid. Yet, the grids provide a good surface smoothness already without heating, which has been omitted therefore.
The employed MCPs, two at each anode plate, exhibit a pore size of 0.5 μm with overall spatial dimensions of $50 \times 50 \times 0.5$ mm and are mounted in chevron configuration. In order to contact both sides of the MCPs, a set of Kapton sheets was manufactured from copper coated Kapton material (I.V. Schaltungen GmbH). The Kapton sheets are described further in Fig. 4.15. One of the copper coated Kapton sheets is placed at each side of the MCPs, enabling the application of a voltage difference of 700 V between both sides of one MCP. The acceleration voltage between the MCPs was set to 300 V, where the efficiency of secondary electron generation in the second MCP is maximal and saturation of individual channels occurs. The bottom of the MCP at the exit of the stack is directly connected to the high voltage potential at the titanium plate, which is contacted by bronze-clamps. The plate is isolated from the underlying copper blocks by another copper coated Kapton sheet, fitted in its coating to the form of the blocks (Fig. 4.15). The double-sided coating of the Kapton sheet acts as a capacitor between the high voltage side at the titanium plate and the copper blocks, which are directly connected to ground through the anode stack holder plate. In this arrangement, the capacitor is short-circuiting any unwanted high-frequency components at the backside of the MCP, which can couple into the measured signal by the capacitor C_A, as is illustrated in Fig. 4.17 b.). The different potential areas at the backside of the MCP and the front of the anode plate are inherently representing a capacitor C_A, so that any high frequency fluctuations have to be discharged at this point.
The setup of the copper blocks and the glass anode is shown in Fig. 4.16. Several anode materials have been tested, however, the best results could be achieved with simple sheet glass. Materials like PEEK have been found to bend during bakeout at 200° in vacuum, most probably due to a present inner strain, while plates of Marcor tend to break rather easily at these dimensions. A high resistance layer on top and a segmented gold layer on the bottom of the glass plate efficiently separate the electronic currents according to their point of impact and thereby, realize the division of the anode in individual segments as intended. The gold layer has been realized by pulsed laser desorption on a previously evaporated Cu/Ni-layer to increase the adhesive strength. The present design is also serving another purpose: Both sides of the glass plate are coated with a conductive material, while the car-

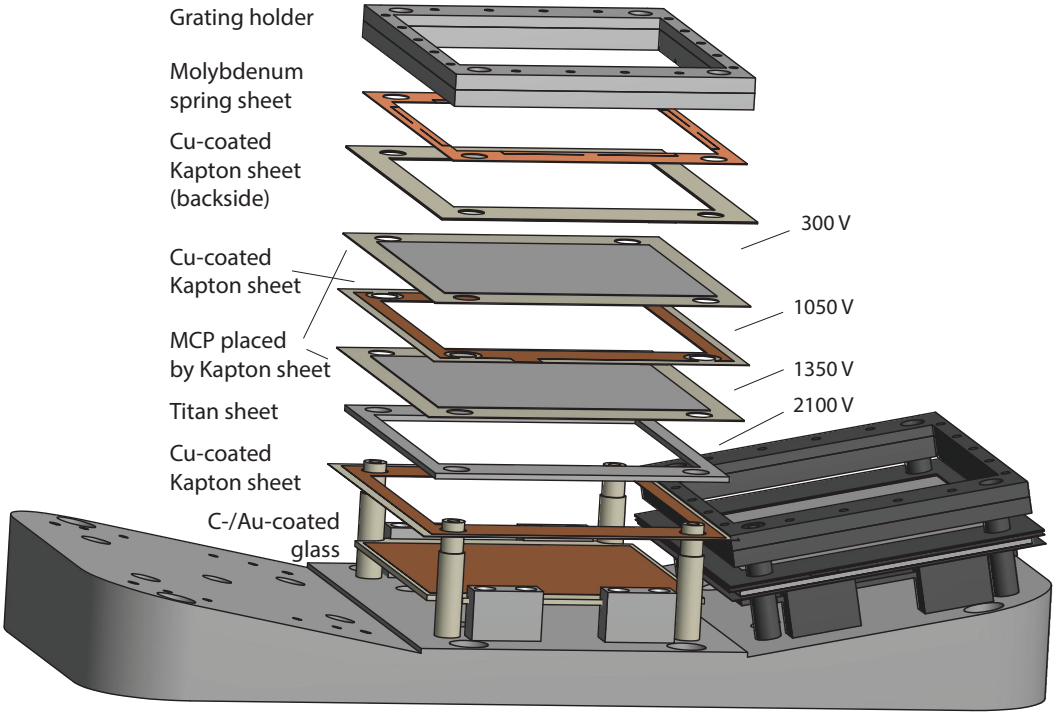

Figure 4.14.: The anode stack is hold in position by four M2 thread bars, which are fitted through corresponding holes in each stack component and placed in a distance of 44 mm and 58 mm, respectively. Each thread bar is surrounded by a PEEK hull to achieve electrical insulation. The hulls exhibit an external diameter of 4.6 mm, reduced to 4 mm at its top to define the final position of the grid holder. The latter consists of two 3 mm thick rectangular plates with a 48×48 mm rectangular hole as predefined by the detection area of the MCP's. Such a rectangular hole is therefore present for each component. A fine grid between the holder plates is mounted by 18 M1.4-screws equally distributed along the sides of the plates. A nut at each thread bar is pushing the grid holder down to the notch edge of the PEEK hull. The whole stack is smoothly pressed together by small molybdenum springs. These are realized through a 0.15 mm rectangular molybdenum plate, from which four 1.4 mm and four 2.5 mm stripes have been cut out by a laser (Riemensperger mechanische Werkstätte GmbH) and bend downwards. With this method, a smooth and equal compression is achieved for the whole anode stack. The MCP's are hold in place by thin Kapton sheets surrounding them. The last MCP lies directly on a 1 mm-thick titanium plate, providing a straight and smooth plane. The plate itself resides on four 12.7×5.2 mm copper blocks.

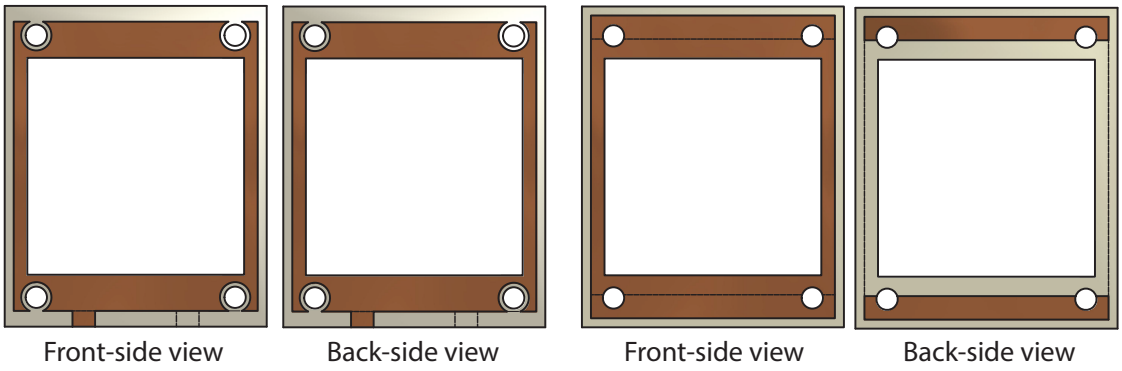

Figure 4.15.: Drawings of the fabricated Cu-coated Kapton sheets. The Cu is limited to the brown marked areas. The copper has been etched to a predefined form, which experiences a minimal distance to the border of 2 mm and of 1 mm around the holes to minimize the risk of an electric breakdown or leakage current. In the actual form, 5 mm wide copper stripes at different positions at the front and the back side of the Kapton sheet are drawn to the side of the sheet, which enable to individually contact the copper coatings. Contacting is made with bronze-clamps, which then lead to thin coax cables with Kapton insulation. Left side: Front and backside of the Kapton sheet used for contacting the MCP's. Right side: Kapton sheet used for isolation of the Titan sheet from the grounded copper blocks.

bon layer represents a branch with a high resistance. This construction denotes a high-pass filter. The AC signal is taken from the gold layers and the DC current flows to the carbon layer at high voltage (Fig. 4.17 b). This method ensures that the rapidly changing signal (with a duration below 1 ns), emitted from the MCPs upon electron impact, can be efficiently separated from the high voltage current at the high resistance layer. The carbon layer is contacted with slightly bend spring steel coated with a layer of gold, which is sitting in a notch of one copper block and partly residing in a Teflon tube to isolate it from the block.
The contact of the gold layers is made by molybdenum springs coated with a thin layer of gold by sputter deposition (Thomas Rapp, E10). The spring is created by folding a thin 3 mm stripe of molybdenum into an U-form and spot-welding it centered against a screw joint (Fig. 4.19 a). The screw joint then allows to fix the spring arrangement directly to the feedthroughs, which are welded into the stack holder plate and lead the signal outside of the vacuum. One spring/feedthrough arrangement is present for each segment, where the position of the springs has been chosen in such a way that the positioning is preferably central within the segment. The glass plate, which is fixed in between the notch created by the two parts of the copper block, is pressed downwards when the copper block is fixed against the stack

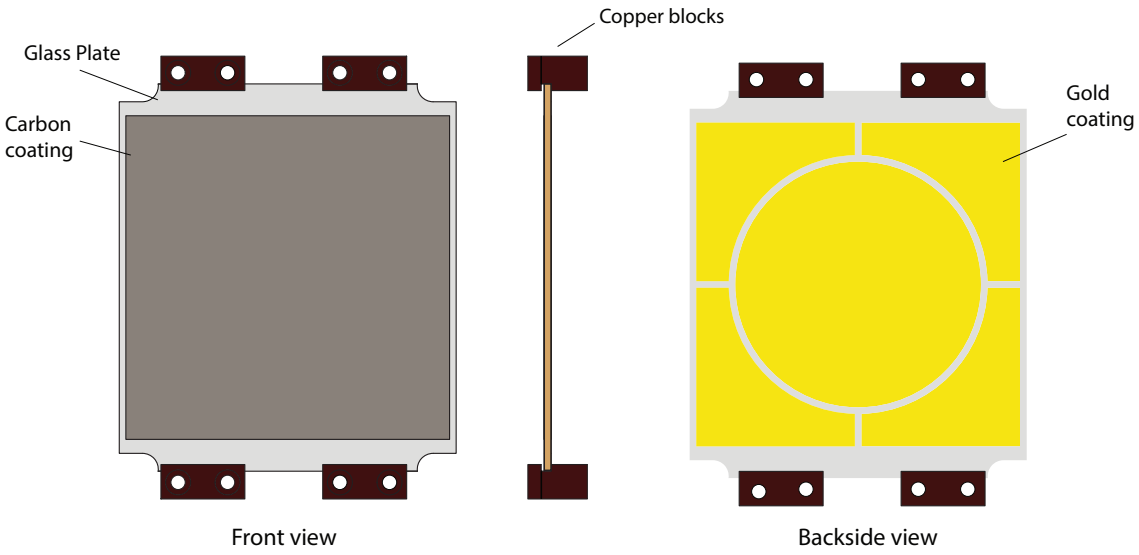

Figure 4.16.: The copper blocks are built from two parts, which are fixed together and also against the anode stack holder by each two M2 screws (Fig. 4.16). Combined they exhibit a 1.2 mm notch, in which the final component, a 1.1 mm thick anode plate, is placed. The thin glass plate has been cut at its corners allowing it to fit within the thread bars, which at the same time fixes the central position of the plate. The anode glass has been coated on both sides. The coating in direction of the MCPs is made by a single 49×49 mm, high resistance carbon coating (≈ 10 $M\Omega$), while the other side exhibits a gold coating in the intended form of the anode segmentation (both realized by Dominik Seiler, Technische Universität München E12).

holder plate. Thus, the glass plate is pressed against the springs leaving a spring stroke of 1 mm.
The mounting of the spectrometer tube and the anode stack plate is illustrated in Fig. 4.18. The single large hole, visible in the base plate, was implemented to permit a large flexibility for future possible changes of the anode stack layout. As one possibility for future implementations, one could think of the use of a sapphire plate as a vacuum seal, placed directly onto the Viton rings. When coated on both sides, the sapphire plate also represents a capacitor that can decouple the signal from vacuum without the use of feedthroughs. In this way, an in principle arbitrary segmentation of the anodes can be achieved.

During the whole construction, care has been taken to avoid any influences that could lead to a deviation from the calculated trajectories. Therefore, the total inner part of the spectrometer is coated with a layer of graphite, which was applied with

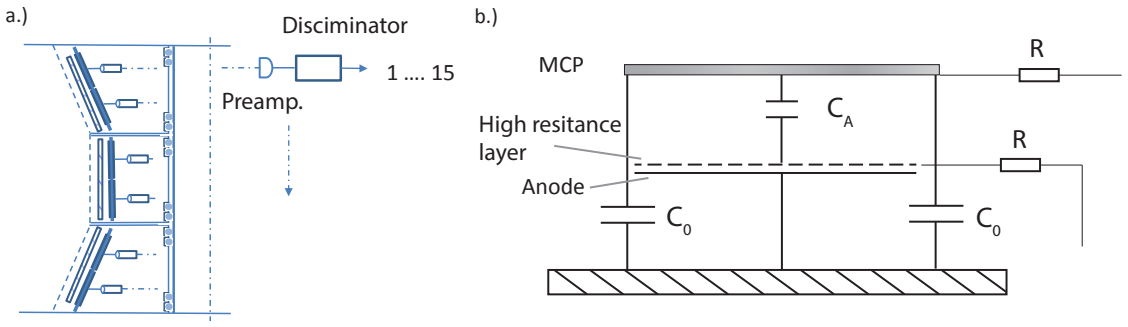

Figure 4.17.: a.) Illustration of the decoupling of the electronic signals. The signal of each anode segment is directly taken from the backside of the anode and passed through a preamplifier and discriminator, giving 15 independent signals. b.) Circuit of the MCP-/Anode- setup.

a spray gun. Any unwanted potential difference created by differing work functions is thereby prevented. At the same time, outer magnetic fields including the earth magnetic field must be shielded from the inside of the spectrometer. For this reason, the outside of the 180 mm-tube is covered with several layers of Mu-metal (a nickel-iron alloy), exhibiting a high magnetic permeability. The magnetic shielding needs to be extended beyond the anode stack to guarantee magnetic fields from penetrating this area. Therefore, the rectangular base plate cannot be sitting directly on the final flange, but is connected to it by a 165×58.6 mm and 194 mm long rectangular tube (Fig. 4.18). The dimensions of the tube resemble the inner hole of the base plate so that the inside of the tube is at atmospheric pressure, while its outside is at vacuum. With this displacement, it was possible to draw the Mu-metal to about 15 cm beyond the end of the stack holder plate. The Mu-metal shielding has been finally demagnetized by application of a strong electromagnetic coil driven by an alternating current. The magnetic shielding in the front of the spectrometer is realized by the cone, made of pure iron (ARMCO). As a magnetically soft material it can be used for an efficient magnetic shielding. After manufacturing the conical form, the part has been annealed in vacuum at a temperature of $800°$ C and finally demagnetized by an AC-field. A self-made plastic form, roughly following the shape of the cone, has been wrapped with a copper wire to create this field and efficiently remove any remaining magnetism.

As there has been concerns regarding the operating pressure of the Kaesdorf TOF CF63 pump-port has been installed in the 200 mm end flange, which should allow a good vacuum within the spectrometer. The outer end of the pump port is tilted to allow free access to the nearby feedthroughs. In order to be able to pump the inner part of the spectrometer, large holes have been drilled into the backside of the tube holder connected to the base plate. The conductance of these holes in their sum equals that of the 63 mm pump port, on which a turbo pump is installed.

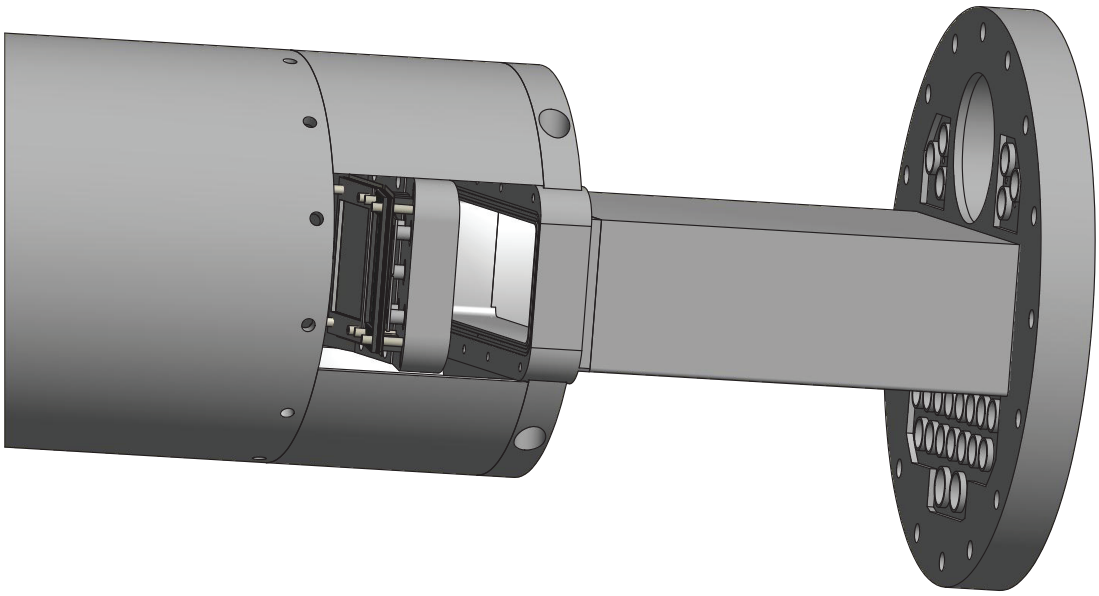

Figure 4.18.: In order to enable the direct contacting of the anode segments by the feedthroughs, the back of the stack holder plate has to be already outside of the vacuum. Therefore, the base plate, against which the stack holder plate is mounted, exhibits a 165×52.4 mm hole, where the ends of the feedthroughs can pass through and at which side atmospheric pressure is present. Since the stack holder plate should be removable, two 1.78 mm-diameter Viton rings are pinched between the plate and the rectangular base plate, fitted into 1.5 mm notches in the base plate. The fitting of the rings into slightly smaller notches has been found advantageous for the sealing against atmosphere. Eight screws, equally distributed along two opposite sites of the plate, now press the stack holder plate against the base plate. If the small free space between the two Viton rings of 1.5 mm is additionally pumped by a roughing pump, this arrangement represents an efficient differential pumping stage. With this setup a pressure in the UHV range can be maintained without problems. The free space is pumped through a thin tube with an inner diameter of 1 mm, which is guided outside the vacuum to the back of the spectrometer.

According to the segmentation of the anodes, in total 15 independent signals are decoupled out of vacuum and need to be discriminated. Therefore, each signal is sent to its own self-made amplifier and a self-made constant fraction discriminator and finally needs to be counted by a TDC. For this purpose a 16 channel multi-event TDC (Caen V1290N) has been bought, which provides an improved temporal resolution of 35 ps (RMS) and is able to analyze the 15 signals independently at the

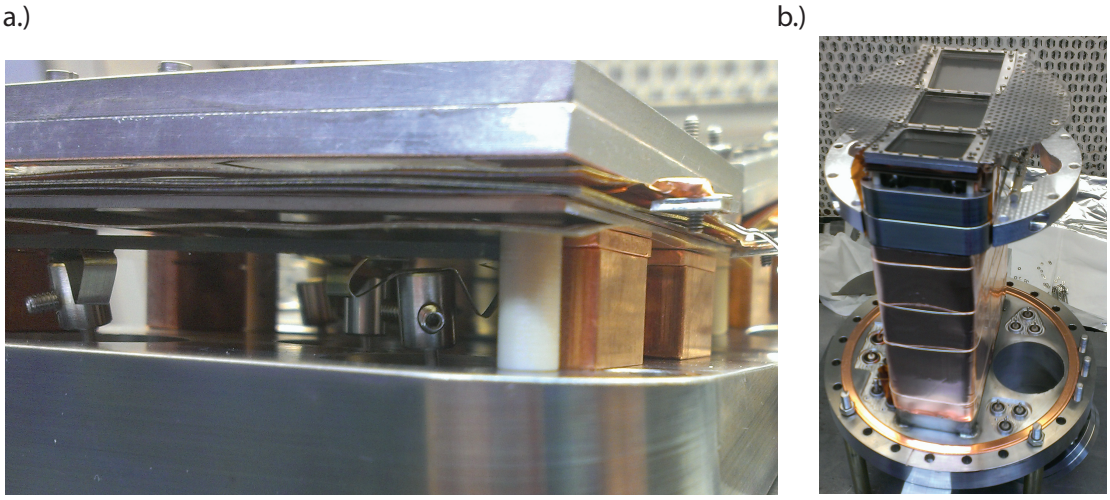

Figure 4.19.: a.) Picture of the spring contacts at the bottom of the anode plate, consisting of a U-shaped, gold-coated molybdenum stripe, spot welded against a screw joint. b.) Picture of the anode stack setup. In order to achieve further shielding, a combination of an 1 mm thick aperture plate with a fine grid (2 lines/mm) on top is placed at the side of each stack.

same time.

4.2.4. Preliminary tests

In order to test the performance of the new TOF spectrometer before installation in the AS3-chamber, a simple electron gun was built that emits electrons of constant energy under an arbitrary angle. With this setup and the spatial resolution provided by the segmented anodes, it was possible to test the spatial mapping of the TOF electrostatic lens as a function of the kinetic energy and angle of the incident electrons. As an electron source, a small tungsten-cathode (AGAR electrode, Plano) was used. Since the generated electronic current of this cathode is not fixed to a defined angle, the cathode was placed in a cylindrical tube, which additionally housed several apertures with small 1 mm diameter central holes. By application of an acceleration voltage between the cathode and the tube/aperture-arrangement, a small diameter, directed beam of electrons with a predefined kinetic energy was extracted. The tube is mounted (and by a Kapton sheet insulated) against a copper plate, which is bent to a U-form as can be seen in Fig. 4.20. The other side of the copper form is mounted against a thick copper plate, which is itself vertically

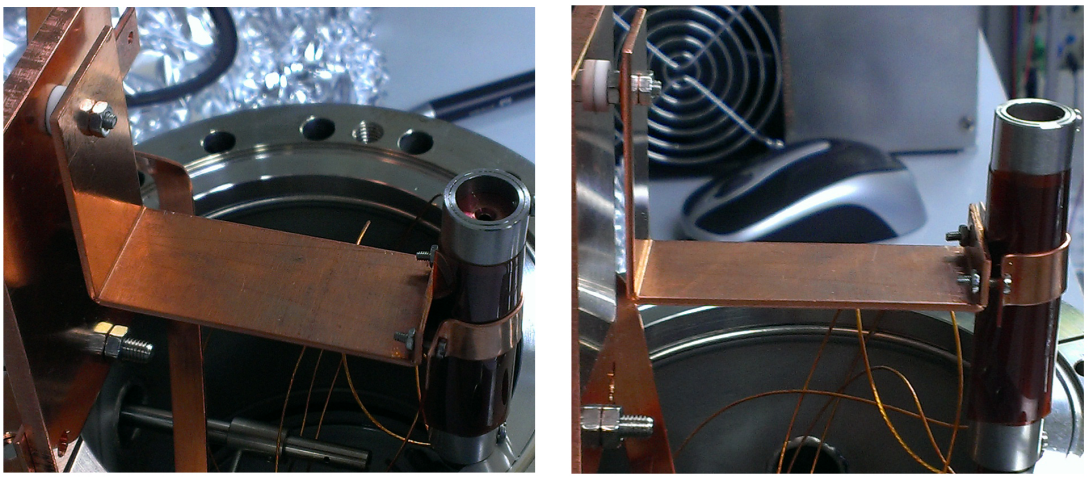

Figure 4.20.: Setup used for measurement of the electron paths within the spectrometer: A tungsten cathode, mounted in the shown tube, emits electrons, which are spatially limited by several apertures. The tube is mounted to a U-form. The form can now be rotated from outside the vacuum to enable measurements for different angles of incidence.

mounted against the inside of a flange. By a rotary feedthrough connected to a rim of the copper form, the incidence angle of electrons emitted from the tube can now be freely varied from outside the vacuum. The construction has been finally conveyed to vacuum with the axis of rotation fixed to a distance of 3 mm to the TOF spectrometer, which simulates the emission of electrons from the sample in the designated working distance of 3 mm to the spectrometer. The tungsten cathode is supporting an emitted electron current of $\approx 1\ mA$, while the current leaving the arrangement of apertures is limited to the μA scale. The kinetic energy of the emitted electrons has now been varied in ranges of $40 - 150\ eV$ and the resulting spatial distribution at the TOF anode segments also under variation of the TOF lens voltages has been observed. Since the electron current can become rather large compared to the common application, the test has not been conducted with the final anode stack, but with simple thin copper plates in the form of the segments, directly soldered to auxiliary feedthroughs. An electronic readout mechanism has been constructed, which samples each segment separately for a predefined time. The modification of the spatial distribution has now been mapped for chosen angles and energies and compared with the SIMION simulations. In this regard, the variation of the maximal acceptance angle of the spectrometer as a function of the high voltage electrode potential has been found useful. Fig. 4.21 is showing the predicted and experimental results for selected values. For all tested energies and angles, a good agreement with the spatial mapping of the simulations could be found, depicting the good performance of the electrostatic lenses.

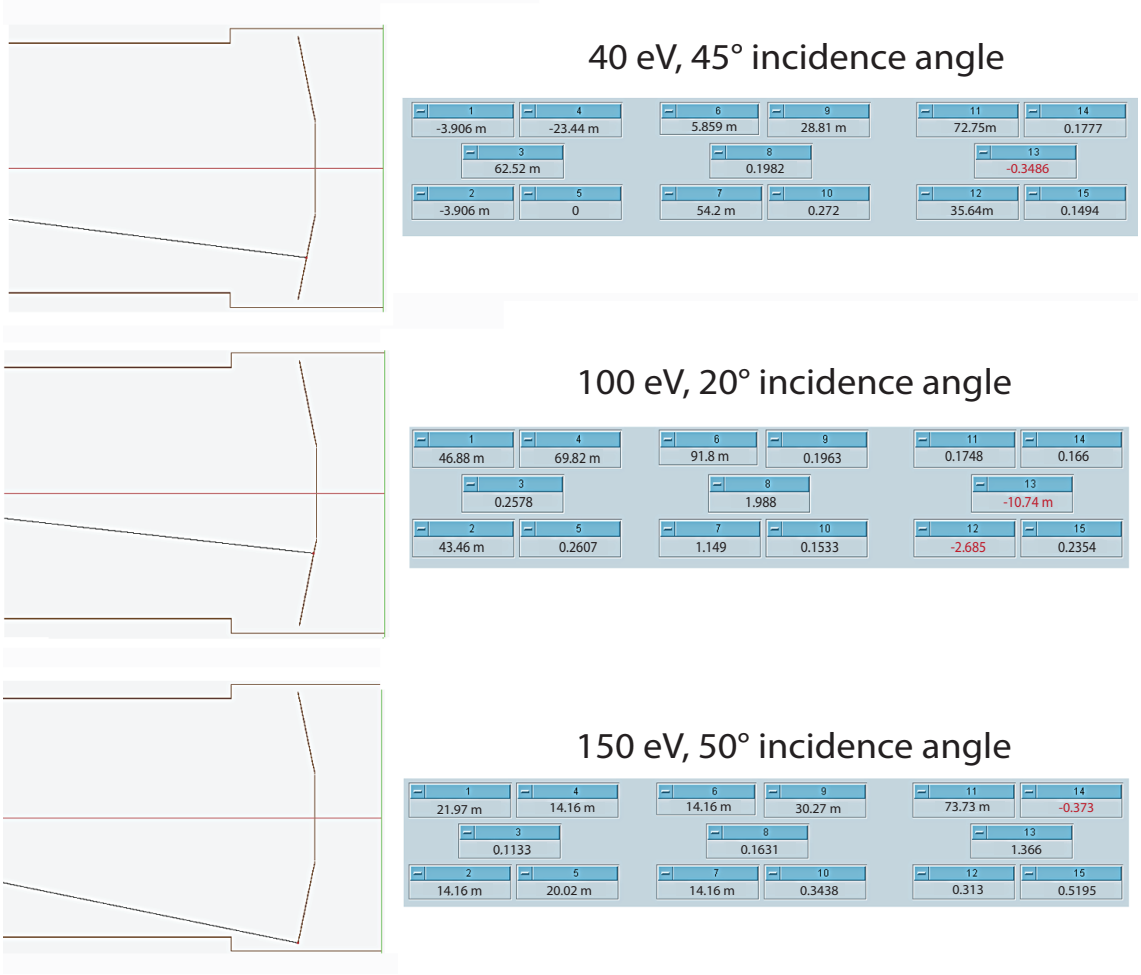

Figure 4.21.: Predicted (left) and measured (right) electron point of impact on the anode for different electron kinetic energies and incidence angles. The point of impact is marked in red in the experimental results. Since electron impact generates secondary electrons, which are driven away from the anode (given the negative anode voltage), the measured current is negative.

Chapter 5.

Attosecond electron dynamics in solids

The application of fs- pulses in a pump-probe setup to date has developed into a standard technique enabling the observation of atomic or molecular motion [80, 45, 6]. Still, access to several fundamental electronic processes e.g. fast electronic transport or screening in metals [42] is only provided in the attosecond regime, the primary timescale of these dynamics. With the advent of attosecond metrology experimental investigations in the gas phase [72, 13, 24, 14] as well as lately on solids [17, 18] became possible. In a proof-of-principle investigation on the (110) surface of tungsten, Cavalieri et. al revealed a time delay of 110 ± 70 as between the emission of core and conduction band photo-electrons for an excitation energy of 94 eV, a result which led to extensive theoretical work [29, 26, 78, 28]. Due to the complex electronic structure of the 5d-metal tungsten, different theoretical models have been used to explain the delay's origin, referring to effects of localization, static band structure or NIR screening (see section 2.4.1). A monocausal theory does not exist as yet.
Recent measurements on W(110) with the same excitation energy of 94 eV revealed a smaller relative delay of 55 ± 10 as [17] than reported by Cavalieri. The difference was explained in terms of possible surface contamination, which, for the case of oxygen on W(110), shifts the relative delays upwards. This delay difference was measured to be ≈ 30 as for an excitation energy of 118 eV and was explained by a shift of the average valence electron distribution and also a shift of the NIR-streaking onset away from the first tungsten layer towards the vacuum. The former would originate from the strong electronegativity of oxygen. While this effect is expected to be enhanced for slower electrons, the large difference of the two retrieved relative delays is still raising questions. In this chapter a new source of delay is identified, namely the chirp of the exciting XUV-pulse. On the basis of a large data set a notable change of the retrieved delay with increasing chirp could be deduced. Depending on the average chirp of the measurements this could explain in combination with an

oxygen induced shift the large deviation between both results.

5.1. Experimental and analytical methods

5.1.1. Mo/Si multilayer mirror for XUV

In the present setup intense, CEP-stable few cycle NIR-laser pulses are provided by a titanium-sapphire laser system with a repetition rate of 3 kHz. These pulses are used not only for the generation of XUV pulses, but as the probe in the following attosecond pump-probe measurements as well. The XUV attosecond (pump-)pulses are generated co-linearly by high harmonic generation (HHG) and are subsequently filtered in the spectral range by a $\approx$ 3.5 eV FWHM bandwidth Mo/Si multilayer mirror centered at 92 eV, resulting in pulses with a duration of $\approx$ 520 as in the Fourier-limited case. Nonetheless, any chirp introduced in the HHG process can lead to larger pulse durations. Since the XUV chirp is dependent on the laser parameters (intensity, bandwidth, NIR-chirp, etc.), the pulse duration can vary with the laser performance. The exact duration of the detected electron wave packet emitted by the XUV pulse can thus only be estimated by numerical analysis of the measured data. In future measurements, the spectrum of the XUV light after HHG will be collected for each streaking spectrogram, which will enable intensity fluctuations and changes in the harmonic generation to be monitored.

The characterization of the XUV-mirror was made in collaboration with Friedmar Senf at the BESSY synchrotron facility. In the employed setup, the monochromatized, high-brilliance radiation from the BESSY radiation storage ring illuminates the sampled mirror and the reflected XUV-light is then detected by a photo cathode, which can be rotated around the mirror. In this way, scanning the wavelength of the incident radiation resolves the actual reflectivity of the mirror in the observed direction. In Fig. 5.1 the results of the measurements performed at BESSY for the 92 eV multilayer mirror are summarized. The spectra have been collected for different detector positions represented by different angles θ, which have been measured with respect to the the surface plane. As can be seen in the red curve, the center energy lies at 92 eV with a spectral width of $\approx$ 3.5 eV for an angle of $\theta = 83°$, as estimated for our setup at the attosecond streaking beamline (AS3). For larger angles the center of energy is shifting to lower energies. Below 90 eV a plateau can be recognized for each curve, which constitutes about 17 % of the peak intensity. The zirconium filter in front of the XUV mirror lowers this value only slightly by not more than 3 % compared to the transmission at the center of the main peak (Fig. 5.1). The plateau can give rise to an enhanced satellite pulse accompanying

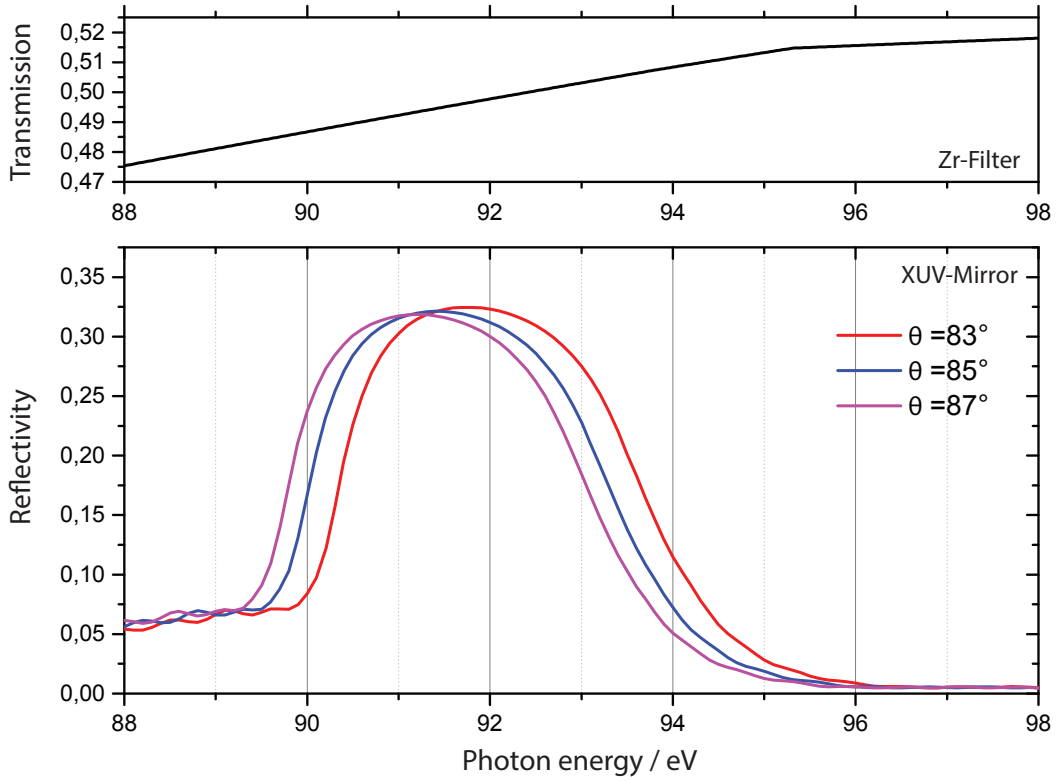

Figure 5.1.: BESSY measurements of the Mo/Si multilayer mirror (lower figure). The mirror is centered at 92 eV with an approximate FWHM bandwidth of 3.5 eV. A shift in energy according to the actual angle of incidence can be noticed. The upper figure shows the filter transmission of the applied 200 nm zirconium filter.

the main attosecond pulse. The influence of such a satellite pulse on the standard deviation of the retrieved XUV- and NIR-parameters was estimated to be quite low, performed with a FROG-type retrieval [103], though recently indications of a larger experimental uncertainty of the retrieved relative delays in correlation with the apparent satellite contribution were found [14]. Nonetheless, by the use of a FROG-type algorithm dubbed Attogram [104] on each spectrogram, which should be able to reconstruct the full XUV-field, no sign of an additional satellite contribution could be found in our data.
On closer examination of 5.1 it is clear that the reflection of the XUV-mirror is not perfectly resembling a Gaussian shape. Though the final spectral pulse shape is determined by the interference of the harmonics [64] and could result in a Gaussian shape, the presence of a Gaussian spectral distribution is not assured. One could then expect an increased uncertainty, because the TSDE-algorithm used for the retrieval is assuming a Gaussian shape for the incident XUV-pulse. It does, however,

have no appreciable effect on the relative delay measured in the attosecond streaking between two peaks, since any deviation in the retrieved values caused by the different shape is identical for each peak and by this, canceling itself in taking the difference for the relative delay.

5.1.2. Tungsten (110) and (100) single crystals

Although the attosecond streaking technique offers a unique tool for the direct, time-resolved observation of electron dynamics with attosecond resolution, the presently available low photon energy ($\leq 130\ eV$) and intensity of the XUV photons as dictated by the HHG -process constrict the measurements to substrates with shallow core levels and corresponding large photoionisation cross-sections. Tungsten is a suitable material of this kind with its strongly localized 4f level at an energy of around 32 eV. Moreover, tungsten can be easily cleaned from surface impurities by standard techniques [105, 106], which is another requirement for an unambiguous interpretation of the results. The procedure involves sputtering of the sample with Ne^+, repeated oxygen treatments and finally flashing of the sample to 2400 K for about 10 s by means of electron bombardment. While it is known that heating of the substrate to 2300 K is efficiently removing tungsten oxide contributions [107, 108], it is not sufficient to achieve an impurity free surface. Rather, carbon is diffusing to and accumulating at the surface, which can be identified in LEED measurements as additional spots accompanying the main pattern [106]. By annealing in a pure oxygen atmosphere ($\approx 3 \cdot 10^{-7}\ mbar$) from 400 K to 2200 K, CO or CO_2 is formed, which then desorbs from the surface even for moderate heating. Such an oxygen cycle is repeated about 10 times, while after the last cycle the sample will be left oxygen covered. Since the oxygen covered surface is inert, any subsequent contamination is prohibited. The sample can then finally be flashed to 2400 K shortly before the measurement to obtain a clean surface. Following this procedure an almost contamination free surface can be achieved. The application of a temperature flash after a time of approx. three hours was enough to continuously retain a clean surface.
Tungsten crystallizes in the bcc structure with a lattice parameter of $a = 3.16$ Å. In this work the (110) and (100) surfaces of tungsten have been investigated. The first Brillouin zone of the crystal is shown in Fig 5.2 with the corresponding symmetry lines of the ¡110¿ and ¡100¿ directions marked, ΓH and ΓN respectively, along with the corresponding LEED patterns. Clear spots can be identified, which are free of additional reflections around the main spots that would indicate a surface contamination. The patterns measured resemble those found in the literature [106, 109, 110]. The LEED pattern of W(100) has been obtained at a temperature of 120 K and is showing additional spots compared to room temperature, which have already been

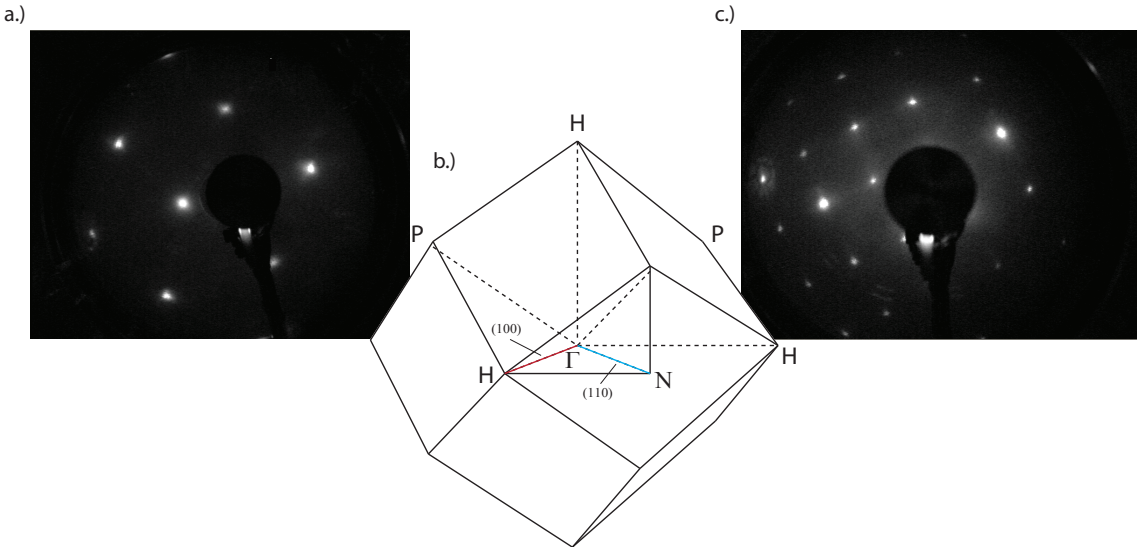

Figure 5.2.: LEED measurement of clean (a) W(110) and (c) W(100). (b) shows the first Brillouin zone of the crystal with the symmetry lines of (110) (blue) and (100) (red).

observed before [111] denoting a temperature dependent phase transition. The work function of W(110) is 5.25 eV, whereas the work function of W(100) is at 4.65 eV [40].
In Fig. 5.3 an XPS-spectrum of clean W(110) observed with Al-Kα radiation (1487 eV) is depicted. In the spectra no indication of oxygen (531 eV binding energy for O1s) or carbon (285 eV C1s) contamination can be found. There have been concerns that the local pressure at the point defined by the XUV/NIR spot diameter is higher than the base chamber pressure ($1 \cdot 10^{-11}$ $mbar$), since the accumulation of surface contaminants seemed to be a lot faster as expected for this pressure range. The source was identified as the time-of-flight (TOF) spectrometer itself, which is placed at a distance of only 3 mm from the crystal surface. In fact, earlier measurements showed the appearance of oxygen on the surface, if the sample was cooled down with liquid nitrogen and placed in front of the spectrometer ($>$ 1hour). In contrast, without the spectrometer involved no oxygen contribution could be found. Yet, a simple bakeout of the TOF spectrometer solved this problem and guaranteed a contamination free surface throughout the measurements.
The spectral structure of tungsten (Fig. 5.3) has its most prominent feature given by the large 4f peak around 32 eV. While the spin orbit splitting is still resolved for the 4d peak ($4d_{5/2}$ at 243 eV and $4d_{3/2}$ at 256 eV), the 4f-splitting is not clearly resolved in this plot. It is shown in the inset of Fig 5.3 taken with 70 eV synchrotron radiation and a final resolution of 73 meV [112]. The $4f_{7/2}$ and the $4f_{5/2}$ peaks reside at 31 eV and 33 eV binding energy, respectively. Each of the peaks is further split into a surface and a bulk contribution as can be seen in Fig. 5.3. This is the

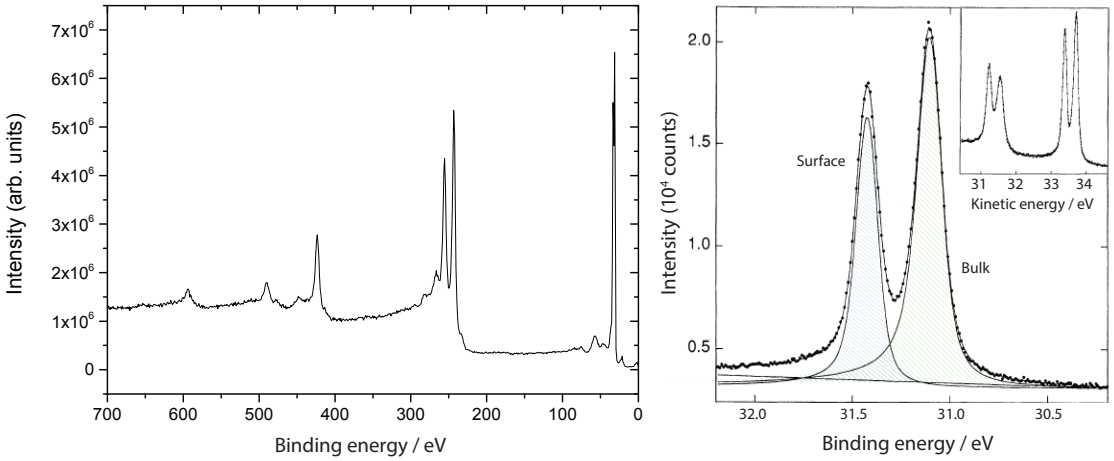

Figure 5.3.: Left side: XPS measurement of W(110) under irradiation with Al-Kα (1487 eV). Right side: Surface/bulk splitting of the W $4f_{7/2}$ peak taken with 70 eV synchrotron radiation and at a resolution of 73 meV (taken from [112]). The inset shows the spin orbit splitting into the W $4f_{7/2}$ and W $4f_{5/2}$ peak.

known surface core-level-shift at a value of 321 meV [113], which arises due to a different coordination number at the surface compared to the bulk. For the applied photon energy of 92 eV, it has been shown before [31] that the surface related peak comprises over 50 % of the total (surface plus bulk) emission, denoting a high surface sensitivity. In general, perturbation of the lattice and the electronic states arises only down to a small depth, in some cases solely confined to the first surface layer. In the same way, contractions of the interlayer spacing in tungsten just appear for the first layer (W(100)) or cannot be measured at all (W(110)) [109]. This would mean a vanishing surface contribution in a normal XPS measurement. However, the small escape depth of the electrons of approx. 3 layers for the energies employed here ($\approx 40 - 90$ eV) gives a drastically enhanced surface sensitivity. The 4f peak is accompanied by the comparatively weak $5p_{3/2}$ peak at 37 eV binding energy. The conduction band covers a width of 10 eV and is well separated from the 4f levels by approx. 29 eV, thus allowing attosecond streaking measurements with decent streaking amplitudes. Tungsten has been studied intensively before [114, 115, 116] and the experimental data considering the conduction band was found to be in good agreement with band structure calculations by Christensen [117, 118]. It is governed by direct transitions from the partly localized 5d-bands and minor contributions from the weakly localized 6sp-states [119], which exhibit wide energy bands and therefore a broad density of states. Also several contributions without notable energy dispersion could be identified as surface states and resonances in the conduction band spectra [120, 114]. For W(100) the situation is similar [121, 115, 122]

with, of course, different direct transitions following the band structure along the corresponding symmetry direction.

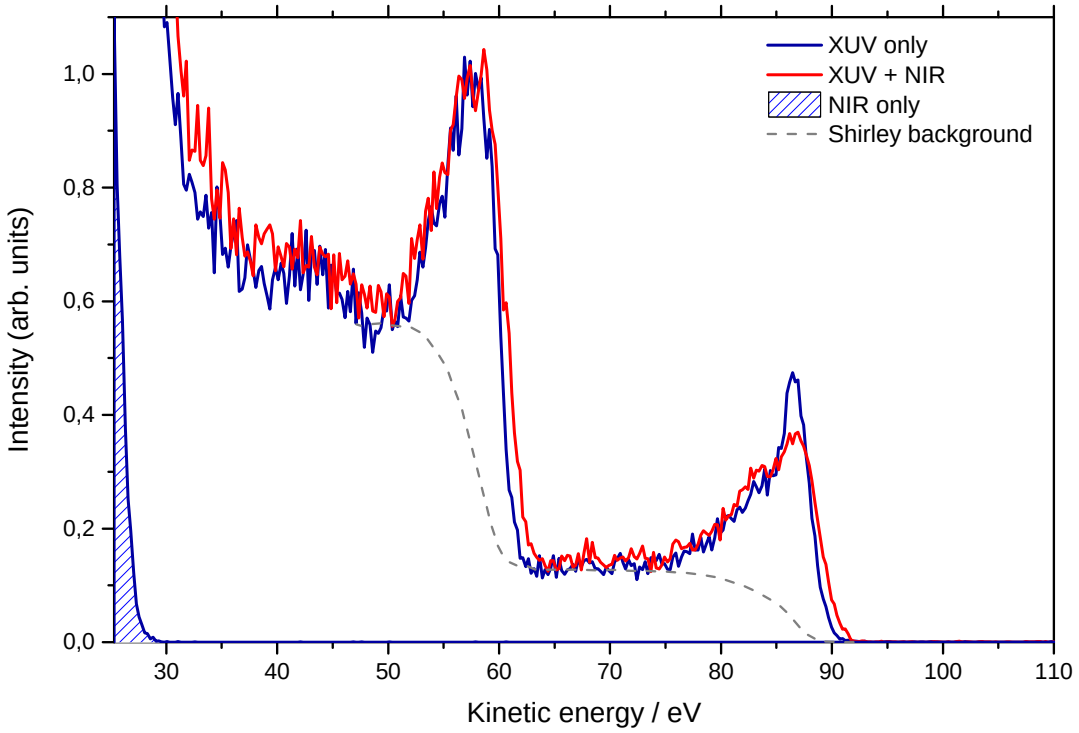

Figure 5.4.: Spectra taken under excitation with the 92 eV XUV-mirror only (blue curve) and simultaneous irradiation of NIR-light (red curve) with a -30 fs delay between NIR- and XUV-pulses. The spectrum mostly preserves its shape and is slightly shifted in energy under the influence of the NIR. The shaded blue curve denotes a measurement of the ATI electrons produced by NIR excitation. The calculated Shirley background of the spectrum is shown in gray.

Owing to the large bandwidth inherent (and compulsory) to attosecond pulses, in our spectra, the peaks are significantly broadened comprising all fine structure. Thus, as can be seen in Fig. 5.4, the $4f_{7/2}$ and $4f_{5/2}$ peak in combination with the weak contribution of the $5p_{3/2}$ peak merge to a broad feature at 58 eV kinetic energy and, in the same way, the conduction band is observed as one broad peak at 87 eV kinetic energy. On closer inspection, another peak accompanying the 4f-peak can be identified at an energy of 42 eV. As the energy-loss function of tungsten peaks at an energy around 25 eV with several bulk and surface plasmon contributions beginning to appear at 10 eV and higher energies [123, 106], these can be (and partly are) attributed to plasmon losses. However, it is also known that saturation effects subject

to the electron detection process can create an artificial peak in the same region. Since the detection of incoming electrons is prevented during the dead time of the TOF discriminator (3 ns) as has been discussed in detail before (section 4.1.1), a saturated peak is followed by a sudden drop in intensity for lower kinetic energies (denoting later arrival times respectively). Thus, a side peak can be formed. Even though attention has been payed as to not drive into saturation, this effect cannot be excluded.
The background in the observed spectra is built up of two main contributions: In the low (kinetic) energy region, an effect equivalent to above threshold ionization (ATI) is dominant, which is shown in Fig 5.4 as the blue curve depicting a NIR-only spectrum without any XUV intensity. The process is describing the absorption of several photons of the NIR-laser field by the emitted electron and in this way is largely intensity dependent. The ATI-intensity is zero down to an energy of 30 eV, while at lower energies the intensity is raising exponentially to a large value. Care has been taken to retain a large enough distance between the ATI onset and the 4f-peak, so that the streaking of the peak is not perturbed in any way. The ATI-electrons are actually not subject to the streaking effect (supplement [17]), since the appearance of streaking relies on temporally coherent electron wave packets [72]. The second contribution to the background is inelastic scattering of the outgoing electron upon the travel to the surface. For the kinetic energies depicted here, this means dominantly electron-electron-collisions. In the observed photoelectron spectra this leads to an asymmetric tail of the peaks. One could argue that the inelastically scattered electrons, which will inevitably be included in the analysis of the peak upon determining the relative delay, will shift the overall delay. Yet the additional delay of electrons, scattered only a few times, can be expected to be in the range of only 10 as [124]. The removal of the background is a standard procedure in XPS. In the same way, the background has been subtracted from the attosecond streaking spectrograms by subtracting a background of each spectrum. The best results could be achieved with the reciprocal Shirley procedure, which empirically determines the background by integrating over the intensity of all higher energetic electrons. The resulting background is depicted exemplary in Fig. 5.4 . Whether the application of the Shirley background gives more reliable results with regard to the retrieval of the relative delay strongly depends on the accuracy of the calculated background itself. However, the “true” background is not known and cannot be directly derived from our experimental measurements. Therefore, each spectrogram has always been analyzed in our retrieval algorithm with and without a subtracted background. A theoretical analysis yielded a difference in the retrieved delay between these two spectrograms for large EWP-chirp, which will be discussed in section 5.3.1.
In Fig. 5.4 additionally to the XUV-only spectrum, a spectrum under influence of the NIR-field is shown as red curve. For this spectrum, the NIR-pulse was set to arrive 30 fs before the XUV-pulse. Despite this large temporal delay, a spectral shift can be observed while the shape of the peaks stays mainly intact. The origin of this

effect can be traced back to the generation of space charge by the NIR-laser pulse [125, 126]. The Coulomb interaction with this space charge cloud is, irrespective of the large temporal separation, strong enough to induce notable spectral distortions and shifts. In a recent study of space charge effects on W(110) [127], a significant broadening of up to 2 eV was found for a photon count exceeding 10^7 photons per pulse. This effect might be weaker in our system providing approx. 10^6 photons per pulse ($\approx 5 \cdot 10^{11}\ W/cm^2$) and is certainly superposed by the broad bandwidth of the XUV-mirror. In analogy, no spectral broadening can be noticed in the spectra. However, a spectral shift of the XUV-NIR spectrum is present in Fig 5.4 , which amounts to about 0.9 eV in our case in conformity with [127] and earlier observations [31].

5.1.3. Analytical methods

Center of energy approach (COE)

In extension to techniques like XPS and UPS, which offer fine spectral resolution, attosecond streaking spectroscopy represents a promising new tool sacrificing spectral information to achieve unprecedented resolution in the temporal domain. As the absolute transport times of electrons to the surface cannot be retrieved so far, mostly because the absolute delay between the XUV and the NIR pulse is not known with attosecond resolution, yet the relative delay between electrons from different states can be restored. Fig. 5.5 shows exemplary a streaking spectrogram on W(110) in a false-color plot with electron (kinetic) energy plotted against the delay between the XUV- and NIR-pulse. The peaks at 58 eV and 87 eV can be identified with the W4f and conduction band (CB) electrons, respectively. As soon as the electrons reach the surface, their energies are modified by the NIR and thus, the oscillations in energy resemble the NIR vector-field. It is clear that a phase shift between the two curves for W4f and CB denotes a temporal delay of the corresponding electrons. Several schemes have been developed to extract this delay from the streakings. The first approach on this topic, already used in the analysis of [17], is based on a center of energy (COE) approach. Here, in a first step the spectrogram is divided energetically in two regions of interest, each of them comprising the full streaking curve of one peak respectively. In this range of energies defined by E_{min_i} and E_{max_i} with i denoting the number of the peak, the COE is calculated for each delay point according to

$$E_{COE_i} = \frac{\sum_{E_{min_i}}^{E_{max_i}} I(E) \cdot E}{\sum_{E_{min_i}}^{E_{max_i}} I(E)} \tag{5.1}$$

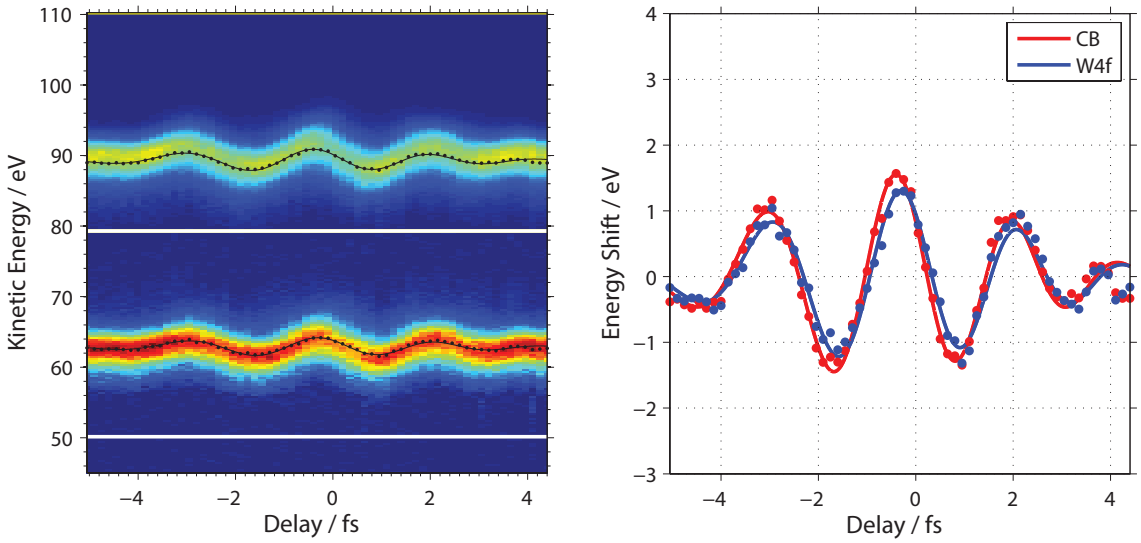

Figure 5.5.: COE retrieval on a spectrogram taken at 92 eV excitation energy on W(110). Left side: Original data with the retrieved COE's superimposed (black dots). The fit to these points is shown as black curve. Right side: Retrieved COE's for the CB and W 4f peak and the corresponding COE fits to these points.

Following this scheme, the center of gravity of each spectrum at each corresponding delay is calculated. Tracking of these centers of energy over the delay gives a curve, which is determined by the integral over the NIR- electric field starting from the instant of the given XUV-NIR delay and consequently closely resembles the NIR-vector potential. The retrieved streaking can now be fitted by a curve describing the NIR oscillations by

$$E_{COE_1} = A_1 \cdot e^{-4\ ln2 \cdot ((t_x - t_{0_1})^2/\tau^2_{FWHM})} \cdot \sin(\frac{2\pi \cdot (t_x - t_{0_1})}{T_{laser}} + \beta\ (t_x - t_{0_1})^2 + \Phi_{CEP}) + E_{0_1} + E_{Drift} \cdot t_x \tag{5.2}$$

In this case, A_1 is the streaking amplitude, t_{0_1} is a time zero initial shift of the NIR envelope, τ_{FWHM} is the FWHM of the NIR-pulse, T_{laser} the laser period, β the chirp of the NIR-pulse, Φ_{CEP} the carrier envelope phase, E_{0_1} the mean peak energy and finally E_{Drift} the drift in energy, which can arise in time due to accumulation of space charge. The second peak is fitted with exactly the same formula and parameters, except for the amplitude A_2, the mean peak energy E_{0_2} and most importantly an additional delay $t_x + t_{12}$ as free parameters. Fitting with this additional parameter now directly gives the shift of the streaking of peak 2 corresponding to the first peak t_{12}. Within this simple model, the relative delay can be quickly retrieved without any assumptions, e.g. about the spectral shape of the electron wave packet. The

method gives reasonable results, but the standard deviation of the retrieved values is relatively large (up to 100 *as* in the worst case), since shot-to-shot fluctuations of the laser or pulse shape variations are strongly reflected in a shift of the COE. Therefore, this method has only been used in our measurements to cross check the retrieved delays. It should be noted, however, that its comparison with other applied methods yielded a good agreement for our measurements.
As can be seen, the streaking curve in equation 5.2 is, except for the energy values, completely described by laser parameters in this model. As a result no information about the XUV-pulse itself, especially the XUV-chirp, can be retrieved. The spectral information corresponding to the variation of intensity over energy, I(E), is only used in the beginning to retrieve the COE and is completely neglected henceforth. This is one disadvantage of the COE method and lead to the inclusion of a more advanced approach based on an approximated solution of the time dependent Schrödinger equation (TDSE).

Time dependent Schrödinger equation approach (TDSE)

The TDSE retrieval is taking into account the full spectral information by fitting the temporal evolution of the emitted electron wave packet (EWP) against the delay to the experimental data in a nonlinear least-squares fitting routine. Several groups have studied this topic theoretically with regard to the atomic response in gas phase x-ray photoionisation experiments [36, 65, 128]. Their work describes the interaction of a photoelectron with the dressing NIR-field and in this sense can easily be expanded to depict the spectrograms retrieved in the solid state case. Following the approach of [129] we begin with the time dependent Schrödinger equation as given by

$$\left(\frac{1}{2}\cdot(\mathbf{p}+\mathbf{A}_L(t))^2+V_{eff}(\mathbf{r})+\mathbf{E}_X(t)\cdot\mathbf{r}\right)\ |\Psi(t)\rangle = i\frac{d}{dt}\ |\Psi(t)\rangle \tag{5.3}$$

in the dipole approximation as the wave phase is mostly independent on the position. $\mathbf{p}$ denotes the canonical momentum, $\mathbf{A}_L$ is the NIR-vector potential, V_{eff} is the screened ionic potential and $\mathbf{E}_X$ is the ionizing XUV-field. Atomic units will be used here unless denoted otherwise. Equation 5.3 is only describing the laser interaction with a single electron (single active electron approximation (SAE)), while the effect of the remaining electrons is solely contained in the effective ionic potential V_{eff}. With the use of the time-evolution operator $U(t,t_0)$, which evolves an electronic state vector in time according to $|\psi(t)\rangle = U(t,t_0)\ |\psi(t_0)\rangle$ and is fulfilling the TDSE

itself, the vector solving equation 5.3 is given by

$$|\Psi(t)\rangle = -i \int_{t_0}^{t} dt' \; U_L(t,t') \; \mathbf{E}_X(t') \cdot \mathbf{r} \; U_L(t',t_0)|\Psi(t_0)\rangle \tag{5.4}$$

Within this description already two valid assumptions have been made: The NIR-field is not producing any ATI electrons in the range of the observed photo emission peaks and the XUV field is generally too weak to influence photo emitted electrons. Both approximations are generally true for the XUV and NIR intensities applied in our experiments. As a consequence the time evolution can now be evaluated by $U_L(t,t_0)$, which solely describes the laser-electron interaction. In order to receive a theoretical reconstruction of a photoelectron spectrum, the electronic state vector has to be projected on momentum space given as $\langle \mathbf{p}|$. The interaction of the time-evolution operator $U_L(t,t')$ upon momentum projection can be described in the strong field approximation (SFA) by Volkov states with the Volkov phase as

$$\Phi_V(t,\mathbf{p}) = -\int_{t}^{\infty} dt' \; \frac{1}{2} \; (\mathbf{p} + \mathbf{A}_L(t'))^2 \; . \tag{5.5}$$

The second time-evolution operator can then be approximated by $U_L(t',t_0) \approx e^{-iE_{kin}(t'-t_0)}$, since it denotes the time evolution of the bound state before ionization. In combination this yields for the reconstruction of the photoelectron spectra as given by the probability distribution against momentum and time

$$I(\mathbf{p},\tau) = \left| \int_{-\infty}^{\infty} dt \; \mathbf{E}_X(t) \; D(\mathbf{p} + \mathbf{A}_L(t+\tau)) \; e^{iS(\mathbf{p},t,\tau)} \right|^2 \tag{5.6}$$

$$S(\mathbf{p},t,\tau) = \Phi_V(t+\tau,\mathbf{p}) + E_{kin} \cdot t \tag{5.7}$$

D($\mathbf{p}$) is denoting the dipole matrix, that depicts the transition from bound to continuum state, and τ is the delay between XUV- and NIR-pulse. The first term $\mathbf{E}_X(t) \cdot D(\mathbf{p})$ denotes the probability amplitude for the transition, while $S(\mathbf{p},t,\tau)$ actually describes the quasiclassical action as can be seen in [36]. Neglecting the influence of the dipole matrix, which can usually be done far away from atomic resonances, the electron-laser interaction is defined by the term $S(\mathbf{p},t,\tau)$. Consequently, the Volkov phase Φ_V drives the interaction of the launched wave packet with the laser.
The TDSE algorithm is now following basically the same path: At first, an electron wave packet is created by

$$\xi(t) = E_X(t) \cdot e^{ibt^2} e^{i\Phi_V} \; , \tag{5.8}$$

where $E_X(t)$, the XUV field, is described in the Gaussian form and b denotes the linear EWP chirp. The Volkov phase is calculated according to equation 5.5, where the vector field $A(t)$ is also represented in Gaussian parameters and the NIR-field chirp b_{NIR} and the carrier envelope phase Φ_{CEP} are included as additional variables of $A(t)$. In the following, the wave packet is Fourier-transformed and squared to receive the form as given by equation 5.6 and finally, the retrieved spectrum is fitted in a nonlinear least-squares fitting routine to the actual data. In a recent change, the least-squares algorithm is now not fitting to the difference between real and calculated spectra, but to the difference between their derivatives. This makes the fitting more stable against unwanted influences, that do not vary against the delay. The procedure is repeated for each peak with individual wave packet parameters and then finally combined to receive the total spectrum.
Since the individual states, e.g. by spin-orbit-splitting within a peak cannot be resolved or distinguished, the algorithm is not including an individual delay of these states even though latest measurements indicate that such a delay between atomic states is possible [14]. Here, a relative delay of 21 ± 5 as between the 2p and 2s orbital of neon was found. In the same way, there is just one parameter for amplitude, chirp, FWHM and central frequency of each peak. Yet the parameters between the peaks can vary, allowing, for example, the retrieval of a different chirp between W4f and CB states.

Frequency resolved optical gating approach (FROG)

FROG is a known method to characterize ultrashort pulses by means of sampling the pulse with the help of a gate, which is defined by the pulse itself. This is generally achieved by focusing the pulse and a delayed replica of itself in a nonlinear crystal. Analyzing the resulting spectrum against the delay τ with a numerical algorithm retrieves the gate $G(t+\tau)$ and the temporal dependence of the pulse $E(t)$. A FROG spectrogram can then be described as [130]

$$I(\omega, \tau) = \left| \int_{-\infty}^{\infty} dt \; E(t) G(t+\tau) \; e^{i\omega t} \right|^2 . \tag{5.9}$$

At a first sight this formula looks very similar to the equation given by 5.6 and in fact it can be converted into the given form allowing the application of the FROG algorithm on attosecond streaking spectra to give a full characterization of the attosecond XUV-pulse [131, 104]. In this context, the laser-electron interaction works as a phase gate with its value given by

$$G(t) = e^{-i \int_t^{\infty} dt' \; p_C A_L(t') + \frac{1}{2} \; A_L^2(t')} \tag{5.10}$$

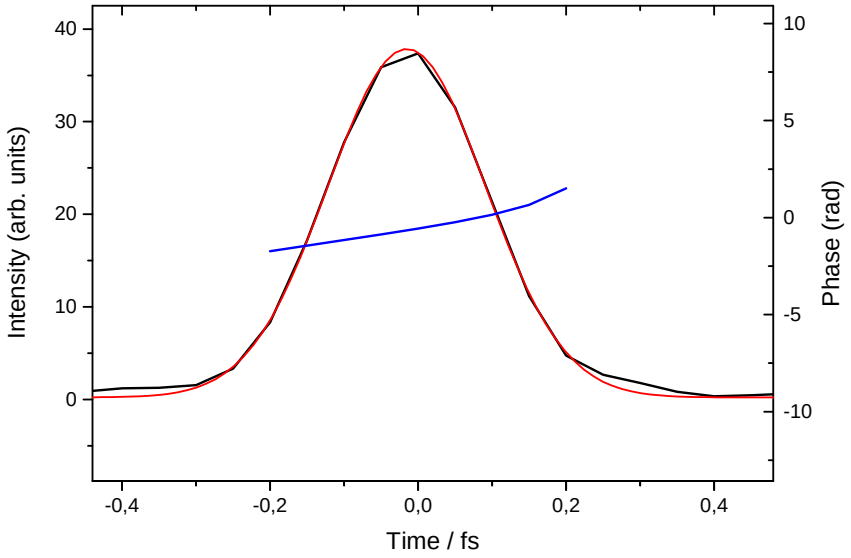

Figure 5.6.: Temporal profile of an emitted electron wavepacket as retrieved by the FROG algorithm. The temporal distribution fits well with a Gaussian fit, shown as red curve. The FROG routine is also able to retrieve the temporal phase from the data, which is shown as blue curve.

where p has been approximated by the unstreaked average momentum p_C. The algorithm has been implemented in a program dubbed "Attogram" by Justin Gagnon et al. [104], which is a useful tool to reconstruct the initial XUV-pulse and its parameters, in particular its chirp. It has been used for the analysis of our data to cross check the wavepacket chirps retrieved by the TDSE algorithm and to verify that the actual pulse form after shaping by the XUV mirror is primarily preserving a Gaussian shape as can be seen exemplary in Fig. 5.6 showing the result of a FROG retrieval. The retrieved values for the chirp also supported the TDSE data within the experimental uncertainties.

5.2. Attosecond streaking spectroscopy on solids

One question arising from the theoretical treatments on the attosecond streaking delay so far has been, whether there are final state effects that dominantly influence the measured delay between core and conduction band electrons. Different group velocities could thus originate as a result of band structure effects. One way to examine this effect is to vary the central XUV photon energy to examine a possible

energy dependence of the delays. However, the escape depth varies with the central photon energy and moreover, theoretical treatments point to a correlation between group velocity and escape depth [26], which further complicates the discussion.
By observing different crystal orientations of the solid for the same photon energy it is possible to decorrelate these effects. Here, the parameters of the photo-emission process stay fixed and the results can be evaluated for comparable escape depths, but different band structures. With this in mind, a series of more than 100 streaked photoelectron spectra have been taken for W(110) and W(100) each, resulting in a large statistical setting of the streaking measurement. This way an in-depth analysis of eventual dependencies of the laser or electron wavepacket parameters is possible.

The analysis yields a discrete trend of the retrieved streaking delay against the measured EWP chirp. It was found that it consists of two primary linear contributions: One, which seems to be an intrinsic property of the solid and varies for different crystal orientations as well as conduction band and core electrons, and one, which is dominant for large (negative) EWP-chirps beyond $-10\ fs^{-2}$. The former shows an remarkable agreement with a chirp to delay dependency induced by atomic effects. In particular, simulated spectra under inclusion of cross-section variations of the W 4f and W 5d states give the same linear trend. The latter one is analyzed in terms of simulated spectra in section 5.3.1 with differently chirped wavepackets. The simulations show that a present chirp in combination with the large pulse width of the electron wave packets (EWP) gives the expected occurrence of a strong narrowing and broadening of the final pulse line width in the zero crossing of the NIR-vector potential. However, for large (negative) chirps (beyond $-10\ fs^{-2}$), the background cannot be separated properly resulting in an erroneous modification of the retrieved streaking field especially in the zero crossings, which is most dominant for the conduction band electrons. This behavior gives an erroneous retrieval of the relative delay, most profound for EWP-chirps lower than $-10\ fs^{-2}$, which is strictly dependent on the sign and magnitude of the chirp, as will be shown in section 5.3.1. Spectral line shape variations [132] around the NIR-vector field maxima, which can be seen in some spectra, could enhance this effect. Finally, remaining deviations in the (intrinsic) chirp dependence between W(110) and W(100) for lower EWP-chirps are analyzed and discussed in terms of band structure effects.

5.2.1. Tungsten in the (110) crystal orientation

In the first large data series obtained with the 92 eV mirror, tungsten oriented in the (110) direction, which was already examined in the measurements by Cavalieri [17], was revisited and showed an previously unobserved behavior. The retrieved, relative delay between the CB and W 4f peak of W(110) now seemed to be depen-

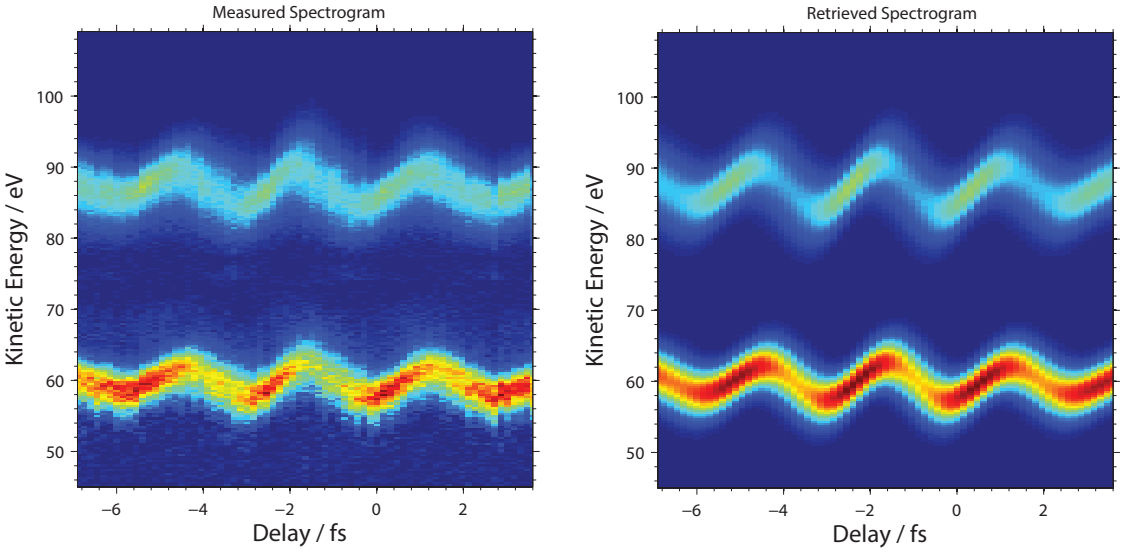

Figure 5.7.: Exemplary measured streaking spectrogram on W(110) (left side) and the retrieved spectrogram, derived by the TDSE routine.

dent on the subtracted background for some spectra. The differences of the relative delays between spectra with and without subtracted Shirley background are ranging between maximal values of -70 *as* and $+80$ *as*. In order to investigate this large deviations, a careful analysis of different laser and electron wavepacket parameters plotted against the streaking delay has been undertaken to evaluate possible dependencies. The corresponding plots of the evaluated, background subtracted data are presented in Figs. 5.8, 5.9 and 5.10. In each plot, those data points, exhibiting the same relative delay before and after background subtraction, are marked in blue.
The attosecond pulse duration, as plotted in Fig. 5.8, does not show any dependence corresponding to the retrieved relative delay. It can be noticed that the data points susceptible to the background subtraction seem to be primarily shifted to values of larger delay in comparison to the subtraction-independent points. This behavior seems to create a double-peak Gaussian structure in the frequency of occurrence of the delay values. In contrast, the distribution of the blue-marked points (including only the BG subtraction-independent points) fits well with a Gaussian as can be seen in Fig. 5.8. As the natural contribution, which arises due to the statistical variation of the measured values (as result of e.g. intensity variations or timing jitter), is of Gaussian shape, this is a strong hint that a systematical error is present for the subtraction-dependent data points, most probably arising through a wrong retrieval of the background subtracted data. A possible reason for this modification will be discussed in section 5.3.1. On inspection of plot 5.8, also no dependence on the laser intensity could be noticed. Nonetheless, a few data points for very high laser intensity have been left out since saturation effects, an aggravated subtraction of the background as part of the larger streaking amplitude and enhanced space

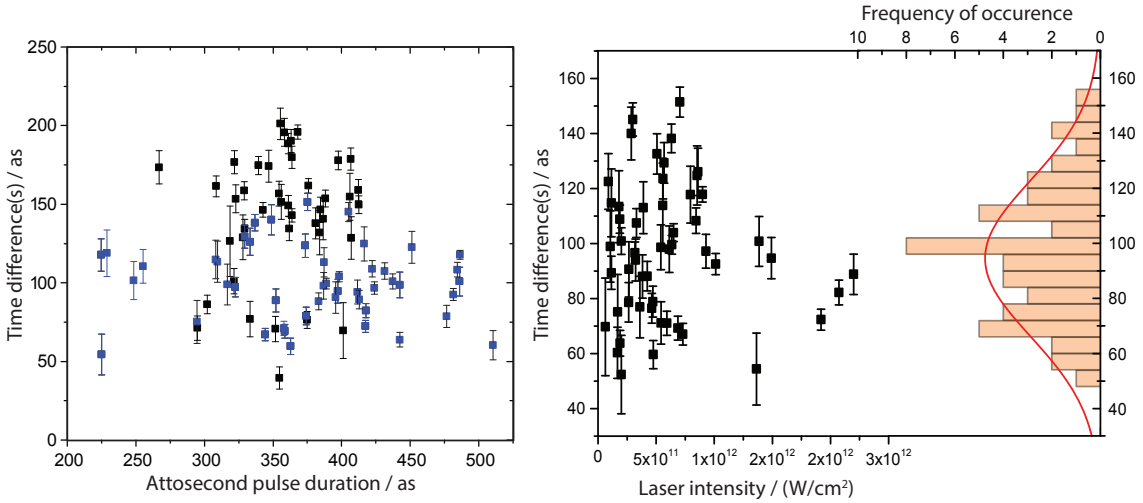

Figure 5.8.: Relative delay as a function of attosecond pulse duration and NIR intensity for the W(110) crystal. Data points that have been found to be independent of the background subtraction are marked in blue. The right plot solely shows these data points. The bars on the right side of the intensity plot show the frequency of occurrence of the relative delays. They resemble a Gaussian fit, shown as red curve.

charge effects could become significant with a large intensity. Also an interaction with the NIR field in the solid could lead to an enhanced influence of the electron movement and a reduced delay. Though this shift in time is expected to be rather small (less than 10 as) even for large intensities [29].
In Fig. 5.9 the delay is plotted against the applied voltage of the TOF spectrometer and also against the day in which the data was collected in order to find dependencies according to the day-to-day laser performance. Before the TDSE analysis, each spectrogram has been corrected for the TOFs energy dependent transmission function according to the applied lens voltage. Therefore, in principle, there should be no dependence of the retrieved delay values against the lens voltage. A small dependence in the given data can, yet, be noticed, which may be rather attributed to a variation in the average delay according to the day-to-day variation in the laser performance. This correlation arises, since many of the measurements for the same lens voltage also stem from the same day. This is also supported by previous measurements, where no dependence in the same range of voltages could be found [31].
In plotting the relative delay against the NIR pulse duration (Fig. 5.10) a slight linear dependence on the duration can be observed. This dependence vanishes when considering solely the subtraction-independent points and seems to be artificial. Taking into account other reasons, a larger NIR-pulse duration could enhance satellite contributions as the spectral separation of the generated XUV-pulse trains is diminished. Otherwise, there also could be an erroneous retrieval of the NIR pulse

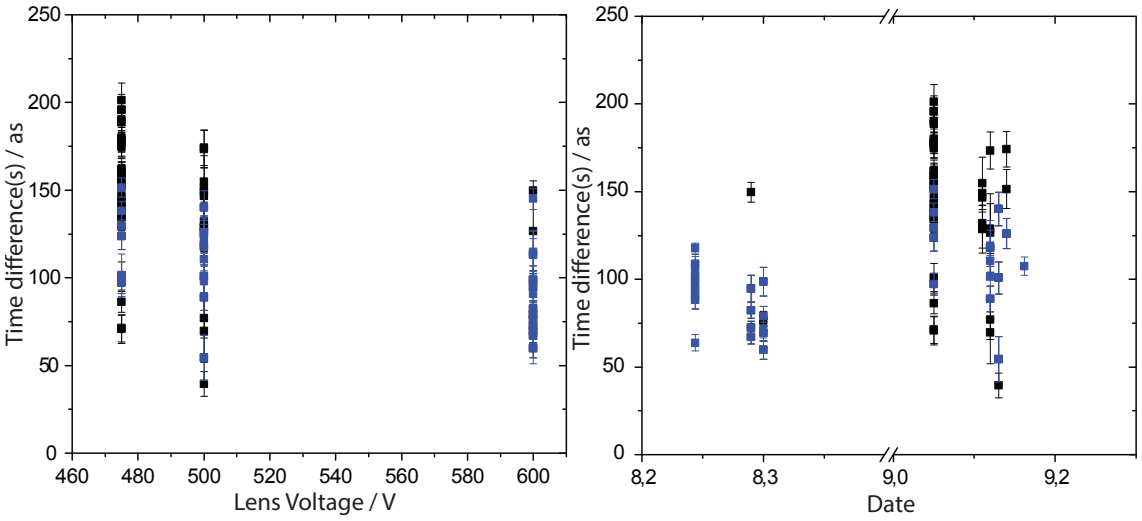

Figure 5.9.: Relative delay versus TOF lens voltage and day-to-day performance for the W(110) crystal. Data points independent of the background subtraction are marked in blue.

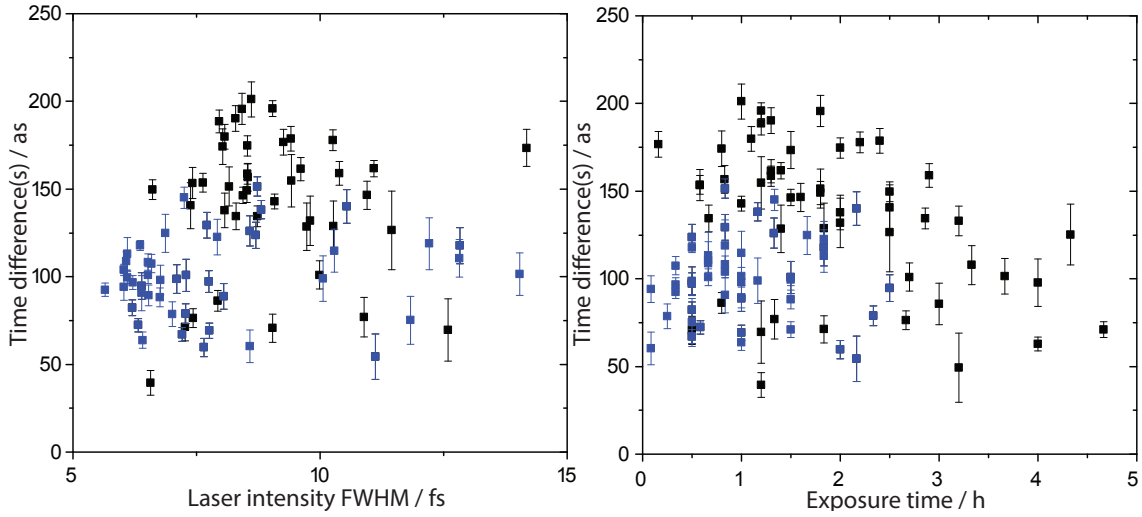

Figure 5.10.: Relative delay versus NIR pulse duration and time after the last cleaning of the sample for the W(110) crystal. Data points independent of the background subtraction are marked in blue.

duration itself for larger durations, since they were partly not scanned over the whole delay range and were thus truncated for large durations.
On the right side of Fig. 5.10, the retrieved streaking delay is plotted against the exposure time of the sample in vacuum after a flash to 2400 K at time zero. Up to a time of 3 hours the delay appears to be unaffected by the exposure time and

therefore free of possible surface contamination. Moreover, no changes of the form of the conduction band could be noticed within this time, which can also be acknowledged as a measure of the surface cleanness. For times greater than 3 hours the delay seems to be lowered in its average value. Thus, the corresponding spectra with exposure time, exceeding the limit of 3 hours, have been excluded from the analysis.

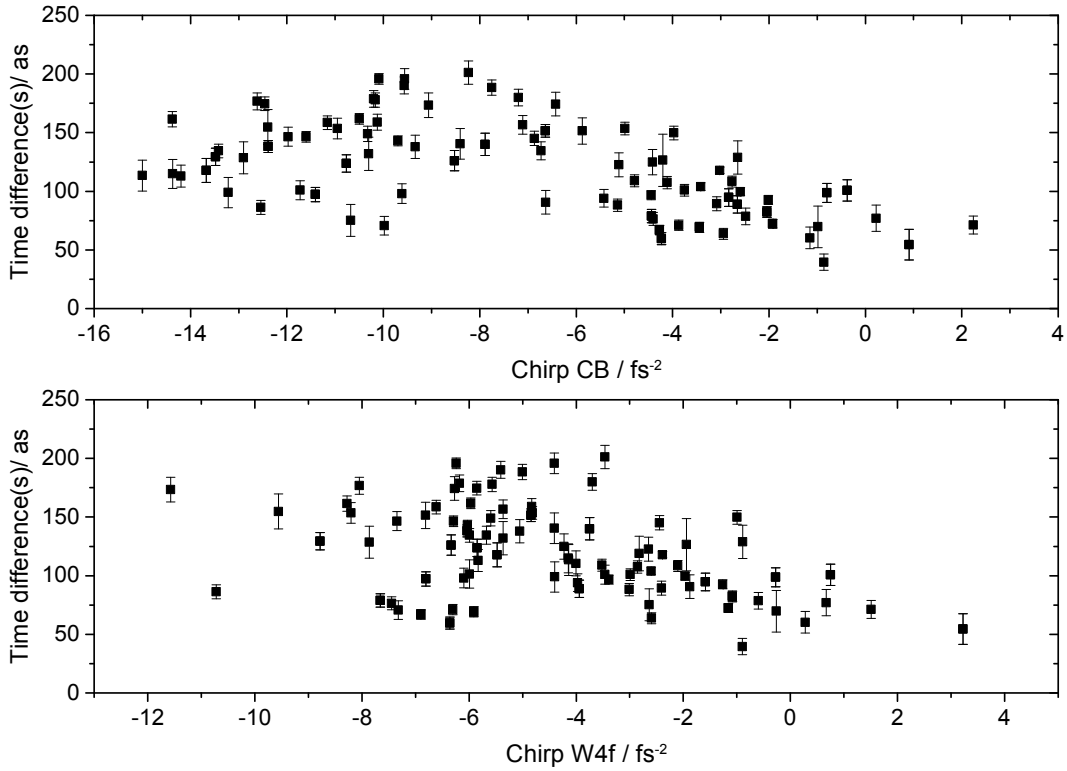

Figure 5.11.: Plot of the relative delay against the EWP chirp as retrieved for the conduction band (top) and the W 4f core level (bottom) for W(110).

At last, a dependence on the retrieved linear wavepacket chirp was examined as can be seen in Fig. 5.11. For a EWP-chirp more positive than $-10\ fs^{-2}$, the data generally show a linear decrease of the retrieved delay with increasing chirp. For a lower chirp value another contribution seems to become dominant and a linear dependence with a different slope emerges. This behavior will be discussed in detail in section 5.3.1. Upon comparison of the chirp dependence of W 4f and CB electrons above $-10\ fs^{-2}$, the CB electrons depict a slightly larger slope of the linear dependence. In general, the chirp values cover a large range compared to previous measurements starting from $-15\ fs^{-2}$ up to $4\ fs^{-2}$ for the conduction band. Since the chirp introduced by the XUV mirror is fixed, the variation can either be produced in the course of high harmonic generation, where changes in the laser parameters (espe-

cially the intensity and the NIR-field chirp) lead to a different XUV pulse chirp. On the other hand, an additional chirp could be introduced in the solid itself, where different group velocities for different initial energies exist e.g. as result of the material's band structure. The chirp would then be mostly dependent on the bandwidth and central energy of the exiting XUV pulse. The latter explanation would also explain the different retrieved chirp values for the W 4f and CB EWPs of the same measurement. It should be noted that older measurements with approx. zero chirp for a 94 eV mirror with 6 eV bandwidth gave relative delays of $\Delta\tau = 55 \pm 10$ as [31]. This value is in agreement with our measurements.

In a first evaluation, it is certainly reasonable to solely analyze those data points that do not exhibit a dependence on the background subtraction, marked in blue in Figs. 5.8, 5.9 and 5.10. Possible reasons for the observed deviations are discussed in section 5.3.1, which will allow a detailed analysis of the chirp dependence in section 5.3.2. The analysis of the separated data now yields an average relative delay between the CB and W 4f electrons of 98 ± 25 as, an average CB chirp of -5 ± 4 fs^{-2} and a W 4f chirp of -3 ± 3 fs^{-2}. Though this is in good agreement with the measurement of Cavalieri [17] with its final delay of 110 ± 70 as, the present chirp dependence of the data renders the approach of averaging over all values questionable. A detailed analysis of the chirp dependence is needed as will be given in section 5.3.2. Nonetheless, comparison of the retrieved delay with previous measurements [17] shows that the standard deviation is greatly reduced. This argues for recent improvements of the setup concerning mostly lower surface contamination by an improved vacuum, a higher laser repetition rate and improvements in the data analysis as, for example, the inclusion of the TOF transmission function [31]. The averaged FWHM pulse duration retrieved by the algorithm is $\Delta\tau_x = 390 \pm 64$ as. As observed in other measurements, this value is unrealistically small compared to the supported pulse duration of the mirror design at 520 as. This is a result of fitting a single electron wave packet to the data in the course of the TDSE algorithm, whereas in reality the data is an average over many electron wave packets accumulated over various laser shots [103]. Thus, shot-to-shot fluctuations and the spatio-temporal profile of the laser [1] can smear out the total wavepacket in the spectral range. The finite energy resolution of the TOF spectrometer adds to this spectral broadening, which in the end leads to a misinterpretation as a lower pulse duration. Since the measured delay is only dependent on the shift of the peaks (shift of the streakings), it is independent of this deviation. This assumption is corroborated by the independence of the retrieved delay on the attosecond pulse duration, which shows that the false retrieval of the pulse duration does not influence the retrieval of the delay.

[1] The spatio-temporal variation of the laser intensity can, for example, lead to a variation of the cut-off energy at different points in space, thereby, in average, smearing out the spectrum.

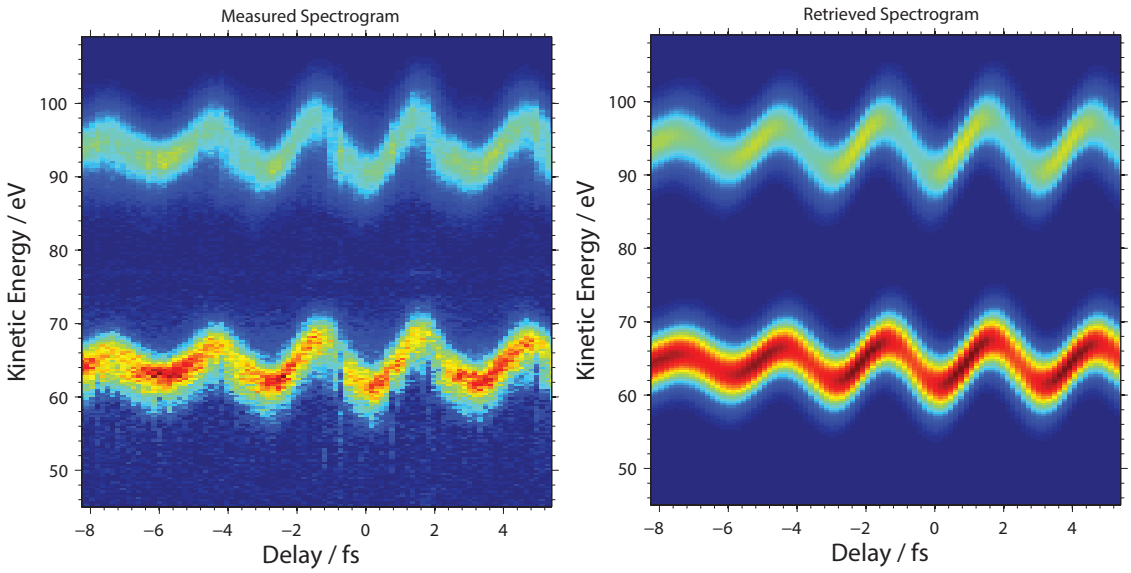

Figure 5.12.: Exemplary measured streaking spectrogram on W(100) (left side) and the retrieved spectrogram, derived by the TDSE routine.

5.2.2. Tungsten in the (100) crystal orientation

The data series of the (100) orientation of a tungsten crystal was processed in the same way. Again, a delay difference between data with and without subtracted background could be observed. The deviations were not as strong in this case ranging from $-30\ as$ to $60\ as$, but still are larger than the standard deviation of the measurement. The study of possible dependencies for the W(100) crystal has been summarized in Figs. 5.13, 5.14 and 5.15, where the BG-subtraction independent values have been marked in blue again. As before, there is no dependence on the retrieved XUV pulse duration or on the NIR laser intensity (Fig. 5.13), while values for high intensity have still been neglected for the further analysis. In the plot of the relative delay against the TOF lens voltage (Fig. 5.14), no dependence could be identified with one exception at $475\ V$, where the average delays are slightly shifted by about $\approx 20\ as$ to higher values. In the same way as before, this deviation can be spotted in the day-to-day performance, where at three consecutive days measurements with this lens voltage have been conducted.
The time dependence for the W(100) crystal is shown on the right side of Fig. 5.15 plotting the sample exposure time against the streaking delay. Again, spectra acquired beyond 3 hours after flashing the sample give a shifted average delay. Consequently, these values have been excluded from the analysis as well.
Next, the relative delay was plotted against the NIR pulse duration (left side of Fig. 5.15). Now, a clear dependence of the pulse duration is observed, which can

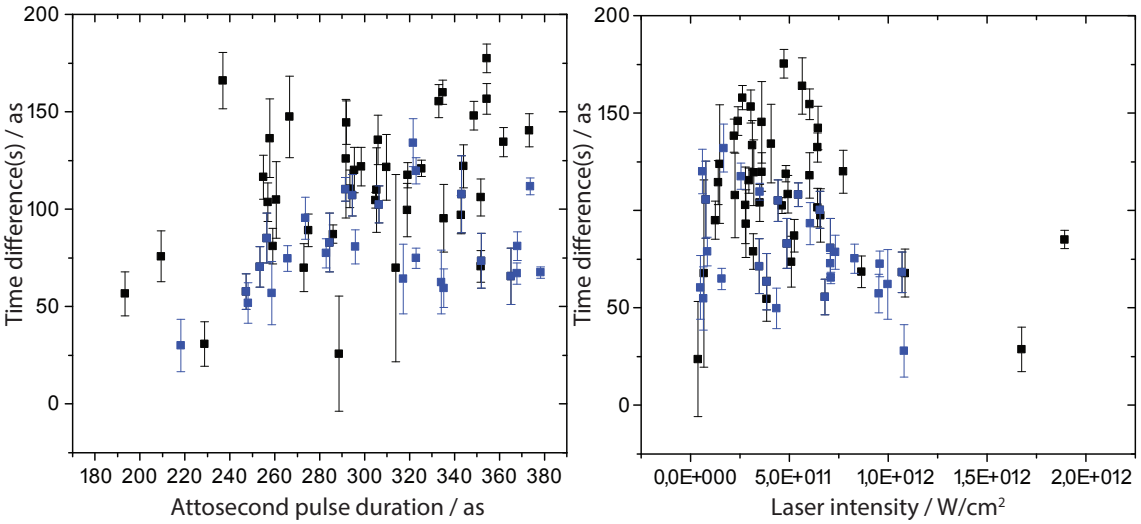

Figure 5.13.: Relative delay versus attosecond pulse duration and laser intensity for the W(100) crystal. Data points that have been found to be independent on the background subtraction are marked in blue.

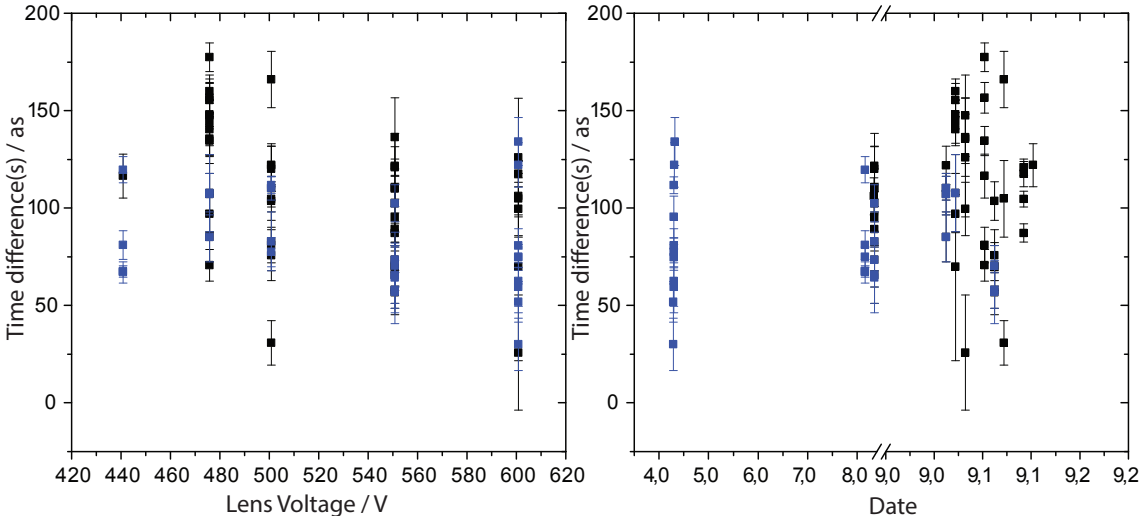

Figure 5.14.: Relative delay versus TOF lens voltage and day-to-day performance for the W(100) crystal. Data points independent of the background subtraction are marked in blue.

be traced back to background dependent effects under comparison with the blue-marked data points. Other reasons could be a different line shape behavior or an erroneous retrieval of the duration itself as discussed before.
Finally, Fig. 5.16 depicts the dependence of the relative delay on the wavepacket chirp. Again a large range of chirp values is covered, but the slope of the linear

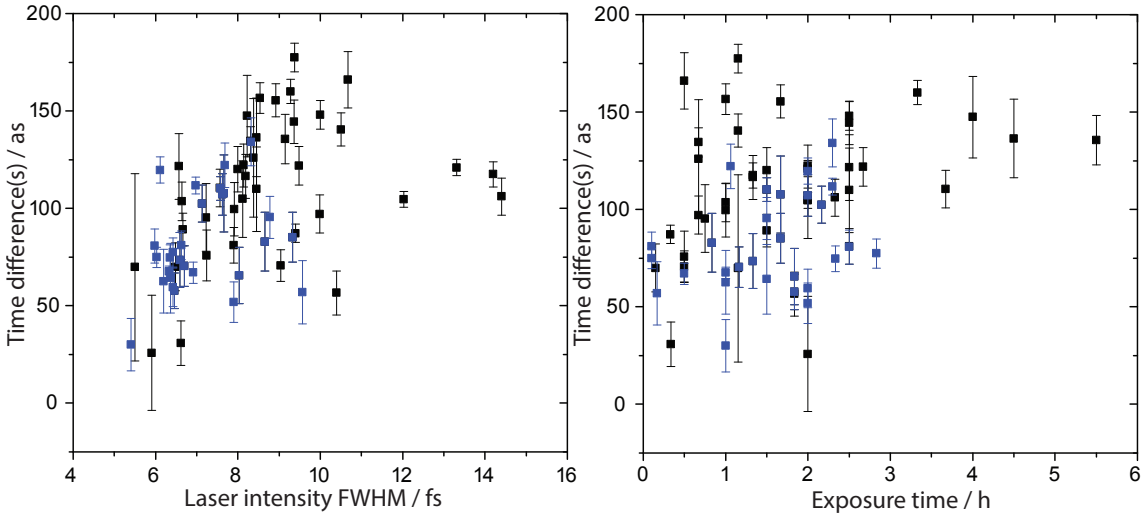

Figure 5.15.: Relative delay versus the NIR pulse duration and time after the last cleaning of the sample for the W(100) crystal. Data points independent of the background subtraction are marked in blue.

decrease in delay for increasing chirps above 10 fs^{-2} is now lower than for W(110). In other words, the dependence on the EWP chirp seems to be less strong for the W(100) crystal. For the W4f core level (bottom of Fig. 5.16) the dependence is even almost vanishing. For values below 10 fs^{-2} a linear dependence with a different sign of slope can be noticed as for the W(110) crystal. In the same way as has been done in the previous section, spectra without a dependence on the applied Shirley background subtraction have been separated and analyzed in further detail. The relative delay between CB and W 4f electrons is then retrieved as 69 ± 21 as with an average CB chirp of -4 ± 8 fs^{-2} and a W 4f chirp of -3 ± 4 fs^{-2}. The delay is rather close to the values retrieved from the W(110) crystal and, taking into account the relative difference between both delays of ≈ 30 as, is almost identical within the experimental uncertainties. However, the same argument as given in the previous section, concerning the existing chirp dependence, holds true. Therefore, a further discussion must include the chirp dependence (section 5.3.2). The attosecond pulse duration is retrieved as 303 ± 53 as, which is even smaller than the pulse duration measured before in the case of the W(110) crystal. Since this is mostly an effect of laser shot-to-shot fluctuations and the laser spatio-temporal profile, which spectrally broaden the overall measured peak, this smaller value cannot be traced back to a physical origin.

In order to evaluate the data further, the streaking spectra have been analyzed in detail for both crystal orientations. Different spectral line shape dependencies could be observed ranging from undistorted streaking spectrograms, adhering identical line widths in the field vector potential maxima, to rather modulated spectrograms,

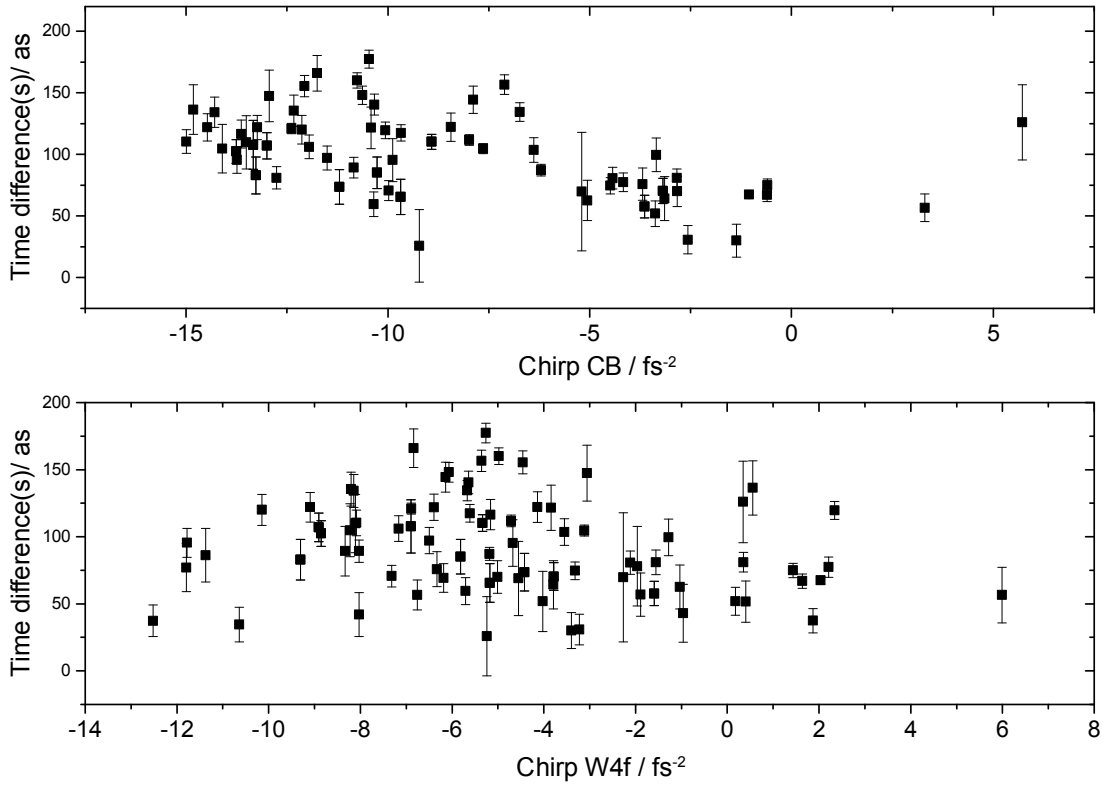

Figure 5.16.: Plot of the relative delay against the EWP pulse chirp as retrieved for the conduction band (top) and the W4f core level (bottom) for W(100).

which were washed out at the streaking amplitudes. The raw data of one streaking spectrogram with strong line shape variation can be seen in Fig. 5.17. The line shape distribution is narrow at one maximum of the field vector potential and develops to a very broad one at the opposite maximum. In the inset of Fig. 5.17 the spectra at these two points are shown. They have been shifted in energy so that the peaks coincide to allow for a better comparison. The spectral broadening of the peaks is notable. Such a periodical broadening and narrowing in the vector potential maxima can be explained by higher order chirp [69]. On the other hand, spectral line shape variations in the range of $1 - 2\ eV$ are predicted by Krasovskii [132] to occur around the vector potential maxima even for moderate exciting XUV pulse widths. The line width variations will be discussed in further detail in section 5.3.1.

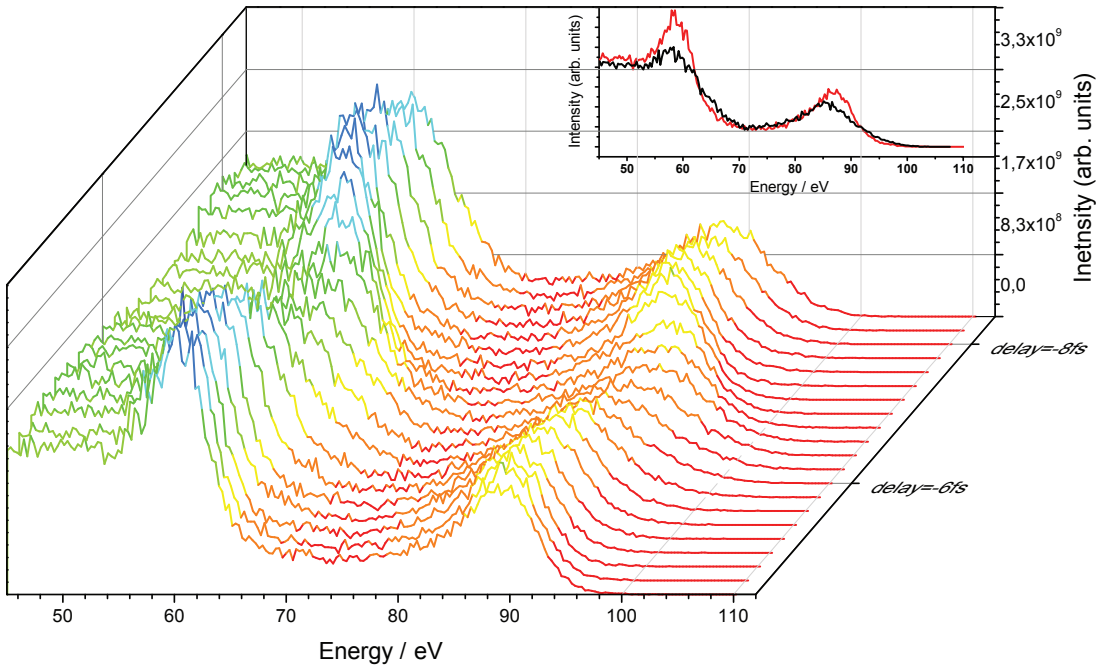

Figure 5.17.: Example of raw data of a streaking spectrogram with strong line shape variations. The inset shows PE spectra taken at the extrema of the streaking. They were shifted in energy to allow a better comparison.

5.2.3. Oxygen surface contamination

From various studies (e.g. [133, 134]), it is clearly known that surface contaminants are able to modify the surface properties. Their influence on the retrieved relative electron transport times has been discussed in detail by [31] for W(110). The relative delays were found to be shifted to higher values with increasing oxygen and CO coverage. For an oxygen contaminated surface this effect amounts to a shift in delay of up to approx. 30 as employing an excitation energy of 118 eV. As an explanation of the increased delays, two main contributions were identified: First of all, the shorter W-O-distance compared to the W-W-spacing and the electronegativity of oxygen, which tends to strongly modify the electron distribution, result in a valence charge distribution closer to the vacuum as would be the case without a layer of oxygen. The CB electrons, in average, therefore reach the surface at earlier times. Moreover, the different valence electron distribution also tends to shift the NIR-screening away from the first tungsten layer. Both effects tend to increase the relative delay between conduction and core electrons. The discussion has been made for the (110) orientation of tungsten. However, an increased delay cannot be a generalized

assumption for all orientations, as, for example, it is known that oxygen on W(100) can modify the electron distribution in such a way that the overall work function is decreasing, in contrast to what would be expected intuitively from an electronegative material [40]. Therefore, the change of delay under oxygen contamination has been measured in a small data series for our W(110) and W(100) samples applying the 92 eV mirror. The analysis for W(110) yields a modified relative delay of 125 ± 21 as. This results in an average deviation induced by oxygen contamination in the range of ≈ 27 as, which is in good agreement with the measurements of [31]. On W(100) the new relative delay is given by 116 ± 29 as and is thereby increased by a value of ≈ 47 as by the introduction of an additional oxygen contribution. It should be noted that the analysis is based on only a few data sets, so that an examination of a possible chirp dependence of the oxygen covered surface is not reasonable. Moreover, the retrieved chirp values are in doubt as the O 2p contribution arising within the conduction band peak could be misinterpreted as an additional chirp by the TDSE-algorithm. Nonetheless, the measured delays support the expectation of an increased relative delay under oxygen contamination. In this context, care has been taken throughout the measurements to maintain a clean surface as well as to limit the times between subsequent temperature flashes to minimize any effects due to oxygen adsorption. As discussed before, for a timeframe less than 3 hours after cleaning, oxygen adsorption is mostly negligible.

5.3. Correlation of chirp and delay in attosecond streaking measurements

In this section, it will be shown that chirp can deliver additional information about the system under observation and can be a more sensitive measure to electronic wavepacket modifications within the solid than the average wavepacket delay alone. Reliable information on the excitation pulse, the electronic transport and screening processes can yet only be derived from such attosecond streaking data, if detection and evaluation artifacts are identified and accounted for. Simulations indicate such artifacts for large chirp magnitudes and are given with a thorough analysis of the reliability range of the TDSE routine in section 5.3.1. Accounting for such artifacts, the measured correlation between the wave-packet chirp and relative time delay between conduction band and W4f core-level photoemission is further analyzed in section 5.3.2. Different sources of chirp such as electronic screening, band structure or localization induced effects are discussed. Yet, a major part of the chirp to delay dependency seems to stem from different slopes in the energy dependent atomic cross-sections of the 4f and 5d states of tungsten. A comparison with simulated data based on these cross-section variations is also given (Sec. 5.3.2).

5.3.1. Simulations

In order to identify possible detection and evaluation artifacts and gain further insight into the observed chirp dependence, calculations have been performed based on measured as well as simulated data. The latter were constructed from a vector potential, which was created as a solution of the time dependent Schrödinger equation.

Fast Fourier Transformation (FFT)

As described in the supplement of [17], a Fast Fourier Transformation (FFT) was conducted to probe the influence of the Shirley background on the streaked photoelectron spectra. The 3-dimensional photoelectron spectrum $P(\epsilon, \tau)$ gives the measured intensity as a function of the electron kinetic energy ϵ and the delay τ between the XUV-pump and NIR-probe pulse. As part of the FFT the delay τ is converted to a frequency ω, so that the appearance of each frequency over the energy ϵ can be monitored. Particularly, the energy components, which are modified with the laser frequency ω_L, have been picked out and investigated. This gives a plot of intensity against energy for the specific frequency ω_L (Figs. 5.18, 5.19 and 5.20). Here, exemplary spectra, where the CB-W4f relative delay is not influenced by the background subtraction (Fig. 5.18), and spectra, which show a significant change in the CB-W 4f delay (Fig. 5.19 5.20), were analyzed.
Fig. 5.18 shows a spectrum with a rather low background intensity (top left). As could be expected, the background subtraction (top right) influences neither the spectral line shape nor the retrieved relative delay. The corresponding FFTs (bottom left and right) thus show only minor differences before and after background subtraction. The highest intensity in the FFT spectrum emerges at energies where the intensity slope in the original spectrum is maximal or in other words, it emerges for those energies, where the modulation of the intensity with the particular laser frequency is maximal. In this manner, a double peak structure arises in the FFT. For the optimal (simulated) case, the two peaks of each double peak are equally weighted according to their intensity after background subtraction. The Fourier transform of a simulated spectrogram with included Shirley-background leads to an attenuation of the lower energy peak and conversely a raise of the high energy peak as a result of the asymmetric intensity contribution of the Shirley background. The streaking from Fig. 5.18 does not reflect this behavior, which is most probably a result of a different line width behavior at the streaking extrema as will be discussed in the next section.
In Figs. 5.19 and 5.20, the background intensity is now larger relative to the peak intensity as can be seen in the upper spectra. A modification of the streaking due

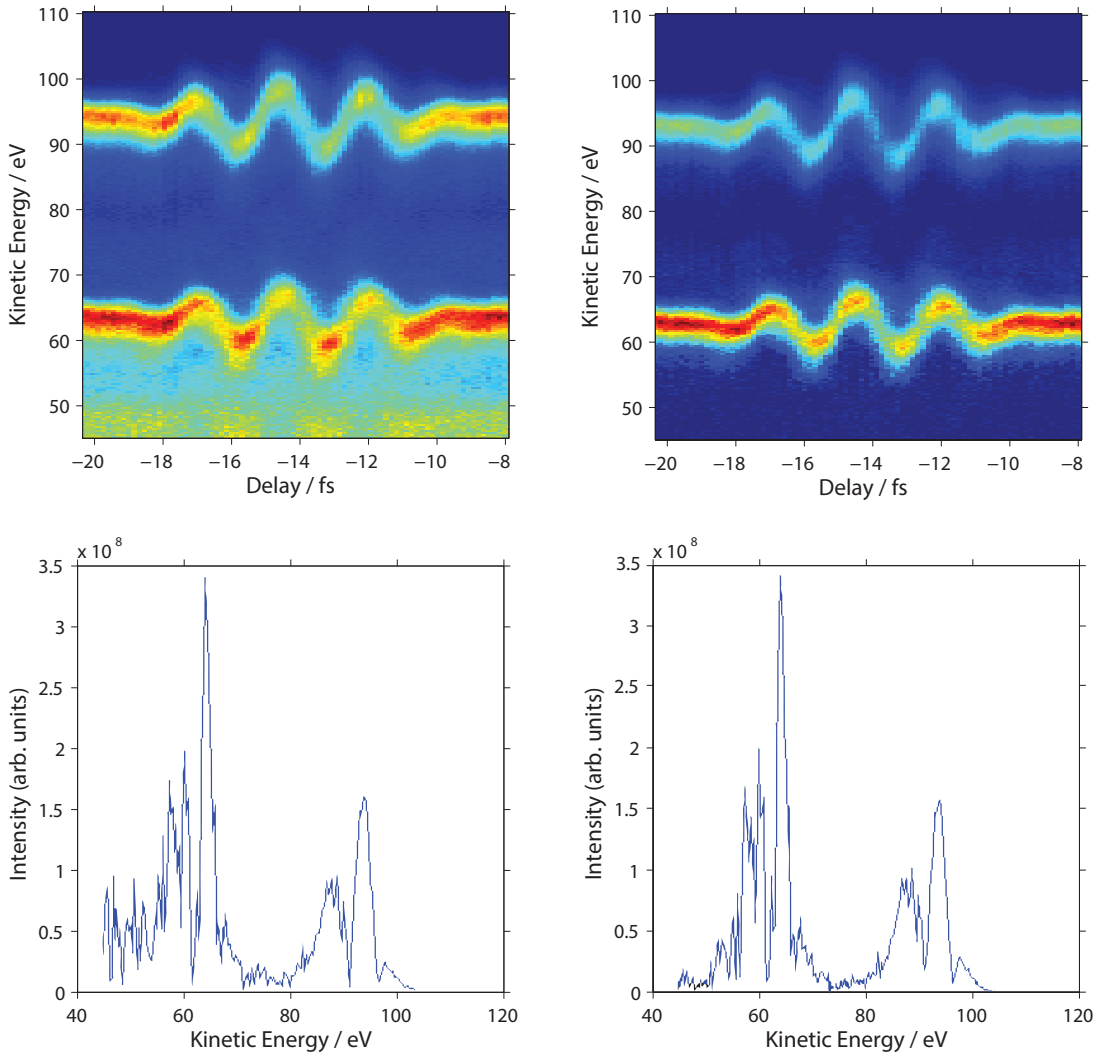

Figure 5.18.: The top figures show the measured photoelectron spectra $P(\epsilon, \tau)$ with (top right) and without (top left) background subtraction. In the bottom figures the corresponding FFT plots are depicted. They show the occurrence of each energy that is modulated with the laser frequency ω_L along the delay.

to the background seems to preserve especially at lower energies, where the background is dominating. This matches the simulated (theoretical) case. However, also the case of a raise of the lower energy peak 5.19 is observed. This could point towards problems of the background separation from the streaking spectrogram. Yet, no distinct relation between the FFT-spectra and background related modifications could be linked and the occurrence of possible spectral line shape variations [132] further complicates the interpretation. In order to evaluate this further, simulated

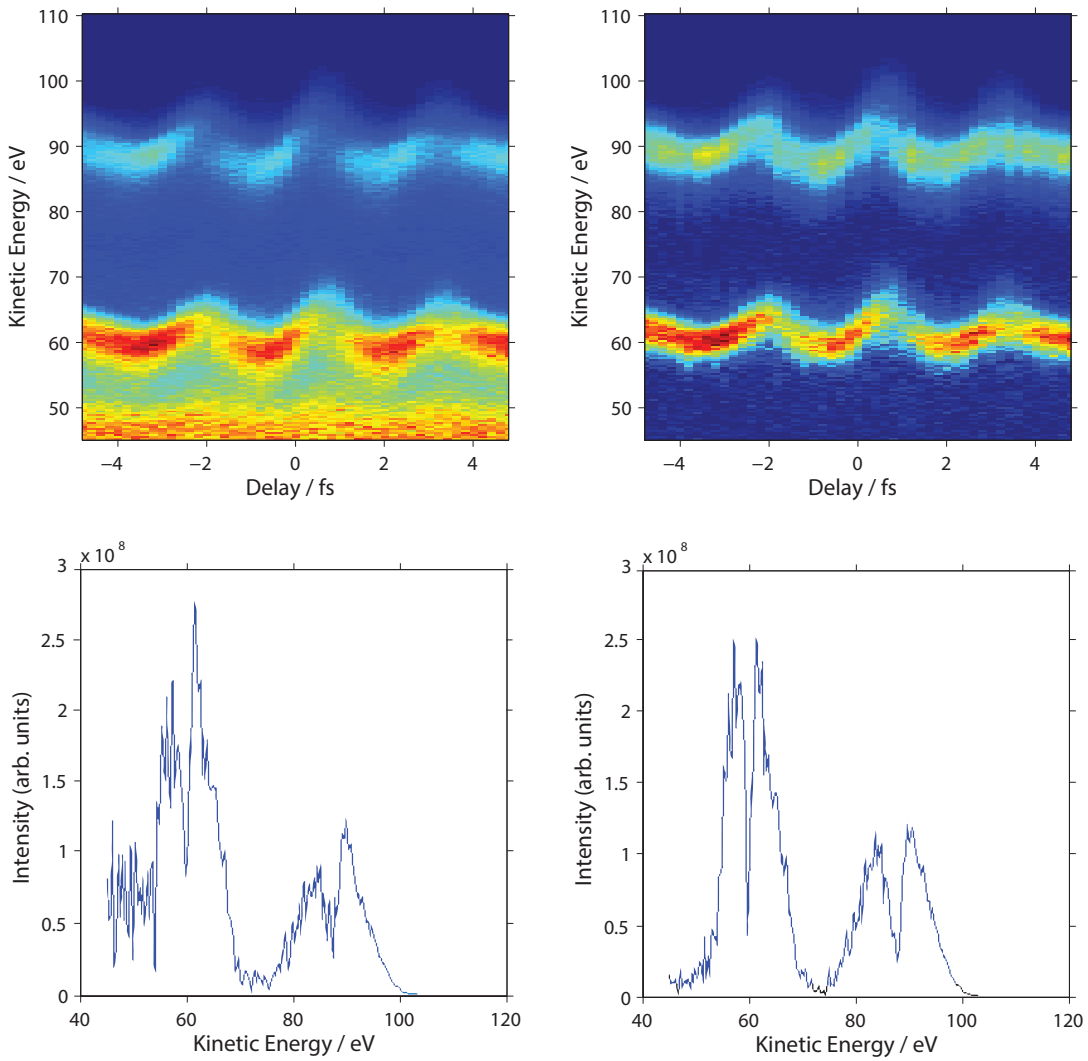

Figure 5.19.: The top figures show the measured photoelectron spectra $P(\epsilon, \tau)$ with (top right) and without (top left) background subtraction. In the bottom figures the corresponding FFT plots are depicted. They show the occurrence of each energy that is modulated with the laser frequency ω_L along the delay.

data have been produced under different conditions and subsequently analyzed.

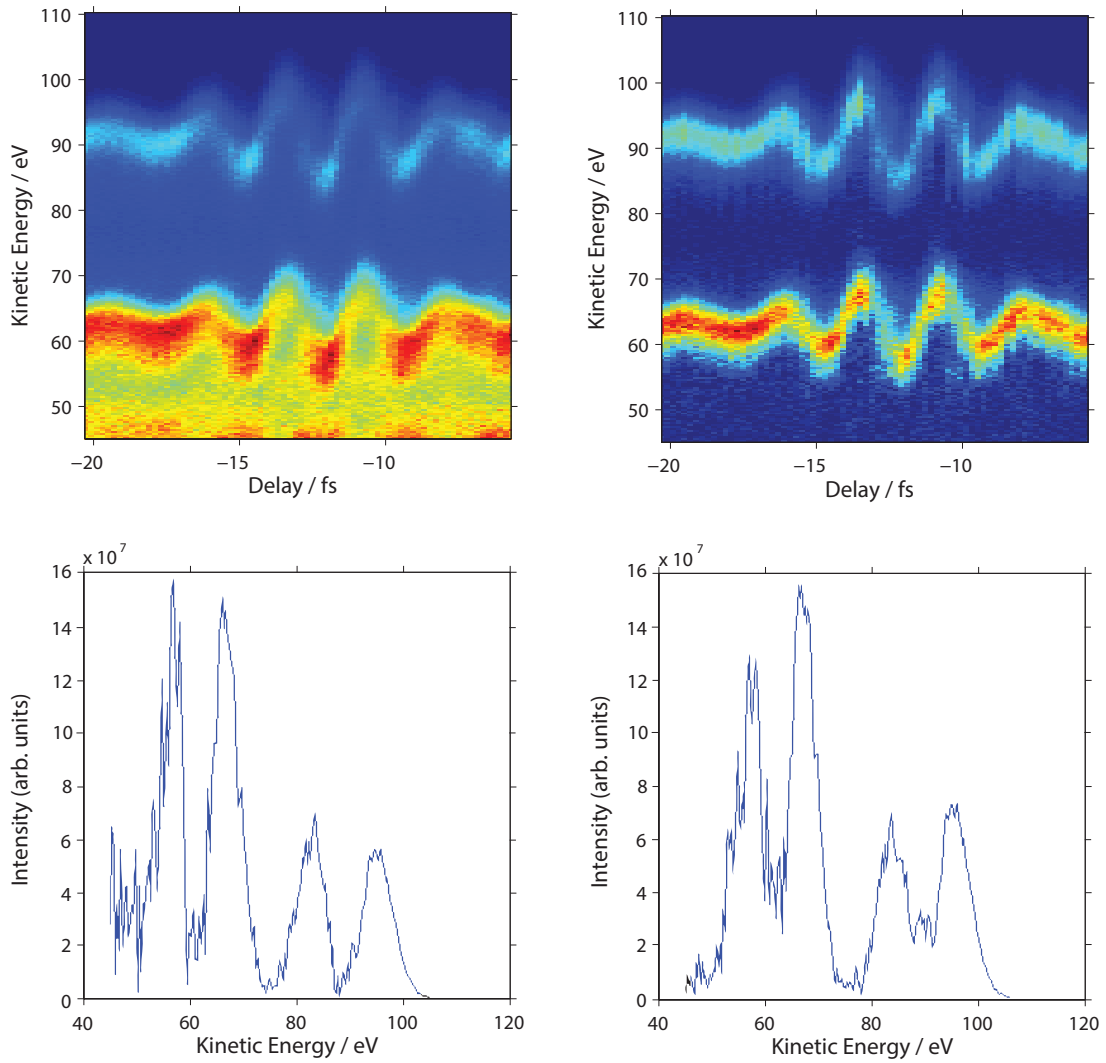

Figure 5.20.: The top figures show the measured photoelectron spectra $P(\epsilon, \tau)$ with (top right) and without (top left) background subtraction. In the bottom figures the corresponding FFT plots are depicted. They show the occurrence of each energy that is modulated with the laser frequency ω_L along the delay.

TDSE Simulations

Simulated data can be constructed by using mostly the same algorithm that has been used in the TDSE retrieval. Originally, spectra are created as a solution of the time dependent Schrödinger equation and fitted to the real data by a least-squares algorithm. By canceling the last step and specifying the NIR and XUV pulse

parameters as initial values, simulated data can be created. This way, simulated streaking spectrograms with different initial XUV spectral pulse widths and chirps have been created and subsequently processed in the same way as real data, including the subtraction of the Shirley background. The initial background of the simulated data was produced by calculating the "inverse" Shirley according to

$$BG_i = e \cdot \int_i^{E_{max}} I(E)\, dE \quad , \tag{5.11}$$

giving the background value BG for every energy point i with E_{max} as the maximum energy of the region of interest. The factor e scales the intensity of the background. It was chosen to fit best with the background intensity of our measured data, which in our case gave a factor of $e = 0.08$.
It should be noted that in our simulations the EWP is generated as an exact copy of the incident XUV-pulse[2] that is scaled with the photoionization cross-sections, implying that most pulse parameters, in particular the EWP- and XUV-chirp, stay equal.
Fig. 5.21 shows the retrieved FHWM of the W4f peak plotted against the XUV-NIR pulse delay for simulated data with different initial parameters. The retrieved values for the FWHM are derived from a fit of a Gaussian to each peak of the spectra after background subtraction. For a better understanding the COE peak shift is plotted in the bottom of the figure. The energy axis depicts $\omega - \omega_0$ in this case, where ω_0 is the central energy.
At an initial XUV pulse width of 500 as, the periodical broadening of the spectral width for an unchirped pulse is rather small (less than 1 eV). The maximal broadening occurs at the zero crossings of the energy shift curve resp. the vector potential. As soon as a chirp is introduced in the initial exciting pulse, the known periodical broadening and narrowing of the pulse width in the zero crossings of the vector potential can be observed. The pulse width is varying from a minimal value of ≈ 4 eV to a maximum of ≈ 10 eV. An increase of the initial XUV pulse width leads to an enhancement of the broadening (to approx. 12 eV for a pulse width of 600 as), while the narrowing stays mostly unaffected. Another set of simulations was also performed with a background scheme dubbed fixed Shirley (FS) to simulate the influence of an unstreaked background. Here, a Shirley background is calculated for the first delay values of the spectrogram and subsequently added to all spectra. This procedure does not introduce significant changes for an unchirped 500 as XUV pulse, but for a chirped pulse a FS contribution leads to a modification of the line width behavior as can be seen in Fig. 5.21. The modification is strongest in the zero crossings and can thus (slightly) change the retrieved linear chirp, which is dominant in these points. Additionally, chirped pulses with larger pulse width

[2]While in reality additional modifications of the EWP can be present as a result of e.g. the interaction with the solids bandstructure.

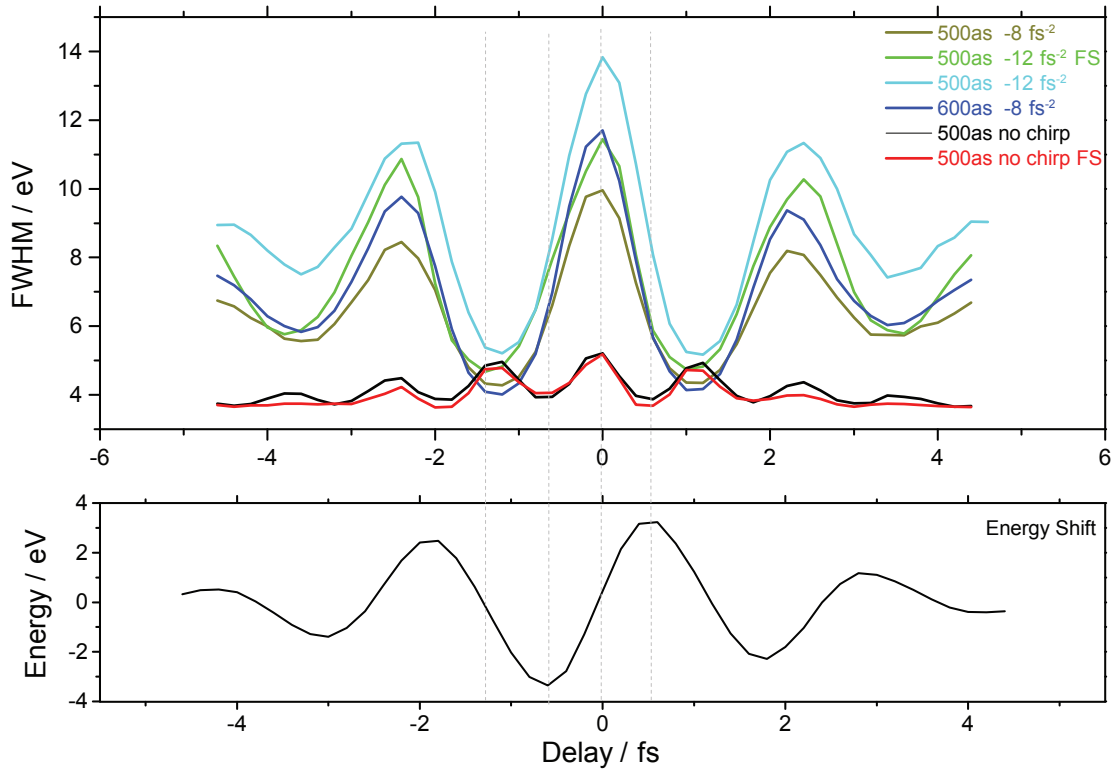

Figure 5.21.: FWHM plotted against the pump-probe delay for simulated data of different initial parameters. In the bottom of the figure the energy shift is given for comparison. The central energy ω_0 has been subtracted giving $\omega - \omega_0$ as the plotted value.

or under the assumption of an unstreaked background (FS) were also observed to give an asymmetric tail in the peaks after subtraction of the background. All these points can reflect a small error in the delay, but it should be noted that the TDSE retrieval algorithm is taking into account the whole spectrogram in a least-squares fit. This sort of averaging should minimize the influence of these errors.
Fig. 5.22 shows, as an example, the FWHM for one real data spectrogram.The minimal and maximal electron pulse widths are now $\approx 6\ eV$ and $\approx 12\ eV$, respectively. The overall broadening, which exceeds the supported mirror-bandwidth ($3.5\ eV$), is a result of spectral smearing as a result of shot-to-shot fluctuations of the laser, finite TOF- spectrometer resolution and space charge effects (discussed in Sec. 5.2.1). A periodic behavior is present as in the simulated data, but the characteristics of the FWHM are now inherently different. Starting with the zero crossings of the vector potential, the FWHM still shows the periodic broadening and narrowing of the pulse width, nonetheless the strongest broadening or narrowing is developed close-by the vector field extrema. These properties have been predicted by Krasovskii [132] for

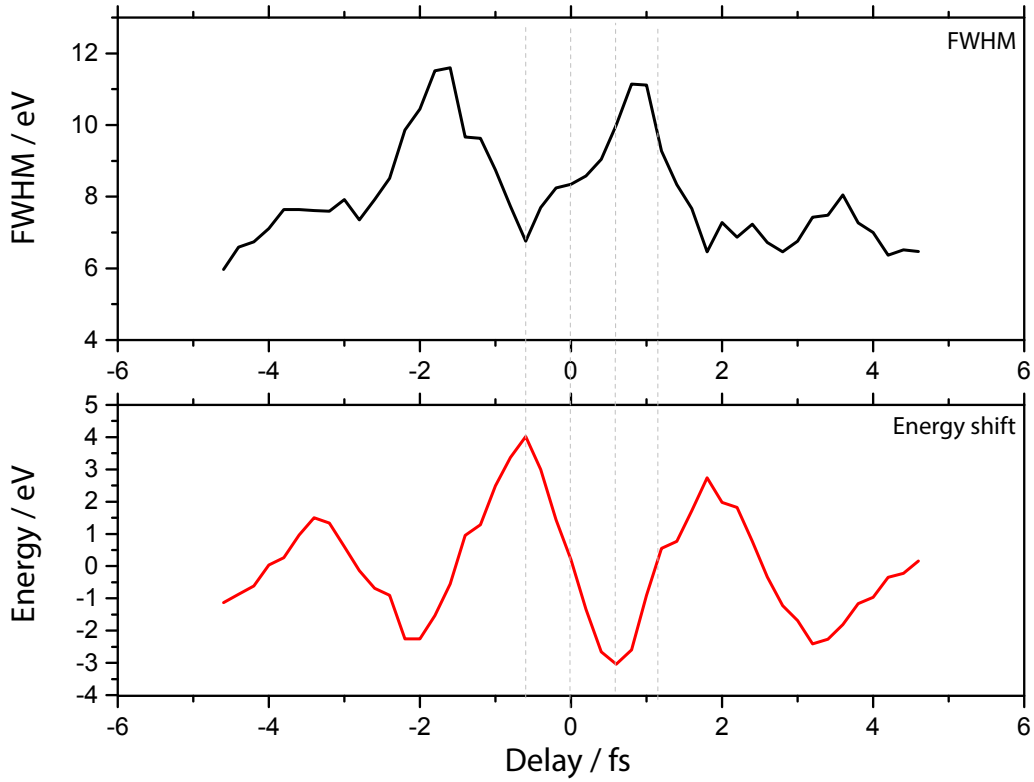

Figure 5.22.: FWHM plotted against the pump-probe delay for exemplary real data. In the bottom of the figure the energy shift is given for comparison. The central energy ω_0 has been subtracted giving $\omega - \omega_0$ as the plotted value.

large XUV pulse widths. Thus, a combination of the effects seen in our simulated data for large pulse widths or an unstreaked background, in addition to the results of Krasovskii, are able to reproduce the characteristics of the real data.
Next, the changes in the COE shift (as a projection of the laser vector potential) based on different initial parameters are investigated for the simulated data. The shifts were derived from a Gaussian fit to each peak of the spectra and a calculation of the COE peak positions. At first, the energy shift of the W4f peak is analyzed (Fig. 5.23) for a constant pulse FWHM of 600 as. The plot shows a modification of the streaking amplitude upon a decrease of the chirp to $-12\ fs^{-2}$, which would lead to an overestimation of the laser intensity. The other parameters mostly stay fixed. In the inset of Fig. 5.23 a magnified area around the zero crossing of the vector potential is shown. The difference between the energy shift curve of the chirped pulse in comparison to the unchirped one is rather small at approx. 21 fs. Introduction of an unstreaked background (FS) leads to a bigger deviation in the crossing at around 44 fs. Also the streaking itself is asymmetrically deformed, so that the streaking

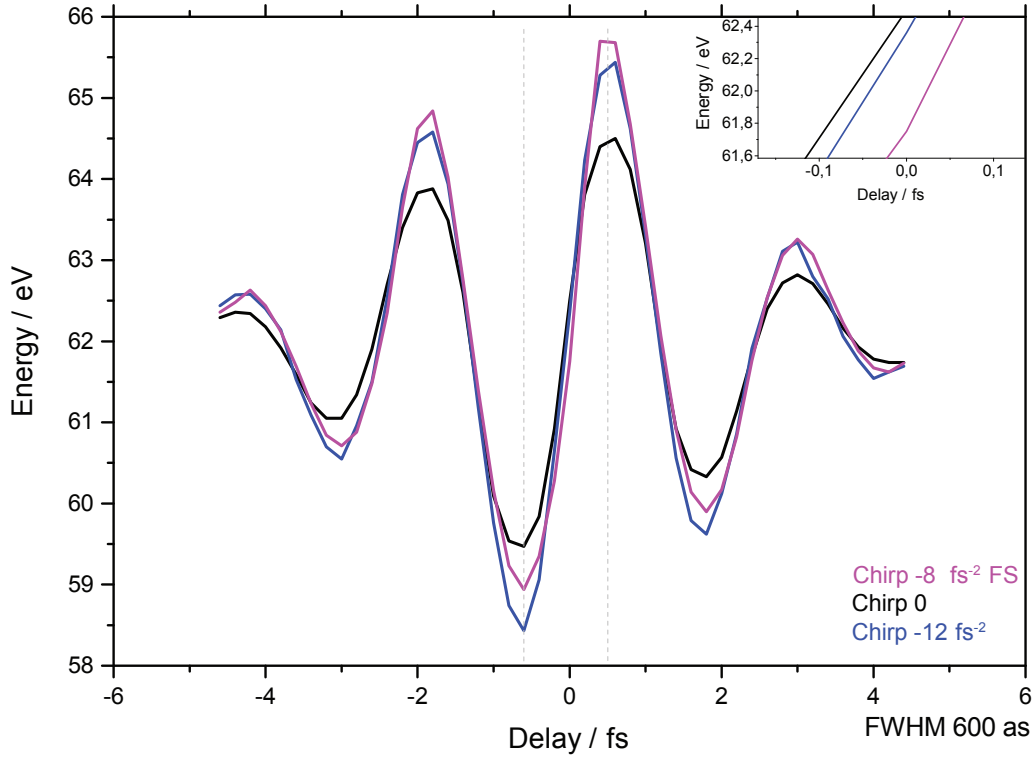

Figure 5.23.: Energy shift of the W4f peak plotted against the pump-probe delay for simulated data. The inset of the figure shows an enlarged area close-by the zero crossing of the vector potential.

amplitude is diminished for one extrema and enhanced for the following one.
Examining the simulated CB peak data, the energy shift curve (COE), however, shows larger deviations from the unchirped case (Fig. 5.24). As before, an increase in the streaking amplitude can still be observed upon decrease of the chirp, but now the streaking experiences an additional asymmetric shift across the delay. This gives a zero crossing shift of the streaking at $-12\ fs^{-2}$ in relation to the curve of the unchirped pulse in the range of $\approx 140\ as$. This rather large shift can, in combination with the shift of the W4f peak (which is shifted in a different direction), establish an artificial delay.
The curve retrieved from the fixed Shirley calculation is less affected than the chirped pulse curve. It shows a similar behavior as for the W 4f peak concerning the streaking amplitudes. Still the shift in the zero crossing is rather large at $\approx 70\ as$. Thus, such a background contribution also involves a modification of the retrieved delay.
As noted before, the TDSE retrieval algorithm is taking into account the complete spectrogram as part of the fitting in contrast to simply comparing the delay between the streaking curves of the W4f and CB at the zero crossings. Anyhow, it has al-

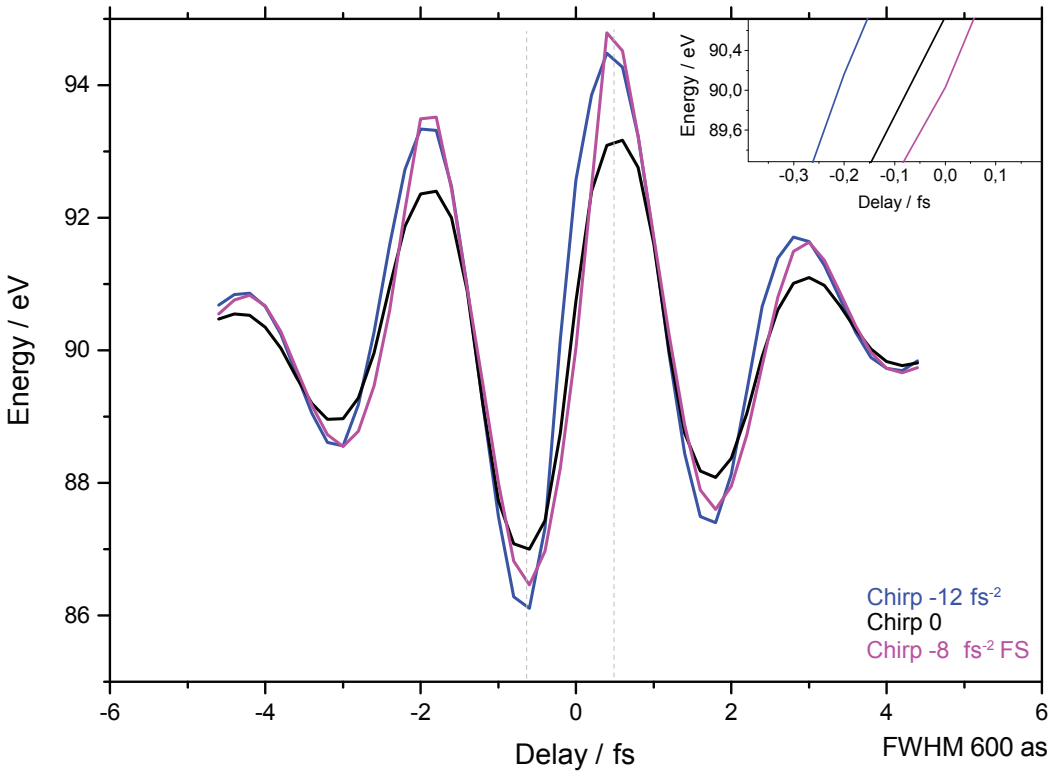

Figure 5.24.: Energy shift of the CB peak plotted against the pump-probe delay for simulated data. The inset of the figure shows an enlarged area close-by the zero crossing of the vector potential.

ready been observed before that asymmetries in the shape of the energy shift curve can lead to substantial delays in combination with an XUV chirp [31]. In this case, the asymmetries have been produced by neglecting the transmission function of the TOF detector. Consequently, an artificial delay as a result of the asymmetric shift and the XUV chirp can also be expected in our case. In particular, it seems that a strong mixing of a spectral peak with the background for large chirps leads to errors in the separation of both as part of the background subtraction. Thus, as seen in our simulations, the pulse width is enhanced for larger initial pulse widths especially in the vector field zero crossings and, in the same way, also the energy shift is largest for those pulse widths, particularly close to the zero crossings. Interestingly, as a result of this pulse width broadening effect in the zero crossings, the relative intensity of the photoemission peaks compared to the background is minimal resp. the influence of the background is maximal in these points.

Finally, the simulated data sets were passed through the TDSE retrieval algorithm to calculate the expected deviations in the retrieved delay evolving in dependence

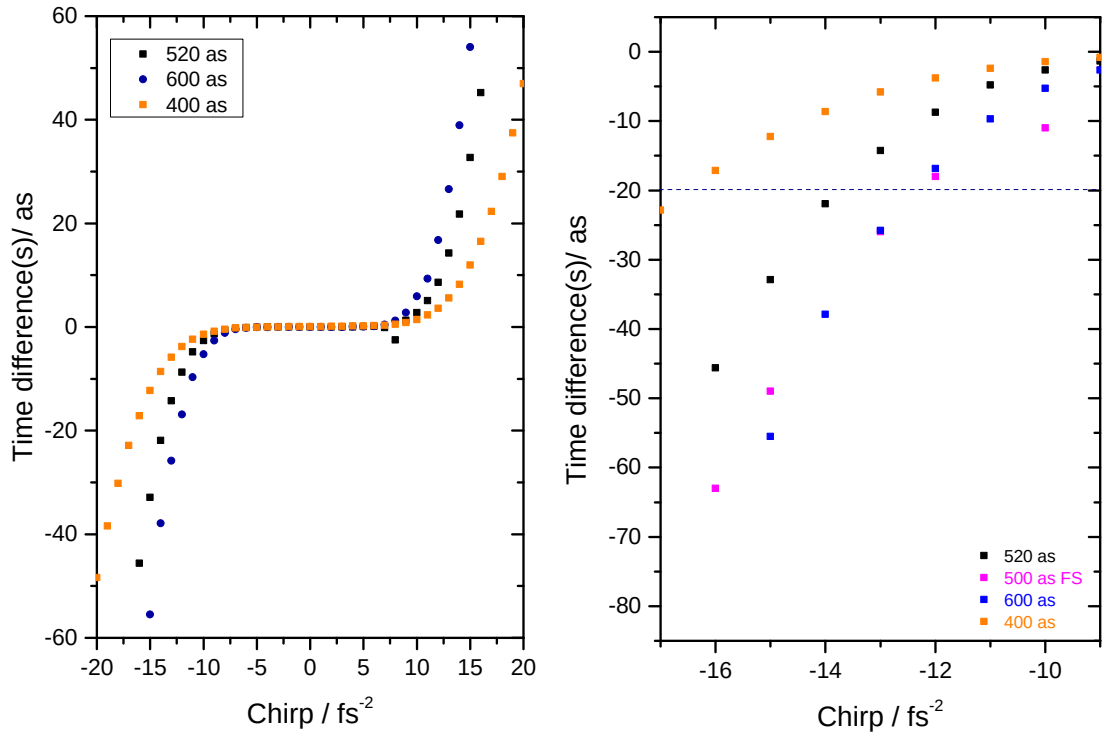

Figure 5.25.: Retrieved delay between the CB and W4f of the TDSE algorithm as a function of initial XUV pulse chirp for simulated data of different inital pulse widths. The initial delay of CB and W4f is exactly zero. The background had been subtracted. The right side gives a zoomed in version for large negative chirps.

of the XUV-chirp as a result of an incomplete background subtraction. The actual delay between the simulated CB and W4f wavepackets is set to zero. This way, any delay retrieved by the TDSE algorithm is characteristic of an artificial delay as a result of, e.g., the background mixing effect. The obtained relative CB-W4f delays are plotted in 5.25 against the initial XUV chirp. The background has been subtracted before running the retrieval algorithm. The simulations have been performed for the same XUV-/NIR- parameters present in our experiments and for different initial wavepacket pulse widths, beginning with the experimentally retrieved (and certainly underestimated, see 5.2.1) average wavepacket duration of 400 as. For large (negative) chirps, all curves show the evolution of an artificial delay. The retrieved curves in each case strictly depend on the sign and magnitude of the XUV-chirp and resemble a third order polynomial. At a pulse width of 400 as, notable delays can be observed for chirp magnitudes larger than 15 fs^{-2}. For an initial pulse width of 520 as (black points) the increase is so rapid that the artificial delay exceeds the

standard deviation error of our measurements already at a chirp of $-14\frac{1}{fs^2}$. However, it can be noticed that the delay-chirp dependence offers a rather large plateau between approx. $-10\ fs^{-2}$ and $10\ fs^{-2}$, where no apparent influence of the delay is observed. Therefore, it is certainly reasonable to routinely restrict the analysis to data points within this range.
Inclusion of a fixed Shirley background for a pulse width of 500 as (magenta points) tends to shift the curve downwards in the range of negative chirps meaning an increased divergent delay. Now, the artificial delay exceeds the standard deviation error already at $-12\frac{1}{fs^2}$. For an increased pulse width of 600 as with a streaked background (blue points), a curve with a larger slope is formed, starting at the same values as for a pulse width of 520 as, but rising quickly to the by far largest deviations.
It is important to note that the XUV-chirps of the simulated data as retrieved by the TDSE algorithm always agree with or overestimate (by at most 1 fs^{-2}) the specified chirp. This way, a comparison with the experiment is possible.

The TDSE retrieval has also been performed on simulated spectra, where the background has not been subtracted (Fig. 5.26). Here, the shape of the curve is similar and the retrieved delay is, in the same way, strictly dependent on the sign and magnitude of the chirp. However, the sign of the retrieved delay is different. Thus, in comparison of the retrieved delay of spectra before and after background subtraction, the artificial delays add up and can reflect in principle the deviations between raw and background-subtracted real data sets, at least for large chirps. It should be noted that the dependence on the chirp is much weaker for spectra with background included as can be seen in 5.26. The deviation in delay is in any case smaller than the average standard deviation error of a measurement. Also the spectra are not affected by adding a fixed Shirley background so that the delay constantly stays at zero in this case. As seen before, a larger initial pulse width of 600 as increases the slope of the curve for larger (positive or negative) chirps and consequently, retrieves larger artificial delays.
The deviation in delay is to a certain extent dependent on the weighting of the Shirley background compared to the overall intensity. As noted before, the general scaling factor is set to $e = 0.08$. By increasing it to $e = 0.30$, the diverging delay is increased as well, giving the magenta curve in Fig. 5.26. The increase is small though, compared to the large raise of the background scaling factor e.
Apart from this, the artificial delay depends also on the streaking amplitude of the NIR-field. One can say that a decrease of the streaking amplitude by a factor of 2 approximately doubles the deviation in delay. For the background subtracted case, the constant-delay plateau generally stays unaffected from such modifications.

In summary, for background subtracted spectra trustable values can be found in the range of $-10\ fs^{-2}$ to $10\ fs^{-2}$. Spectra without applied background subtraction are

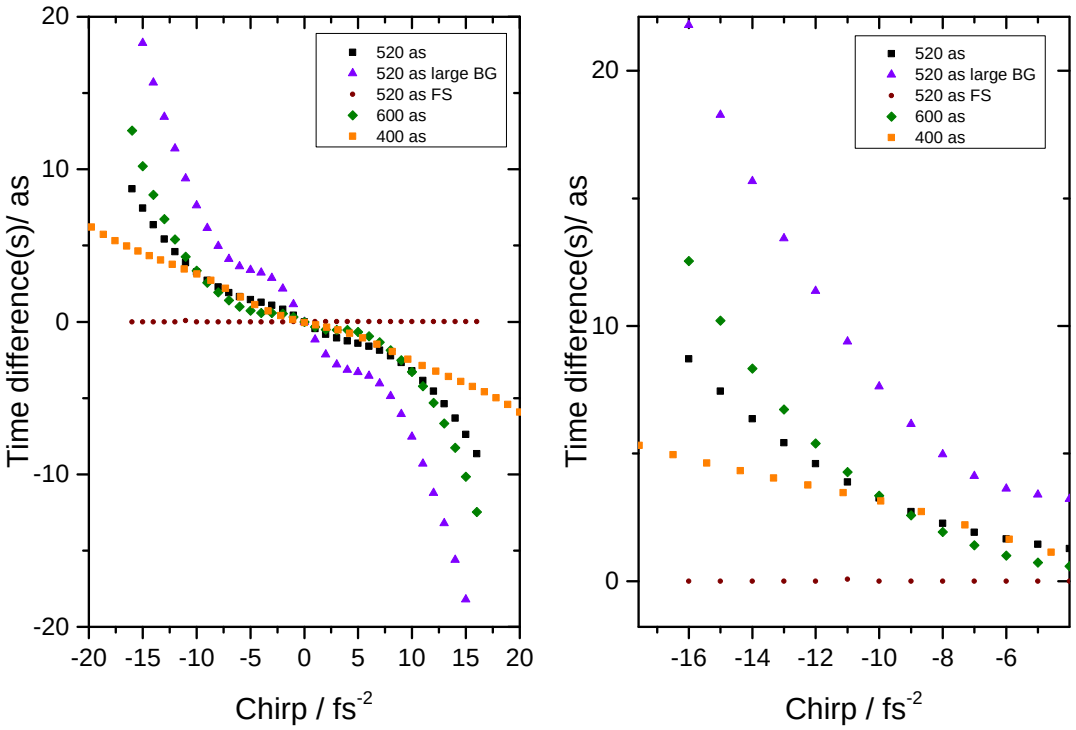

Figure 5.26.: Retrieved delay between the CB and W4f of the TDSE algorithm as a function of initial XUV pulse chirp for simulated data of different initial pulse widths. The initial delay of CB and W4f is exactly zero. The background was not subtracted and is included in all data. The right side gives a zoomed in version for large negative chirps.

less susceptible to this effect and give reliable values between $-12\ fs^{-2}$ to $12\ fs^{-2}$.

5.3.2. Results and discussion

With the range of trustable values in mind, one can have a closer look at the chirp dependence of the spectra. Fig. 5.27 shows the retrieved streaking delay plotted against the wavepacket chirp for the W(100) (left side) and the W(110) crystal (right side) for background subtracted spectra. In order to enable an unambiguous interpretation of the data, as before only those spectra have been included in the plot that do not retrieve different delays with and without background subtraction within the standard error. One can see that for each crystal orientation the conduction band electrons as well as the W 4f electrons depict a primarily linear

dependence against the chirp for values above $-10\ fs^{-2}$. Below this point the spectra obviously deviate from this behavior and show an essentially decreasing delay for larger (negative) chirp. This behavior can most probably be related to the erroneous retrieval discussed before, which tends to appear for large values of the chirp modulus. Therefore, only values in the trustable range above $-10\ fs^{-2}$ have been taken into account for the analysis. In this case, a linear trend can be observed in each plot.
The general spread of the measured CB-W 4f time differences is rather large for a given EWP chirp as is usual for most of the attosecond streaking measurements

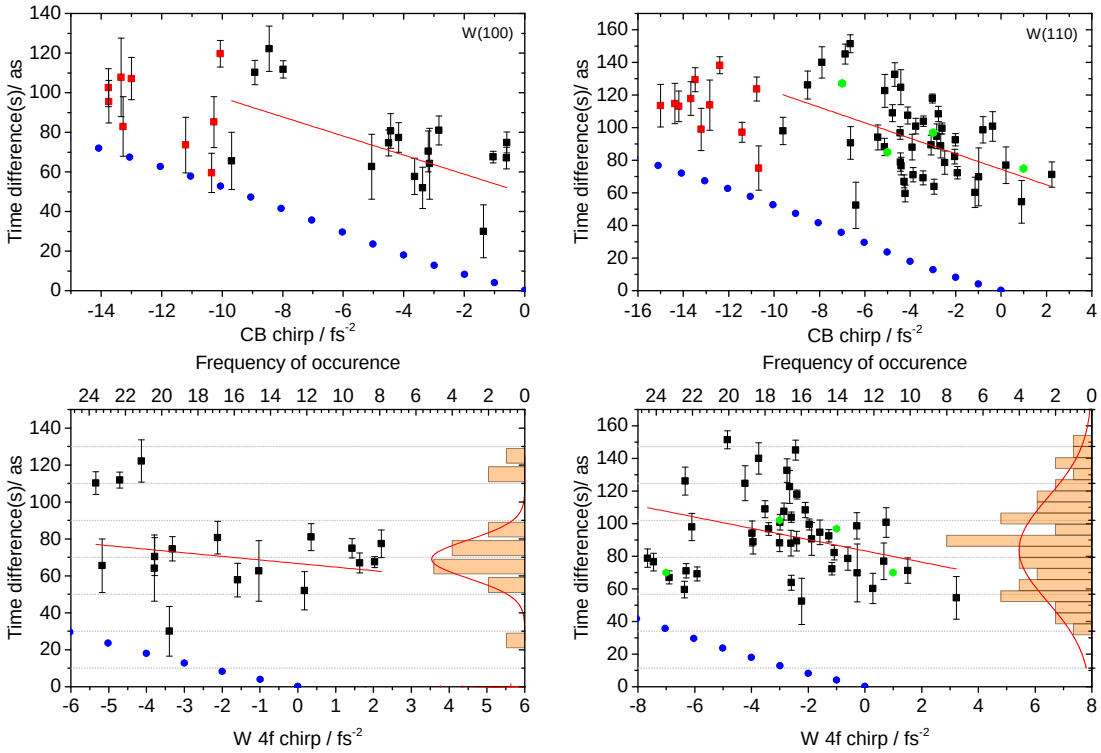

Figure 5.27.: Chirp dependence of spectra not affected by background mixing plotted as streaking delay against EWP-chirp for the CB (top) / W 4f electrons (bottom) and the W(100) (left) / W(110) (right) surface. The linear interpolation of the data is given by the red curve in each spectrum. The frequency of occurrence of each delay at the bottom plots resembles well to a Gaussian plot as indicated by the red line fit. Green points give the centers of Gaussians, evaluated in chirp windows of 2 fs^{-2}. The blue points give the chirp dependence retrieved from simulated data under inclusion of the atomic cross-sections of the 4f and 5d state (see p. 113).

performed so far [31, 30], where shot-to-shot fluctuations and spatial jitter of the laser modify parameters of the incident XUV/NIR-pulses (e.g. the XUV photon energy) and reflect in a measured Gaussian spread of the relative delays. In this manner, a statistical (Gaussian) distribution of the overall data is apparent, which generally allows to derive the average values of the delays.
In order to follow the arising dependence on the chirp, a linear interpolation has been conducted on the plots from 5.27 and its results are summarized in table 5.1. It can be seen that the interpolation of the conduction band plots gives the same slopes for the (100) and (110) orientations. A rather interesting behavior comes from the diminished slope of the W 4f- compared to the CB-linear dependence, which is found for both crystal orientations leading to an almost vanishing CB-chirp dependence for W(100). The y-intercepts for W(110) are slightly larger than for W(100), reflecting the generally lower average retrieved streaking delay for the W(100) surface.
It should be noted that the retrieved chirp is the overall chirp of the emitted electron wavepacket, while the chirp of the pump XUV-pulse is unknown. It is known that a chirp present in the XUV-field is mapped onto the emitted electron wavepacket 2.4. However, the emergence of a possible CB or W 4f final state dependent chirp cannot be separated from this initial chirp in our setup.
A cross-check of the retrieved chirp dependency could be achieved with a robust routine introduced by Gagnon et al. [135], calculating the average group delay dispersion(GDD) of the measured electron wavepacket, independent on its waveform. Plots, combining these newly retrieved GDDs with the time differences retrieved from our TDSE routine, give the same linear trend as the TDSE-only data sets.
The larger W(110) data set allows to divide the plot into several single sets, each covering a chirp window of 2 fs^{-2}. Considering the frequency of occurrence of the delays in these windows, allows to fit each with a Gaussian distribution. The centers of these Gaussians are given as green points in Fig. 5.27, which fit well with the linear fit of the overall data (red line). A larger deviation can only be spotted for one point on W(110) for a very low chirp, which could be a result of the weaker statistics present in this region.
A clear derivation of values from the given two dimensional plots seems difficult, since both chirp values, the CB- and W 4f-chirp, are given in relation to the relative temporal delay between the CB and W 4f peak. The inclusion of a three dimensional plot is necessary to decorrelate these values, which has been performed in Fig. 5.28. In the next step a plane was fitted by a least-squares routine to the 3 dimensional data points so that it is now possible to extrapolate the expected temporal delay for any given set of CB-/W 4f- chirp values. The retrieved plane for each crystal surface, (110) and (100), can then be written in terms of the equations

$$\Delta\tau^{(110)} = -7.4 \cdot b_{CB} \cdot (as \cdot fs^2) + 3.5 \cdot b_{W4f} \cdot (as \cdot fs^2) + 75.7\ as \tag{5.12}$$

$$\Delta\tau^{(100)} = -5.3 \cdot b_{CB} \cdot (as \cdot fs^2) + 3 \cdot b_{W4f} \cdot (as \cdot fs^2) + 55.3\ as\ , \tag{5.13}$$

where b_{CB} and b_{W4f} are the CB and W 4f chirp (in fs^{-2}). With this equation it is possible to calculate back to a "chirp free" delay denoting the measurement of a wavepacket with zero chirp. In case the origin of the relative wavepacket delay is a final state/propagation effect, the retrieved zero-chirp value reflects the "true" delay of a measured "non-chirped" electron wavepacket, which is not modified by peak modifications induced by group velocity dispersion. An additional temporal shift as well as a wavepacket chirp can then be the result of group velocity dispersion induced by the band's energy dispersion:

$$GVD = \frac{\partial}{\partial E}\left(\frac{\hbar^2}{\partial E/\partial k}\right) . \tag{5.14}$$

In particular, the peak form and center is modified as part of the induced GVD resulting in an average temporal shift of the wavepacket.
The "chirp-free" temporal delay can be calculated back to a value of $\Delta\tau_0^{(110)} = 76\ as$ for the (110) orientation and $\Delta\tau_0^{(100)} = 55\ as$ for the (100) orientation. The deviation between these two values is rather small and is, with a difference of approx. 21 as, within the standard deviations of 21 as (100) or 25 as (110) of the averaged delays. The value of $\Delta\tau^{(110)}$ agrees well with previous measurements, giving an average delay of 55 as taken from 4 individual spectrograms at negligible EWP chirp [31]. Inclusion of a decent chirp of $-6\ fs^{-2}$ raises the overall delay up to $\Delta\tau_{-6}^{(110)} = 99\ as$ for W(110), which denotes a deviation from the chirp-free value of 24 as, already in the range of

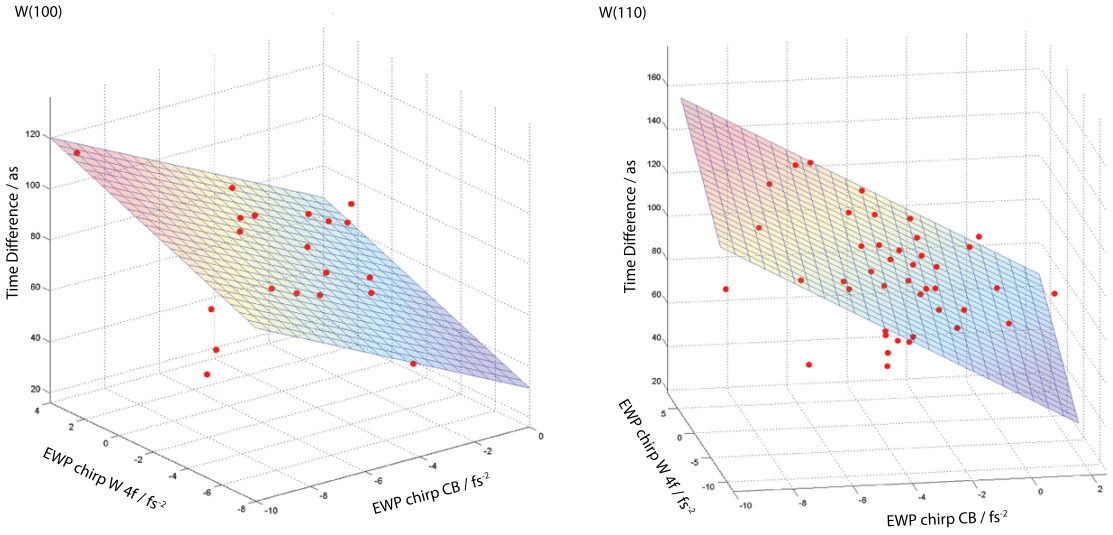

Figure 5.28.: Three dimensional plots of the measured, relative streaking delay of CB and W 4f electrons for W(100) (left side) and W(110) (right side) plotted against the retrieved CB and W 4f EWP chirp. A least squares, planar fit has been realized and is shown for both crystal directions.

	slope (10^{-3} fs^3)	y-intercept (as)
W(110) CB	$-4,8 \pm 1,3$	$74,4 \pm 5,8$
W(110) W4f	$-3,5 \pm 1,5$	$83,3 \pm 5,2$
W(100) CB	$-4,8 \pm 1,7$	$49,2 \pm 9,1$
W(100) W4f	$-1,9 \pm 2,5$	$66,7 \pm 7,9$
Simulation	$-4,9 \pm 0,01$	$1,2 \pm 0,2$

Table 5.1.: Results of the linear interpolation of the chirp dependence given in Fig 5.27. Results of the influence of cross-section variations taken from [136] for W 4f and W 5d states on simulated data are given for comparison.

the experimental uncertainty. In (100) the same behavior arises, but with a lower overall slope, giving $\Delta\tau_{-6}^{(100)} = 68\ as$. Equation 5.12 now enables to compare our data with the measurements performed by Cavalieri et al. [17]. The average chirp values for the CB and the W 4f peak in their work have been denoted as $-9\ fs^{-2}$ and $-5\ fs^{-2}$, respectively [32]. For these values, the least-squares fit to our data reveals a temporal delay of 116 as. This value is very close to the result measured by Cavalieri et al. of $110 \pm 70\ as$. Therefore, it is possible that the overall value could have been modified solely by the chirp dependence. On the other hand, the actual chirp distribution of the measurements by Cavalieri et al. is not known to us, while the standard deviation of this first measurement is rather large at 70 as so that additional modifications by an oxygen contribution can be present. Consequently, by an inclusion of an additional delay as part of an inherent chirp dependence and possible oxygen contributions, the results of [17] can be well reproduced. In future measurements, one could perform measurements with XUV-mirrors inducing a negative chirp (e.g. $-5\ fs^{-2}$) and, in a second measurement, positive chirp (e.g. $5\ fs^{-2}$) to increase the precision of the chirp dependence determination. Moreover, it would be desirable to diminish variations of the laser waveform, especially the laser intensity, as well as fluctuations in the laser pointing in order to reduce the scatter of the data. Concepts, which build on the measurement of the second harmonic signal after introduction of an additional chirp by, e.g., a pulse shaper, can be used to measure and stabilize the NIR chirp. By doing so, its contribution to the XUV-chirp can be controlled, which in turn allows modification of the wavepacket chirp.

As the comparison of the chirp-free delays showed, the values of $\Delta\tau_0^{(110)}$ and $\Delta\tau_0^{(100)}$ do not deviate largely from each other, which could have been an indication of final state, band structure dependent effects. In terms of band structure dependent effects as i.e. discussed by Krasovskii [26], these temporal delays reflect the average group velocities as given by $v_G = \frac{1}{\hbar}\frac{\partial E}{\partial k}$ without dispersive effects implied by group velocity dispersion. In this picture, a notable difference in the average group ve-

locities would point towards a final state modification of the velocities by i.e. the proximity to a band gap, where the average group velocity within the solid is lower than in vacuum according to equation 2.4. The coincidence of the retrieved delays at least invokes that no prominent band structure features exist that clearly shift the overall delay. However, the interpretation of band structure features solely from the temporal delays of two crystal orientations is rather difficult or in doubt, since, as has been discussed before, the angle integrated measurement integrates over k-vectors within the whole Brillouin-zone. Therefore, one either has to resort to angle resolved measurements, which in principle can be performed with the newly built TOF-spectrometer (for large enough excitation intensities), or find an energy, at which the band structure exhibits prominent features for one crystal orientation in such a way that a strong modification of the delay can be expected. Since all measurements performed here are based on an integration over approx. 18° (as given by the acceptance angle of the TOF-spectrometer), no preference of band structure or localization induced effects can be made regarding the chirp-free delays.

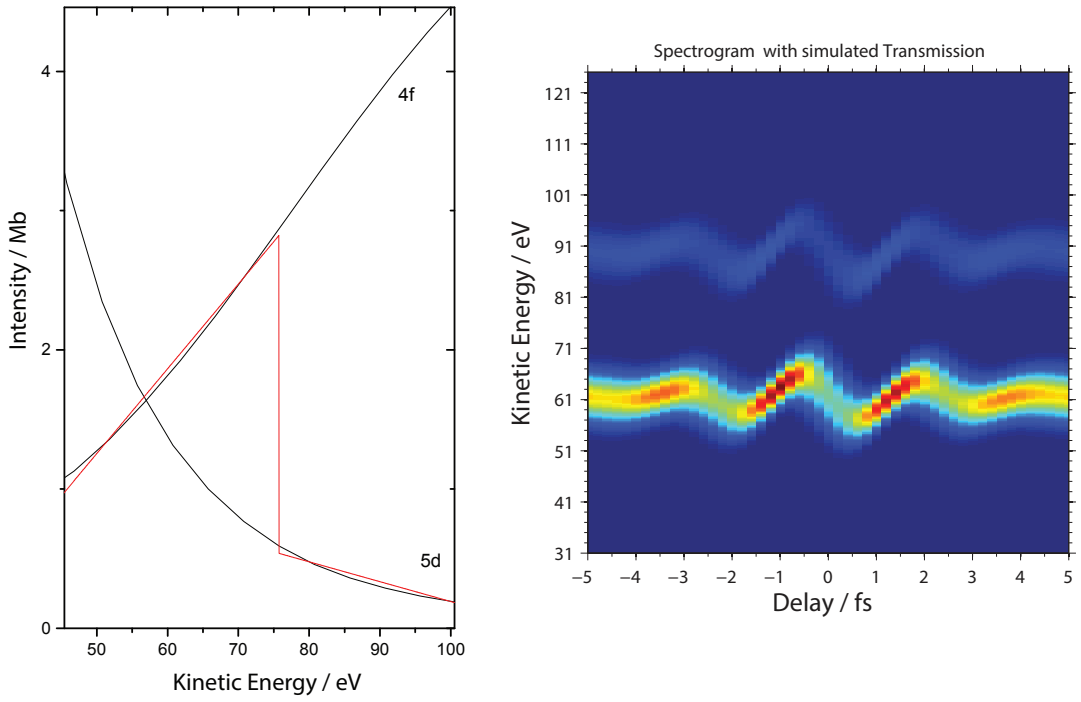

Figure 5.29.: Left: Atomic cross-sections for W 4f and W 5d taken from [136] and the transmission function (red line), derived from a linear fit to the corresponding cross-section. Right: Simulated spectrogram after application of the cross-section derived transmission function.

Recent experiments on Ne [14] guided attention to the emergence of a Wigner shift delay between Ne 2p and 2s states apparent in gas phase streaking measurements.

This initial delay can have a large impact, since it defines the onset of the timing between the emitted wavepackets and was measured to be larger than expected [137]. In the same way, it is possible that atomic effects serve as the origin of an additional chirp and wavepacket delay. In particular, strong variations in the atomic cross-sections have been very recently found to largely modify the form of the emitted EWPs in gas phase experiments on Ar/Ne [138]. Such variations are also present for the 4f and 5d states of tungsten around an energy of 90 eV with different sign in the slopes of the intensity dependence of each state (see Fig. 5.29). An estimate of a cross-section induced influence can be performed by a direct modification of simulated wavepackets with the atomic cross-sections taken from [136]. In a first approximation, a linear interpolation of the cross-section's energy dependency has been deduced to achieve a modification, which is independent of the wavepacket's center energy. Such an approximation seems reasonable, since the cross-section variations are not deviating largely from a linear fit in the observed energy range. The application of the intensity variations leads to the occurrence of a chirp-dependent artificial delay in the simulated data (for wavepackets with the same initial CB and W 4f chirp), as can be seen in Fig. 5.27 (blue points). The parameters of a linear fit to this dependence are summarized in table 5.1. The slope of the cross-section induced change shows a remarkable coincidence with the slope of the chirp dependency, measured in our experiment, especially for the CB electrons. Atomic cross-section effects, in fact, seem to account for a large fraction of the observed chirp/delay- correlation and induce delays up to 53 as, while broadening the overall Gaussian distribution. The delay seems to be unaffected of cross-section modifications only for zero chirp.
Effects related to atomic (photon) energy dependent modifications are not expected to vary between different crystal orientations. Remaining deviations from the simulated cross-section dependency in the slopes and offset of the linear correlation, especially between the (110) and (100) orientations of tungsten, should therefore originate from other EWP modifications. The variations between W(110) and W(100) and the different chirp magnitudes of the CB and W 4f peak for the same measurement in general are an indication of band structure related effects (final state effects), where a delay shift and an additional chirp can be introduced to a wavepacket via the group velocity dispersion. The largest slope in the chirp dependency was observed for the CB electrons for both crystal orientations. It is possible that this strong dependency results from the proximity towards a final state band gap, where the change in energy dispersion over the wave vector is large and the group velocities vary accordingly. Small changes in the XUV pulse central energy, full width half maximum or chirp could thus be translated into variations of the average wavepacket delay and chirp. On the other hand, the weaker dependency (lower slope of the linear fit) observed for the W 4f wavepackets could point towards a more free electron like final state dispersion. Such an explanation would fit well with the observed behavior, since also the measured wavepacket chirps of the CB

electrons are constantly larger than the W 4f chirps. However, a direct comparison with bandstructure calculations is hindered by the integration across large angles (up to ± 18°) inherent to our time-of-flight measurements, as mentioned before.
In discussion of other effects, the average wavepacket chirp could be subject to screening effects as electronic screening is predicted to occur within a timescale of a few a.u. after the creation of a photohole [42]. In this manner, the trailing and leading edge of the subsequently emitted electron wavepacket would feel a different potential as part of the arising screening. Group velocity dispersion would result from this time dependent variation, giving a chirped electron wavepacket. Different CB and W 4f wavepacket chirps are yet not expected from electronic screening, but are clearly visible from our data.
In combination with previous experiments [18, 70], our measurements provide further indication for the emergence of final state propagation effects on the electron wavepacket delay. Albeit, it should also be noted that different CB and W 4f wavepacket chirps have been recently predicted within the model of Zhang et al. [78]. In a recent paper by Liao et al. [71], the relative delays have been traced back to a combination of a different conduction band- and core level-localization as well as the influence of the mean free path and NIR-penetration depth. In their model, a different CB- and core level-chirp is also predicted for the final spectrograms, resulting from the screening of the NIR-field and the electron localization character. In this case, the measured chirp would be artificial reflecting the localization of the electronic state. Wavepacket delay-chirp correlations have yet not been predicted within this model so far. Nonetheless, different chirp values for CB and core levels could be reproduced well.
It should also be noted that estimations based solely on the free-electron propagation model, though giving good predictions for the nearly-free electron metal magnesium, most probably do not give reliable results on tungsten with its partly localized valence band states. Here, the propagation velocity inside the solid is calculated according to $v_f = \sqrt{2 \cdot (E_{kin} + V_0)/m_e}$ with the kinetic energy E_{kin} and the inner potential V_0. Inclusion of the mean free path then allows an estimation of the delay, which, for mean free paths of 3.6 Å(CB) and 3.9 Å(W 4f) derived by the overlayer method, were calculated before [31] yielding approx. 25 as for an excitation energy of 92 eV. This value is largely underestimating the measured values, showing that this model seems to be too simple disregarding the complex band structure of tungsten and/or the variation in the localization between the states.

In summary, we measured for the W(110) and (100) surfaces the relative time delays between the conduction band and W 4f states and compared them to the electron wavepacket chirp for both energy levels. It has been shown that reliable information on the excitation pulse, the electronic transport and screening processes can only be derived from such attosecond streaking data, if detection and evaluation artifacts are

identified and accounted for. The data show a linear correlation between wavepacket chirp and time delay with a larger slope of the CB dependency and generally larger chirp magnitudes of the CB electron wavepackets compared to the W 4f levels. The origin of this effect seems, in its majority, to stem from cross-section variations of the 4f and 5d states of tungsten. The remaining dependency and variations for different crystal orientations are strong indications of band structure related (final state) effects.
The results originating from this work provide deeper insight into the electron dynamics at the attosecond timescale and in particular, stress the importance of final state propagation effects within the solid. Extension of these experiments to time and angle resolved measurements to lift the k-dependency of the wavepackets can provide further information and facilitate comparison with theoretical calculations. A theoretical understanding of the source of the chirp-delay dependency can open the pathway to precise control of electronic movement within the crystal on the attosecond timescale. Such control can open vast possibilities regarding electronic based communication or processing.

Chapter 6.

Summary & outlook

Attosecond streaking spectroscopy has developed into a unique tool nowadays and has proven to provide insight into electron dynamics from the atomic scale to condensed matter systems with unprecedented temporal resolution. In particular, the observation of electron transport in solids holds promise to entail more detailed knowledge on photoelectron propagation and electronic rearrangement/screening after excitation. However, a deeper understanding of these processes is so far hindered by limitations inherent to the HHG process. They appear as a limited maximal XUV photon energy, which confines the measurements to a few materials with suitable core levels, and a low XUV intensity, which i.e. prevent the sampling of a full angular resolved spectrogram. While the XUV energy depends solely on the laser capabilities (mostly the laser intensity and pulse duration), the XUV intensity can be at least partly compensated by an improvement of the TOF detection system.

In this work, a new TOF spectrometer had been devised and implemented, which builds on a large acceptance angle of $\pm 50°$ and an advanced anode segmentation concept. The segmentation of the anodes, where each has its own detection electronics, allows one to significantly reduce the effective deadtime, normally introduced by the CFD/TDC pulse-discrimination setup. The detection efficiency is thereby increased in the same way, since a lower percentage of electrons is discarded in the detection process. Moreover, a sophisticated lens design was implemented in the setup, which features a dispersion-free spatial mapping of the angle-dependent electron distribution in the relevant energy range of 40 eV to 150 eV. The constant transmission over a wide energy span will further increase the quality of the acquired data, omitting the need to post-process the measured spectrograms with the help of spectrometer specific transmission curves. In combination with the given segmentation, the spatial mapping further allows one to resolve the electrons' angular distribution. Since the maximal acceptance angle can be freely varied up to the detection limit of $\pm 50°$, the angular resolution can also be varied between 2.5° and 10°, given as the spatial resolution of one segment. The new spectrometer allows an in situ measurement of

different angular directions without the need to change the detection direction. At maximal resolution, the angular electron distribution for excitation energies below 100 eV can be sampled within a small range of **k**-vectors inside the Brillouin-zone. This will enhance the comparability with theoretical band structure calculations, so far limited to a single **k**-vector. Apart from that, the application of s-polarized NIR probe-pulses could shed light on the influence of the NIR light on electron propagation within the solid. In this case, the polarization direction is not changed upon refraction at the surface, which implies an unmodified NIR field strength at the point (in time and space) of ionization. The angular and energy resolution of the spectrometer should enable one to decompose the asymmetric broadening of the momentum distribution, induced by the instantaneous momentum change of the NIR field. In this way, residual propagation effects in adsorbates on surfaces could be investigated, as, e.g., present for electrons emitted from a monolayer of xenon on tungsten [31], by conducting subsequent s- and p-polarized measurements on the same laser spot. S-polarized measurements deliver additional timing information by negligible NIR-screening at the point of emission.

Beyond the improvements of the detection system, it is certainly important to know about the capabilities of the theoretical TDSE-retrieval algorithm, which calculates the relative delay from the given spectrograms. The TDSE routine has been reviewed before [14, 31], showing modifications of the retrieved delay by satellite XUV-pulses or the TOF transmission function. As an extension of this work, an artificial delay originating from a wrong retrieval for large EWP-chirps (of magnitude larger than 10 fs^{-2}) has been found in this thesis. Its magnitude and sign is strongly dependent on the magnitude and sign of the EWP chirp and can be traced back to asymmetries in the streaking curves, occurring after background subtraction. However, this deviation can be neglected for small chirps below $|10\ fs^{-2}|$, so that a range of trustable values can be defined.

The field of electron transport in condensed matter is heading towards one complete theory, where so far several divergent theoretical approaches exist with different opinions regarding the importance of the NIR-skin depth, state localization, band structure or the inelastic mean free path. In order to illuminate the origin of the measured streaking delays, large series of streaking spectrograms have been recorded on tungsten for two different crystal surfaces, (110) and (100). While the found average relative delays between CB and W 4f states are similar for both directions, thereby not permitting a conclusion about the existence of final state effects, the data showed a distinct trend of the streaking delay against the retrieved chirp of the electron wave packets. This behavior can have a large impact on the interpretation of streaking delays, as the retrieved values can vary in average up to 50 as in the observed range of EWP chirps from 0 fs^{-2} to $-10\ fs^{-2}$. In terms of a 3D analysis of the dependency of our data, it was possible to reproduce the relative streaking

delay of the proof-of-principle experiment on W(110) by Cavalieri, applying the average EWP chirp values measured in their experiment. The delay was found to be shifted upwards by a chirp dependent contribution and a possible additional delay, induced by contamination of the surface with oxygen. The chirp dependence in our data was found to differ for the two measured crystal surfaces, W(110) and W(100). Moreover, a three dimensional analysis reveals a generally stronger influence of the CB wave packets (compared to the W 4f EWP) on the EWP chirp. The latter is most likely not induced by an influence of the NIR field, since no dependence of the EWP on the NIR field strength can be found. An analysis of the cross-section variations across the W 4f and conduction band wavepackets led to the conclusion that such atomic effects can, in fact, amount for a large fraction of the observed dependency. Remaining variations in the chirp dependency and the chirp magnitudes themselves for different crystal orientations seem to originate from bandstructure induced wavepacket modifications. However, further measurements with a smaller data spread induced by jitter of the laser parameters and the laser pointing in collaboration with theoretical calculations are needed to draw further conclusions. In this regard, it would be useful to measure spectrograms with different initial XUV-chirps, i.e. at $-5\ fs^{-2}$ and $5\ fs^{-2}$. This can be achieved by introducing XUV-mirrors with different group delay dispersions. Further, subsequent gas phase measurements may help to decompose the XUV chirp from chirp contributions arising within the solid. In summary, even though localization induced effects cannot be excluded and have been predicted to explain the CB and W 4f EWP chirp [71], the different chirp behaviors for different crystal orientations and between CB and W 4f wave packets point towards band structure induced effects.

Attosecond spectroscopy can help to gain information on a large variety of processes within the solid, including electronic screening, charge transfer, Fano resonances [139] or plasmon formation [29]. Within this thesis, a new, custom TOF detection system has been designed and implemented, which should increase the capabilities of the attosecond streaking setup, regarding its large detection efficiency, constant energy dependent transmission and provided angular resolution. In addition to the recent investigations on the W(110) and W(100) chirp dependencies, these improvements can advance theoretical effort in decomposing different contributions to the delay. Improvements beyond this point can solely be achieved in collaboration with further development of the laser capabilities, which is still the major limiting factor of attosecond science.

Appendix A.

Attogram data extraction

The analysis so far resorts to the application of the TDSE-routine for the retrieval of the relative temporal delay and wavepacket chirp. Even though the TDSE retrieval is supposed to give reliable values for chirp magnitudes below 10 fs^{-2} (see section 5.3.1), given the manifold of transitions contributing to the conduction band, errors in the chirp retrieval could be invoked as the current algorithm is fitting only a single transition. Previous tests have shown that the fitting of each spectrum is basically following the most dominant transition line. However, it seems useful to identify to which extent other detection schemes can reliably determine the electron wavepacket chirp.
Therefore, the capabilities of the Attogram algorithm should be revised in more detail. The Attogram retrieval of a simulated streaking spectrogram for usual excitation parameters and an EWP chirp of -8 fs^{-2} results in vector potentials of the W 4f- (blue curve) and the CB transition (red curve) as shown in Fig. A.1 (top left). Each spectrum of the streaking was preprocessed in such a way that a Shirley background was calculated, appended and subsequently subtracted again by the Shirley background subtraction algorithm. The simulated streakings have been chosen such that the simulated W 4f and CB electron wavepackets show no delay to each other. Yet, the vector potentials, retrieved by the Attogram algorithm, show a temporal delay of the potentials by as much as 89 as, even though the form of the vector potentials is almost identical.
The artificial delay seems to arise as a result of deficiencies in the background subtraction and is strictly dependent on the wavepacket chirp as well, giving a vanishing delay for zero chirp. In consideration of the large artificial delay, the retrieval of temporal delays between EWPs by comparing the vector potentials retrieved by the Attogram algorithm therefore seems to be not feasible. Rather, a time difference retrieval is only possible within the Attogram routine by a careful comparison of the retrieved group delay dispersion across both wavepackets as has been done in [138].
Next, the accuracy of the EWP chirp retrieval shall be discussed in more detail. The Attogram algorithm provides the spectral and temporal pulse form as well as the

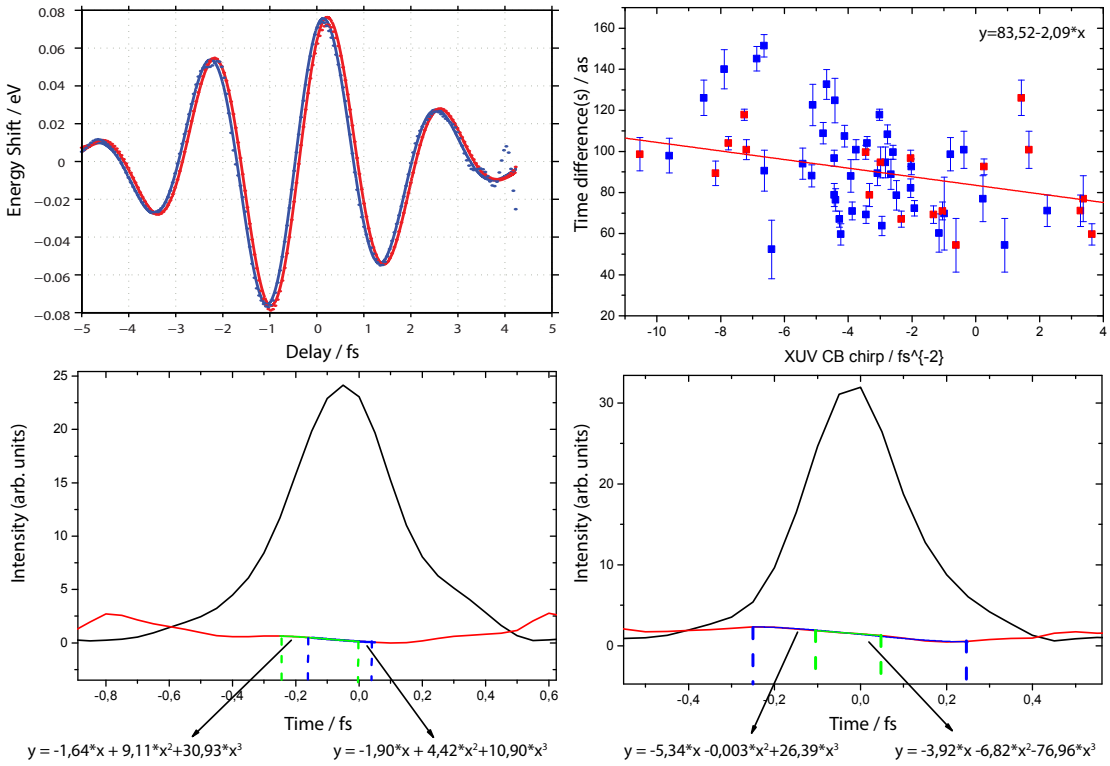

Figure A.1.: Top left: Retrieved vector potentials for the W 4f- (blue curve) and the CB transition (red curve) by the Attogram routine for background subtracted, simulated spectra. An artificial delay from the retrieval can be observed between the initially unshifted W4f and CB peaks. Bottom: Temporal intensity and phase profiles of the W 4f-peak (W(110)) retrieved by the Attogram routine for exemplary real data. Individual third order polynomial fits have been performed on the temporal phase between different borders as given by the dashed lines. The second order polynomial can strongly deviate depending on the position (left) and width (right) of the observed window. Top right: Comparison of the TDSE chirp dependence (blue points) and the chirp dependence of the Attogram derived points (red).

corresponding phase term of the EWP as a result. The chirp can thereby be derived by a comparison with a polynomial fit to the temporal phase. More precisely, the Taylor expansion of the temporal phase $\Phi(t)$ around the center of the pulse t_0 contains the average EWP chirp in its second derivative. Comparison with the second derivative of the polynomial fit therefore gives the chirp. The additional polynomial fit to the data, however, can introduce an additional error to the retrieval. Fig. A.1 (bottom right) shows the retrieved temporal pulse as well as the corresponding phase

of the W 4f peak for a measurement on a W(110) substrate. It can be seen that in dependence of the width of the fitting window the values of the second derivative in phase can strongly deviate. As the Taylor expansion is only valid in a small area around t_0, the use of a small window seems to be more appropriate. However, it is clear from Fig. A.1 (bottom left) that errors can be introduced depending on the width and position t_0 of the window. These errors alone can be of the magnitude of the retrieved, average chirp value. Therefore, the Attogram routine has been solely used so far to cross-check the retrieved TDSE-values and pulse forms of the EWPs. The chirp dependence of the Attogram derived values has been plotted exemplary for the CB electrons of W(110) as red points in Fig. A.1 (top right) in comparison to the TDSE derived values. In this case, the red points only contain the retrieved chirp values of the Attogram routine, while the values of the relative W 4f - CB delay were still taken from the TDSE routine. Moreover, only values of clearly retrieved spectra with a low deviation between measured and reconstructed spectra have been included, where a good retrieval of the chirp was possible. A linear fit to the Attogram data is shown as red line. The values in general show a weaker trend in dependence of the chirp, yet still containing the same sign of the linear dependence slope. The deviations could be a result of the lower statistics present or of the discussed retrieval errors.
Lately, a more sophisticated algorithm for the retrieval of the chirp introduced by Gagnon et al. [135], which is independent on the spectral form of the emitted wavepacket, has been applied to our data. The retrieved chirp values strongly support the slope of the chirp-delay-dependence already observed within the TDSE algorithm.

Bibliography

[1] E. E. Fill, F. Krausz, and M. G. Raizen. *Single-molecule electron diffraction imaging with charge replacement.* New Journal of Physics (2008) 10, 9, 093015.

[2] F. Remacle and R. D. Levine. *An electronic time scale in chemistry.* Proceedings of the National Academy of Sciences of the United States of America (2006) 103, 18, 6793–8.

[3] F. J. Wuilleumier and M. Meyer. *Pump-probe experiments in atoms involving laser and synchrotron radiation: an overview.* Journal of Physics B: Atomic, Molecular and Optical Physics (2006) 39, 23, R425–R477.

[4] A. Zewail. *Laser femtochemistry.* Science (1988) 113, December.

[5] N. Bloembergen. *From nanosecond to femtosecond science.* Reviews of Modern Physics (1999) 71, 1964, 283–287.

[6] F. Krausz. *Attosecond physics.* Reviews of Modern Physics (2009) 81, 1, 163–234.

[7] A. H. Zewail. *Femtochemistry: Atomic-Scale Dynamics of the Chemical Bond.* The Journal of Physical Chemistry A (2000) 104, 24, 5660–5694.

[8] D. M. Fritz, D. A. Reis, B. Adams, et al. *Ultrafast bond softening in bismuth: mapping a solid's interatomic potential with X-rays.* Science (New York, N.Y.) (2007) 315, 5812, 633–6.

[9] M. F. Kling, C. Siedschlag, A. J. Verhoef, et al. *Control of electron localization in molecular dissociation.* Science (New York, N.Y.) (2006) 312, 5771, 246–8.

[10] I. Shumay, U. Höfer, C. Reuß, et al. *Lifetimes of image-potential states on Cu(100) and Ag(100) measured by femtosecond time-resolved two-photon photoemission.* Physical Review B (1998) 58, 20, 13974–13981.

[11] M. Lisowski, P. Loukakos, U. Bovensiepen, et al. *Ultra-fast dynamics of electron thermalization, cooling and transport effects in Ru(001).* Applied Physics A: Materials Science & Processing (2004) 78, 2, 165–176.

[12] M. Hentschel, R. Kienberger, C. Spielmann, et al. *Attosecond metrology.* Nature (2001) 414, 6863, 509–13.

[13] K. Klünder, J. M. Dahlström, M. Gisselbrecht, et al. *Probing Single-Photon Ionization on the Attosecond Time Scale.* Physical Review Letters (2011) 106, 14, 143002.

[14] M. Schultze, M. Fiess, N. Karpowicz, et al. *Delay in photoemission.* Science (New York, N.Y.) (2010) 328, 5986, 1658–62.

[15] J. Itatani, J. Levesque, D. Zeidler, et al. *Tomographic imaging of molecular orbitals.* Nature (2004) 432, 7019, 867–71.

[16] J. B. Bertrand, H. J. Wörner, P. Salières, et al. *Linked attosecond phase interferometry for molecular frame measurements.* Nature Physics (2013) 9, 3, 174–178.

[17] A. L. Cavalieri, N. Müller, T. Uphues, et al. *Attosecond spectroscopy in condensed matter.* Nature (2007) 449, 7165, 1029–32.

[18] S. Neppl, R. Ernstorfer, E. M. Bothschafter, et al. *Attosecond Time-Resolved Photoemission from Core and Valence States of Magnesium.* Physical Review Letters (2012) 109, 8, 087401.

[19] M. Swoboda, T. Fordell, K. Klünder, et al. *Phase Measurement of Resonant Two-Photon Ionization in Helium.* Physical Review Letters (2010) 104, 10, 103003.

[20] S. Haessler, B. Fabre, J. Higuet, et al. *Phase-resolved attosecond near-threshold photoionization of molecular nitrogen.* Physical Review A (2009) 80, 1, 011404.

[21] T. Udem, R. Holzwarth, and T. W. Hänsch. *Optical frequency metrology.* Nature (2002) 416, 6877, 233–7.

[22] J. Reichert, R. Holzwarth, T. Udem, et al. *Measuring the frequency of light with mode-locked lasers.* Optics Communications (1999) 172, 1-6, 59–68.

[23] E. Goulielmakis, Z.-H. Loh, A. Wirth, et al. *Real-time observation of valence electron motion.* Nature (2010) 466, 7307, 739–43.

[24] M. Uiberacker, T. Uphues, M. Schultze, et al. *Attosecond real-time observation of electron tunnelling in atoms.* Nature (2007) 446, 7136, 627–32.

[25] R. Kienberger and E. Goulielmakis. *Atomic transient recorder.* Nature (2004) 427, February, 817–821.

[26] E. E. Krasovskii. *Attosecond spectroscopy of solids: Streaking phase shift due to lattice scattering.* Physical Review B (2011) 84, 19, 195106.

[27] C.-H. Zhang and U. Thumm. *Probing dielectric-response effects with attosecond time-resolved streaked photoelectron spectroscopy of metal surfaces.* Physical Review A (2011) 84, 6, 063403.

[28] A. Kazansky and P. Echenique. *One-Electron Model for the Electronic Response of Metal Surfaces to Subfemtosecond Photoexcitation.* Physical Review Letters (2009) 102, 17, 177401.

[29] C. Lemell, B. Solleder, K. Tőkési, et al. *Simulation of attosecond streaking of electrons emitted from a tungsten surface.* Physical Review A (2009) 79, 6, 062901.

[30] E. Magerl. *Attosecond photoelectron spectroscopy of electron transport in solids.* Ph.D. thesis, Ludwigs-Maximilians-Universität München (2011).

[31] S. Neppl. *Photoemission from Surfaces and Interfaces.* Ph.D. thesis, Technische Universität München (2012).

[32] A. Cavalieri, N. Müller, and T. Uphues. *Attosecond spectroscopy in condensed matter Supplementary Information.* Nature (2007) 1–24.

[33] H. Hertz. *Ueber einen Einfluss des ultravioletten Lichtes auf die electrische Entladung.* Annalen der Physik und Chemie (1887) 31, 8, 983–1000.

[34] A. Einstein. *Über einen die Erzeugung und Verwandlung des Lichtes betreffenden heuristischen Gesichtspunkt.* Annalen der Physik (1905) 17, 6, 132–148.

[35] S. Hüfner. *Photoelectron Spectroscopy: Principles and Applications.* Springer-Verlag Berlin Heidelberg (2003).

[36] M. Lewenstein, P. Balcou, M. Ivanov, et al. *Theory of high-harmonic generation by low-frequency laser fields.* Physical Review A (1994) 49, 3, 2117–2132.

[37] C. Kittel. *Einführung in die Festkörperphysik.* Oldenbourg Wissenschaftsverlag GmbH, München (2013).

[38] C. J. Powell and A. Jablonski. *Evaluation of Calculated and Measured Electron Inelastic Mean Free Paths Near Solid Surfaces.* Journal of Physical and Chemical Reference Data (1999) 28, 1, 19.

[39] A. Zangwill. *Physics at surfaces.* Cambridge University Press (1988).

[40] T. Leung, C. Kao, W. Su, et al. *Relationship between surface dipole, work function and charge transfer: Some exceptions to an established rule.* Physical Review B (2003) 68, 19, 195408.

[41] A. Borisov, D. Sanchez-Portal, R. Diez Muino, et al. *Building up the screening below the femtosecond scale.* Chemical Physics Letters (2004) 387, 1-3, 95–100.

[42] R. D. Muino, D. Sanchez-Portal, V. M. Silkin, et al. *Time-dependent electron phenomena at surfaces.* Proceedings of the National Academy of Sciences of the United States of America (2011) 108, 3, 971–6.

[43] P. A. Brühwiler, O. Karis, and N. Martensson. *Charge-transfer dynamics studied using resonant core spectroscopies.* Reviews of Modern Physics (2002) 74, 3, 703–740.

[44] D. Menzel. *Ultrafast charge transfer at surfaces accessed by core electron spectroscopies.* Chemical Society reviews (2008) 37, 10, 2212–23.

[45] A. H. Zewail. *Femtochemistry.* Wiley-VCH Verlag GmbH, Weinheim, FRG (2001).

[46] Z. Chang. *Fundamentals of Attosecond Optics.* Taylor and Francis Group (2011).

[47] P. Franken and A. Hill. *Generation of optical harmonics.* Physical Review Letters (1961) 7, 1, 118–120.

[48] M. Wegener. *Extreme Nonlinear Optics.* Springer-Verlag Berlin Heidelberg (2005).

[49] A. McPherson, G. Gibson, H. Jara, et al. *Studies of multiphoton production of vacuum-ultraviolet radiation in the rare gases.* JOSA B (1987) 4, 4, 595–601.

[50] P. Corkum. *Plasma perspective on strong field multiphoton ionization.* Physical Review Letters (1993) 71, 13, 1994–1997.

[51] P. Hommelhoff, C. Kealhofer, A. Aghajani-Talesh, et al. *Extreme localization of electrons in space and time.* Ultramicroscopy (2009) 109, 5, 423–9.

[52] S. Kazamias and P. Balcou. *Intrinsic chirp of attosecond pulses: Single-atom model versus experiment.* Physical Review A (2004) 69, 6, 063416.

[53] P. Salières, B. Carré, L. Le Déroff, et al. *Feynman's path-integral approach for intense-laser-atom interactions.* Science (New York, N.Y.) (2001) 292, 5518, 902–5.

[54] M. Bellini, C. Lyngå, A. Tozzi, et al. *Temporal Coherence of Ultrashort High-Order Harmonic Pulses.* Physical Review Letters (1998) 81, 2, 297–300.

[55] P. Salières, A. L'Huillier, and M. Lewenstein. *Coherence Control of High-Order Harmonics.* Physical Review Letters (1995) 74, 19, 3776–3779.

[56] F. Lindner, G. Paulus, H. Walther, et al. *Gouy Phase Shift for Few-Cycle Laser Pulses.* Physical Review Letters (2004) 92, 11, 113001.

[57] M. Schnürer, Z. Cheng, M. Hentschel, et al. *Few-cycle-driven XUV laser harmonics: generation and focusing.* Applied Physics B (2000) 70, S1, S227–S232.

[58] Z. Chang, A. Rundquist, H. Wang, et al. *Temporal phase control of soft-x-ray harmonic emission.* Physical Review A (1998) 58, 1, R30–R33.

[59] J. Mauritsson, P. Johnsson, R. López-Martens, et al. *Measurement and control of the frequency chirp rate of high-order harmonic pulses.* Physical Review A (2004) 70, 2, 021801.

[60] I. Christov, R. Bartels, H. Kapteyn, et al. *Attosecond Time-Scale Intra-atomic Phase Matching of High Harmonic Generation.* Physical Review Letters (2001) 86, 24, 5458–5461.

[61] I. Christov, M. Murnane, and H. Kapteyn. *High-Harmonic Generation of*

Attosecond Pulses in the Single-Cycle Regime. Physical Review Letters (1997) 78, 7, 1251–1254.

[62] E. Goulielmakis, M. Schultze, M. Hofstetter, et al. *Single-cycle nonlinear optics.* Science (New York, N.Y.) (2008) 320, 5883, 1614–7.

[63] M. Hofstetter, M. Schultze, M. Fiess, et al. *Attosecond dispersion control by extreme ultraviolet multilayer mirrors.* Optics express (2011) 19, 3, 1767–76.

[64] A. Wonisch and U. Neuhäusler. *Design, fabrication, and analysis of chirped multilayer mirrors for reflection of extreme-ultraviolet attosecond pulses.* Applied optics (2006) 45, 17.

[65] J. Itatani, F. Quéré, G. Yudin, et al. *Attosecond Streak Camera.* Physical Review Letters (2002) 88, 17, 173903.

[66] P. B. Corkum, N. H. Burnett, and M. Y. Ivanov. *Subfemtosecond pulses.* Optics Letters (1994) 19, 22, 1870.

[67] E. Constant, D. Garzella, P. Breger, et al. *Optimizing High Harmonic Generation in Absorbing Gases: Model and Experiment.* Physical Review Letters (1999) 82, 8, 1668–1671.

[68] R. Kienberger, M. Hentschel, M. Uiberacker, et al. *Steering attosecond electron wave packets with light.* Science (New York, N.Y.) (2002) 297, 5584, 1144–8.

[69] M. Uiberacker, E. Goulielmakis, R. Kienberger, et al. *Attosecond Metrology with Controlled Light Waveforms.* Laser Physics (2005) 15, 1, 195–204.

[70] S. Neppl, R. Ernstorfer, A. L. Cavalieri, et al. *Direct observation of electron propagation and dielectric screening on the atomic length scale.* Nature (2015) 517, 7534, 342–346.

[71] Q. Liao and U. Thumm. *Attosecond Time-Resolved Photoelectron Dispersion and Photoemission Time Delays.* Physical Review Letters (2014) 112, 2, 023602.

[72] M. Drescher, M. Hentschel, R. Kienberger, et al. *Time-resolved atomic inner-shell spectroscopy.* Nature (2002) 419, 6909, 803–7.

[73] M. Drescher and F. Krausz. *Attosecond physics: facing the wave- particle*

duality. Journal of Physics B: Atomic, Molecular and Optical Physics (2005) 38, 9, S727–S740.

[74] D. Kane and R. Trebino. *Characterization of arbitrary femtosecond pulses using frequency-resolved optical gating*. IEEE Journal of Quantum Electronics (1993) 29, 2, 571–579.

[75] R. Trebino, K. W. DeLong, D. N. Fittinghoff, et al. *Measuring ultrashort laser pulses in the time-frequency domain using frequency-resolved optical gating*. Review of Scientific Instruments (1997) 68, 9, 3277.

[76] C. Lemell, K. Tőkési, and J. Burgdörfer. *Time-resolved photoelectron emission from surfaces*. Journal of Physics: Conference Series (2012) 388, 1, 012048.

[77] C.-H. Zhang and U. Thumm. *Effect of wave-function localization on the time delay in photoemission from surfaces*. Physical Review A (2011) 84, 6, 065403.

[78] C.-H. Zhang and U. Thumm. *Attosecond Photoelectron Spectroscopy of Metal Surfaces*. Physical Review Letters (2009) 102, 12, 123601.

[79] A. G. Borisov, D. Sánchez-Portal, a. K. Kazansky, et al. *Resonant and non-resonant processes in attosecond streaking from metals*. Physical Review B (2013) 87, 12, 121110.

[80] U. Keller. *Recent developments in compact ultrafast lasers*. Nature (2003) 424, 6950, 831–8.

[81] D. Strickland and G. Mourou. *Compression of amplified chirped optical pulses*. Optics Communications (1985) 55, 6, 447–449.

[82] M. Nisoli, S. De Silvestri, and O. Svelto. *Generation of high energy 10 fs pulses by a new pulse compression technique*. Applied Physics Letters (1996) 68, 20, 2793.

[83] R. Szipocs, K. Ferencz, C. Spielmann, et al. *Chirped multilayer coatings for broadband dispersion control in femtosecond lasers*. Optics letters (1994) 19, 3, 201.

[84] J. Eckstein, A. Ferguson, and T. Hänsch. *High-resolution two-photon spectroscopy with picosecond light pulses*. Physical Review Letters (1978) 40, 1977, 13–16.

[85] S. Planas and N. P. Mansur. *Spectral narrowing in the propagation of chirped pulses in single-mode fibers.* Optics letters (1993) 18, 9, 699–701.

[86] S. Cundiff and J. Ye. *Colloquium: Femtosecond optical frequency combs.* Reviews of Modern Physics (2003) 75, 1, 325–342.

[87] A. Apolonski, A. Poppe, G. Tempea, et al. *Controlling the phase evolution of few-cycle light pulses.* Physical review letters (2000) 85, 4, 740–3.

[88] M. Krüger, M. Schenk, and P. Hommelhoff. *Attosecond control of electrons emitted from a nanoscale metal tip.* Nature (2011) 475, 7354, 78–81.

[89] T. Wittmann, B. Horvath, W. Helml, et al. *Single-shot carrier-envelope phase measurement of few-cycle laser pulses.* Nature Physics (2009) 5, 5, 357–362.

[90] T. Naeser. *Photo Credit.*

[91] L. Sarkadi and A. Orbán. *A time-of-flight electron spectrometer for studies of forward electron emission in ion-atom collisions.* Measurement Science and Technology (2006) 17, 1, 84–90.

[92] A. Eppink and D. Parker. *Velocity map imaging of ions and electrons using electrostatic lenses: Application in photoelectron and photofragment ion imaging of molecular oxygen.* Review of Scientific Instruments (1997) 68, 9, 3477.

[93] A. Adams and F. Read. *Electrostatic cylinder lenses II: Three element einzel lenses.* Journal of Physics E: Scientific Instruments (1972) 150.

[94] R. Imhof and F. Read. *A three-aperture electron optical lens for producing an image of variable energy but fixed position.* Journal of Physics E: Scientific Instruments (1968) 859, 1–3.

[95] F. Read. *A symmetric electrostatic lenses of three apertures.* Journal of Physics E: Scientific Instruments (1970) 127.

[96] D. de Bruijn, P. van Deenen, and D. Dijkkamp. *Microchannel plate report.* Technische Informatie Post .

[97] S. N. Samarin, O. M. Artamonov, D. K. Waterhouse, et al. *Highly efficient time-of-flight spectrometer for studying low-energy secondary emission from*

dielectrics: Secondary-electron emission from LiF film. Review of Scientific Instruments (2003) 74, 3, 1274.

[98] O. Jagutzki. *Fast position and time resolved read-out of micro-channelplates with the delay-line technique for single particle and photon detection.* Tech. rep., Johann Wolfgang Goethe-Universität, Frankfurt (1998).

[99] D. Gedcke and W. McDonald. *A constant fraction of pulse height trigger for optimum time resolution.* Nuclear Instruments and Methods (1967) 55, 377–380.

[100] D. Gedcke and W. McDonald. *Design of the constant fraction of pulse height trigger for optimum time resolution.* Nuclear Instruments and Methods (1968) 58.

[101] F. Wuilleumier and M. Krause. *Photoionization of neon between 100 and 2000 eV: Single and multiple processes, angular distributions, and subshell cross sections.* Physical Review A (1974) 10, 1, 242–258.

[102] B. Kassühlke. *Ein Elektronen-Flugzeitspektrometer für Oberflächenuntersuchungen: Konzeption, Aufbau und erste Anwendungen.* Ph.D. thesis, Technische Universität München (1994).

[103] J. Gagnon and V. S. Yakovlev. *The robustness of attosecond streaking measurements.* Optics express (2009) 17, 20, 17678–93.

[104] J. Gagnon, E. Goulielmakis, and V. Yakovlev. *The accurate FROG characterization of attosecond pulses from streaking measurements.* Applied Physics B (2008) 92, 1, 25–32.

[105] M. Bode, S. Krause, L. Berbil-Bautista, et al. *On the preparation and electronic properties of clean W(110) surfaces.* Surface Science (2007) 601, 16, 3308–3314.

[106] L. N. Tharp. *Energy Spectra of Inelastically Scattered Electrons and LEED Studies of Tungsten.* Journal of Applied Physics (1967) 38, 8, 3320.

[107] E.Bauer. *Adsorption of oxygen on W(110) II. The high coverage range.* Surface Science (1978) 71, 695–718.

[108] Engel. *Adsorption of oxygen on W(110) 1. The p(2 x 1) structure.* Surface Science (2000) 52, 1975, 237–262.

[109] M. van Hove. *M.A. van Hove and S.Y. Tong.* Surface Science (1976) 54, 91–100.

[110] P. S. P. Wei. *Low-Energy Electron Diffraction Study of Tungsten (100) Surface.* The Journal of Chemical Physics (1970) 53, 7, 2939.

[111] T. Felter, R. Barker, and P. Estrup. *Phase Transition on Mo(100) and W(100) Surfaces.* Physical Review Letters (1977) 38, 20, 1138–1141.

[112] D. Riffe, G. Wertheim, and P. Citrin. *Different core-hole lifetime and screening in the surface of W (110).* Physical review letters (1989) 63, 18, 1976–1979.

[113] D. Riffe and G. Wertheim. *Submonolayer oxidation of W(110): a high-resolution core-level photoemission study.* Surface Science (1998) 399, 2-3, 248–263.

[114] J. Feydt, A. Elbe, H. Engelhard, et al. *Photoemission from bulk bands along the surface normal of W (110).* Physical Review B (1998) 58, 20, 1–6.

[115] B. Feuerbacher and B. Fitton. *Directional Photoemission from Three Tungsten Single-Crystal Faces.* Phys. Rev. Lett. (1973) 30, 19, 923–926.

[116] B. Feuerbacher and N. Christensen. *Volume and surface photoemission from tungsten. II. Experiment.* Physical Review B (1974) 10, 6, 2373–2390.

[117] N. Christensen and B. Feuerbacher. *Volume and surface photoemission from tungsten. I. Calculation of band structure and emission spectra.* Physical Review B (1974) 10, 6, 2349–2372.

[118] R. Smith and J. Anderson. *Study of W bulk bands with normal (001) photoemission using synchrotron radiation.* Solid State Communications (1976) 19, 001, 975–978.

[119] L. Mattheiss. *Fermi surface in tungsten.* Physical Review (1965) 139, 1962.

[120] R. Gaylord and S. Kevan. *Spin-orbit-interaction-induced surface resonance on W (011).* Physical Review B (1987) 36, 17, 9337–9340.

[121] M. L. Shek. *Photoemission studies of W(100)-(5x1) and comparison with WC(0001).* Surface Science (1985) 149, 423–448.

[122] R. Willis, B. Feuerbacher, and B. Fitton. *Angular dependence of photoemission*

from intrinsic surface states on W (100). Solid State Communications (1976) 18, 100, 1315–1319.

[123] J. Weaver, C. Olson, and D. Lynch. *Optical properties of crystalline tungsten.* Physical Review B (1975) 12, 4, 1293–1297.

[124] C. Lemell. *Internal Communication.*

[125] S. Hellmann, K. Rossnagel, M. Marczynski-Bühlow, et al. *Vacuum space-charge effects in solid-state photoemission.* Physical Review B (2009) 79, 3, 035402.

[126] S. Passlack, S. Mathias, O. Andreyev, et al. *Space charge effects in photoemission with a low repetition, high intensity femtosecond laser source.* Journal of Applied Physics (2006) 100, 2, 024912.

[127] A. Pietzsch, A. Föhlisch, M. Beye, et al. *Towards time resolved core level photoelectron spectroscopy with femtosecond x-ray free-electron lasers.* New Journal of Physics (2008) 10, 3, 033004.

[128] M. Kitzler, N. Milosevic, A. Scrinzi, et al. *Quantum Theory of Attosecond XUV Pulse Measurement by Laser Dressed Photoionization.* Physical Review Letters (2002) 88, 17, 173904.

[129] J. Gagnon. *Attosecond Electron Spectroscopy Theory and its Applications.* Ph.D. thesis, LMU München (2010).

[130] Y. Mairesse and F. Quéré. *Frequency-resolved optical gating for complete reconstruction of attosecond bursts.* Physical Review A (2005) 71, 1, 011401.

[131] V. S. Yakovlev, J. Gagnon, N. Karpowicz, et al. *Attosecond Streaking Enables the Measurement of Quantum Phase.* Physical Review Letters (2010) 105, 7, 073001.

[132] E. Krasovskii and M. Bonitz. *Spectral Line Shape Variations in Time-Resolved Photoemission from a Solid.* Physical Review Letters (2007) 99, 24, 247601.

[133] T. Engel. *Adsorption of Inert Gases on Tungsten: Measurements on Single Crystal Planes.* The Journal of Chemical Physics (1970) 52, 11, 5572.

[134] E. P. Gyftopoulos and J. D. Levine. *Work Function Variation of Metals Coated by Metallic Films.* Journal of Applied Physics (1962) 33, 1, 67.

[135] J. Gagnon and V. S. Yakovlev. *The direct evaluation of attosecond chirp from a streaking measurement.* Applied Physics B (2011) 103, 2, 303–309.

[136] J. Yeh and I. Lindau. *Atomic subshell photoionization cross sections and asymmetry parameters.* Atomic Data and Nuclear Data Tables (1985) 32, 1, 1–155.

[137] J. Feist, O. Zatsarinny, S. Nagele, et al. *Time delays for attosecond streaking in photoionization of neon.* Physical Review A (2014) 89, 3, 033417.

[138] M. Sabbar, S. Heuser, R. Boge, et al. *Resonance effects in photoemission time delays* (2014) .

[139] M. Wickenhauser, J. Burgdörfer, F. Krausz, et al. *Time Resolved Fano Resonances.* Physical Review Letters (2005) 94, 2, 023002.

Danksagung

Zunächst möchte ich Prof. Dr. Barth, Prof. Dr. Kienberger und Prof. Dr. Krausz danken für die Möglichkeit am Lehrstuhl E20 und im Labor für Attosekundenphysik zu arbeiten.
Allen voran möchte ich Prof. Dr. Feulner danken für seine konstante Unterstützung und sein umfangreiches Wissen in allen experimentellen und theoretischen Bereichen. Ohne seinen wissenschaftlichen Rat und seine Tatkraft, sei es beim Identifizieren von technischen Problemen, weitreichenden Diskussionen oder experimentellen Workarounds, wäre die Arbeit in dieser Form nicht möglich gewesen.
Ich möchte Dr. Hartmut Schlichting für seine Ideen und Kommentare bezüglich des neuen Flugzeitspektrometers, der Weitergabe seines Wissens, sei es bezüglich der durchgeführten Simulationen oder auf Fragestellungen bezüglich der Elektronik, und seiner stets kompetenten Hilfe danken.
Ich danke dem gesamten Team des Labors für Attosekundenphysik, darunter Elisabeth Bothschafter, Florian Mühlbauer, Michael Jobst, Konrad Hütten, Stefan Neppl, Michael Stanislawski, Ralph Ernstorfer für die gute Zusammenarbeit.
Justin Gagnon und Nick Karpowicsz möchte ich über deren grosse Hilfe zu Fragestellungen über die von Ihnen geschriebenen Auswertungsprogramme (Attogram, sowie TDSE) danken, sowie über sehr hilfreiche allgemeine Diskussionen.
Domik Seiler danke ich für seine unermüdliche Arbeit und Unterstützung bei der Erstellung verschiedenster Beschichtungen.
Ich möchte den Mitarbeitern der mechanischen Werkstatt der TUM danken für deren präzise und zuverlässige Arbeit. Insbersondere gilt der Dank Manfred Pfaller und Manfred Reither, dafür, immer anspechbar zu sein und Ihren Rat und Hilfe bei der Umsetzung der einzelnen Zeichnungen.
David Duncan und Francesco Allegretti danke ich für das Korrekturlesen dieser Arbeit, sowie interessante (und hilfreiche) Diskussionen.
Natürlich möchte ich auch meinen Kollegen des Departements E20 danken, allen voran Sybille Fischer, Katharina Diller, Anthoula Papageorgiou und Sushoban Joshi für die gute Arbeitsatmosphäre, moralische Unterstützung und die gute Zeit.
Viktoria Blaschek, Max Glanz, Karl Eberle, Karl Kölbl und Reinhold Schneider danke ich für deren konstante administrative und technische Unterstützung. Inbesondere gilt der Dank Karl Kölbl für das erstellen vieler kleiner Bauteile für das neue Flugzeitspektrometer und Hilfe bei mechanischen Anpassungen und Problemen, sowie Reinhold Schneider für die Umsetzung vieler elektronischer Bauteile und die Unterstützung in diesem Bereich.
Nicht zuletzt möchte ich meiner Mutter danken für Ihre Liebe und Unterstützung auch in schweren Zeiten.